The Martian Radiation Environment - Early Mars and Future Measurements with the Radiation Assessment Detector

Dissertation
zur Erlangung des Doktorgrades
der Mathematisch-Naturwissenschaftlichen Fakultät
der Christian-Albrechts-Universität zu Kiel

vorgelegt von
Bent Ehresmann

Kiel im Januar 2012

Referent/in :	Robert F. Wimmer-Schweingruber
Korreferent/in :	Wolfgang J. Duschl
Tag der mündlichen Prüfung :	27.03.2012
Zum Druck genehmigt :	27.03.2012

Der Dekan

Zusammenfassung

Heutzutage ist die Oberfläche des Mars eine unwirtliche Umgebung für Leben. Aufgrund seiner dünnen Atmosphäre und des Fehlens eines globalen Magnetfelds, ist der Mars nur schlecht vor dem Einfall geladenener Teilchen aus dem Weltall geschützt. Insbesondere hochenergetische galaktische kosmische Strahlung kann sich durch die ganze Atmosphäre bis zum Boden fortbewegen. Diese Strahlung erzeugt, in Kombination mit von ihr in der Atmosphäre und im Boden produzierten Sekundärteilchen, eine Strahlungsumgebung an der Planetenoberfläche, die eine mögliche Gefahr für Leben darstellt. Um diese Gefahr einzuschätzen, wird in der Radiation Assessment Detector (RAD), als Teil der Mars Science Laboratory (MSL) Rover-Mission, diese Strahlenbelastung auf der Marsoberfläche messen. Des Weiteren gibt es deutliche Anzeichen dafür, dass der Mars einmal, früh in seiner Geschichte, sehr viel günstigere Bedingungen für ein potentielles Aufkommen von Leben besaß, insbesondere in der Noachische Periode (vor $\sim$ 4 Milliarden Jahren). Damals war die Atmosphäre beträchtlich dichter und zudem durch ein globales Magnetfeld geschützt. Des Weiteren gab es große Vorkommen an flüssigem Wasser auf der Oberfläche. Diese Umstände deuten an, dass die damalige Strahlungsumgebung weniger gefährlich für Leben gewesen sein könnte. Daher ist es für die Frage, ob sich jemals Leben auf dem Mars entwickeln konnte, von besonderem Interesse, die Strahlenbelastung auf dem frühen Mars abzuschätzen.

In dieser Arbeit wird daher der Einfluss von höheren Atmosphärendrücken, entsprechend einer dichteren Atmosphäre, auf die Strahlenelastung auf und wenig unter der Oberfläche analysiert. Des Weiteren wird ermittlet, welchen Effekt größere Mengen an flüssigem Wasser an der Oberfläche und unterirdischem Wassereis auf das Strahlungsfeld hätten. Hierzu wurde ein Modell entwickelt, mit dem sich die resultierende Strahlendosis aus zunächst berechneten Teilchenflüssen für diese Bedingungen mit Hilfe von Monte Carlo-Methoden ermitteln lassen. Im Rahmen dieser Arbeit konnte der existierende Parameterraum im Bereich der Mars-Strahlungsforschung erweitert werden, da eine große Anzahl an Faktoren für verschiedene Teilchensorten untersucht wurden.

Zusätzlich wurde ein Modell entwickelt, dass einen wichtigen Teil der bordeigenen Datenweiterverarbeitung von RAD nachbildet. Es wird beschrieben, wie die Verarbeitungslogik des Instruments aufgebaut ist, um geladene Teilchen in den Detektor durchdringende und in ihm stoppende Teilchen zu unterscheiden, und wie diese Logik im entwickelten Modell implementiert ist. Es wird erklärt, wie sich mit dem Modell Cut-Werte bestimmen lassen, die für die Teilchenklassifizierung wichtig sind, und wie das Modell hilft die Logik zu verbessern. Es wird außerdem anhand von Kalibrationsdaten gezeigt, dass das entwickelte Modell in der Lage ist, geladene Teilchen korrekt in durchgehende und stoppende Teilchen zu unterscheiden.

Abstract

Today, the surface of Mars is an inhospitable environment for any form of life. Due to its thin atmosphere and lack of a global magnetic field, Mars is only weakly protected from charged particles impeding the planet from outer space. In particular, high-energetic galactic cosmic rays can propagate all the way through the atmosphere to the ground. These high-energetic particles create, along with secondary particles produced in the atmosphere and the soil, a surface radiation environment that can pose a possible hazard for life. To estimate this risk, the Radiation Assessment Detector (RAD) will measure the radiation exposure on the surface, as part of the Mars Science Laboratory rover mission, launched in November 2011 and slated to arrive at Mars in August 2012. Furthermore, there is substantial evidence that, early in the planet's history, conditions on Mars were much more suited for an emergence of life. Especially the Noachian period ($\sim$ 4 billion years ago) is deemed as a promising time span. The atmosphere was considerably denser and shielded by a global magnetic field, and large amounts of liquid water could be found on the surface. These factors indicate a radiation environment less dangerous for life. Thus, quantifying the radiation exposure on early Mars is of high importance for the question if life could have ever emerged there.

In this thesis, the influence of higher atmospheric pressure, corresponding to a denser Noachian atmosphere, on the radiation exposure on and beneath the surface is analysed. Furthermore, the influence of the presence of larger volumes of liquid surface water and subsurface water ice on the radiation field are determined. For this, a model was developed that calculates radiation dose rates from computed particle fluxes for these conditions via Monte Carlo methods. In the scope of this work, the existing parameter space of Martian radiation research is expanded by calculating dose rates of a wide set of particle species for a broad range of environmental changes.

As a second main part of this thesis, a model that mirrors an important part of RAD's onboard data processing and reduction was developed. The setup of the electronics' processing logic is explained in detail and it is described how the instrument aims to distinguish measured charged particles onboard in particles penetrating the detector and stopping in it. The model is used to determine necessary cut values for the particle distinction. Additionally, it is shown that the model is able to correctly distinguish penetrating and stopping charged particles in measured calibration data. Furthermore, findings from this research are employed to improve the processing logic.

Contents

List of Figures

List of Tables

1. Introduction

The question if life might exist somewhere else than on Earth has long occupied the minds and imagination of mankind. This idea is thereby not just rooted in metaphysical or romantic ideas of cosmic pluralism. Besides from wanting to answer this existential question, the scientific aspect of this search for extraterrestrial life can further be based on the simple notion that if life developed on Earth it is not impossible that it might have done so somewhere else in the universe. There are several ways scientists conduct this search, e.g. the on-going hunt for so-called exoplanets has – as of January 2012 – yielded 725 planets outside our solar system. Such planets then can be further analysed for the existence of biotracers which could give indications for the presence of life.

However, the search is not constricted to analysing other star systems or galaxies. There are also theories that simple life could be present outside of Earth within our Solar system, which gives the advantage that one can explore promising locations in-situ. Again, there are different ways to search for extraterrestrial life in our Solar system, e.g. the analysis of soil samples from planets or asteroids for traces or remnants of microbial life. Another approach is to research the prevalent environmental conditions of a planet and how they might affect or have affected a possible emergence or evolution of life.

One of the main places of interest for this kind of research is our neighbour planet Mars, which leads to the motivation of this work: How does the present-day- and early-Mars radiation environment affect the chances of a possible emergence or sustainment of life?

The research presented in this work, in regards to this question, can broadly be divided into two main topics:

1. The analysis of the radiation environment under early-Mars-like conditions.

2. The calibration of a radiation detector developed to measure the Martian surface radiation.

In the following sections, first, an introduction to these two topics is provided. Then, the structure and scope of this work is explained.

1.1. The radiation environment on early Mars

To understand the motivation for the first point one has to be aware that any form of ionising radiation can have possibly hazardous effects on life forms. Energetic particles interact with organic matter via different processes, such as electron ionisation in atoms, which may result in damaged or destroyed cells, a topic further discussed in Ch. 2.2.2. In that context it should be mentioned that planets possess a radiation field on its surface and in its atmosphere. This radiation environment is to a large part created by Galactic Cosmic Rays (GCRs) propagating through the atmosphere and interacting with molecules of atmosphere and soil. These interactions also produce secondary particles, which in turn can also propagate further through the atmosphere to the ground and contribute to the radiation environment. A more detailed look at GCRs and the creation of the planetary radiation environment can be found in Ch. 2.1. For the moment, it is sufficient to keep in mind that a planetary radiation environment can be an influencing factor for a development of life. Taking Earth as an example, one can see that a surface radiation environment does not necessarily have to be hindering for the emergence of life. So, when wanting to analyse the environmental conditions for life on a different planet (in this case, Mars), it is important to know how the radiation environment looks like or has looked like in the past.

As Mars plays a central role in the content of this work and an adequate description would go beyond the scope of this introduction, the present-day and early Mars environment situations will be dealt with in a separate chapter (Ch. 3) and only a broad synopsis of the characteristics relevant to this work is given here. Mars today does not present itself very well-suited for any kind of life. It has atmospheric conditions that do not allow for the existence of liquid surface water for longer time periods, which is disadvantageous as liquid water is considered to be a prerequisite for the emergence of life. Several other factors, such as the lack of a global magnetic field and the low atmospheric pressure, further pose obstacles for a preservation of life. However, even though present-day Mars seems a dry, barren planet, there are still indications that it once contained water in larger amounts.

For this it is important to know that, in principle, Mars has the ability to contain surface water, as it lies on the border of the so-called habitable zone. This zone is defined as the region in a stellar system where a planet has the right distance from the star so that its temperature allows for the prolonged presence of liquid water, whereas outside of the zone planets would be too cold, respectively if they are closer to the star they would be too hot. So, this leads to the possibility that Mars once possessed liquid surface water.

Further confirming this possibility, certain geological features detectable on Mars are

interpreted as having been created by the presence of liquid water, other investigations of Martian rock samples also substantiate this assumption (see Ch. 3.2 for a more detailed look).

These findings led to the idea that it might be reasonable to look into earlier epochs of Mars and analyse if the then prevalent conditions would have been more supporting for life. Especially, the Noachian epoch ($\sim 4.1 - 3.7$ Ga ago) presents itself as a suitable time span. Most of the above mentioned geological features are found in areas formed during this time. Furthermore, research suggests that Noachian Mars still had a global magnetic field, acting as a better shield against radiation from outer space.

Another conclusion is that if early Mars could sustain larger amounts of liquid water for longer time periods, it must have had a considerably denser atmosphere and higher atmospheric pressure. This, subsequently, should result in a radiation environment less hazardous for life. Due to the higher atmospheric pressure GCRs propagating through the Noachian atmosphere would lose more energy on their way to the ground, leading to lower energetic particle fluxes at the surface, compared to present-day. A further advantage is that the Noachian era coincides with the time frame on which life developed on Earth.

The research presented here focuses on the influence of such probable higher atmospheric pressure levels on the radiation environment on Mars. Furthermore, the influence of liquid surface water or sub-surface water ice during such times is also analysed, as well as changes in the radiation environment when going from the surface into the top layers of the soil. All with the underlying idea in mind to place the derived results into the context of the likelihood of a sustainment of possible life, emerged on ancient Mars, i.e. drawing conclusions if the Noachian radiation environment would have been to hindering for such an emergence and a subsequent sustainment of simple life forms.

The aim of this work is to provide a significant addition to the existing research on Martian radiation and expand the previously analysed parameter space. This is done by analysing several aspects of the radiation field for a number of parametric changes in the environmental conditions. E.g., environmental changes include several steps of atmospheric pressure increases, and the influence of a sub-surface water ice layer under these conditions, as well as different amounts of liquid surface water under an increased pressure scenario. For all these analysed conditions, particle fluxes of the most common particle species, created by interaction of primary GCRs with the atmosphere and soil are calculated. Furthermore, dose rates, a measure for effects of radiation exposure, are calculated for all considered particle species, as well as for a broad range of surface elevations, as these show different radiation conditions for a given environmental scenario.

1.2. MSL/RAD

The second main topic of this work deals with calibration work undertaken for the Radiation Assessment Detector (RAD). The RAD-relevant findings presented in this work constitute crucial research for the ability to analyse the measured data on the Martian surface. To reduce bandwidth the measured data will be onboard processed and, for the most part, only the reduced data packages will be transmitted back from Mars to Earth. So, to be able to conduct Earth-based scientific analysis of the data, it is important that the processing logic of the instrument is functioning properly. This work addresses, in particular, the onboard processing of charged particles.

For a better understanding of this subject the following sections aims to shortly describe both the Mars Science Laboratory (MSL) mission, of which RAD is part of, as well as the RAD instrument itself. A more detailed description of RAD's behaviour for charged particle detection is given in the appropriate Ch. 7.

1.2.1. Mars Science Laboratory

MSL is a Martian surface mission, planned and developed under the patronage of the National Aeronautics and Space Administration (NASA). It consists of a rover (*Curiosity*) that is equipped with several scientific instruments, such as cameras, spectrometers, environmental and atmospheric sensors, and the radiation detector RAD. This instrument is described in more detail below in Sec. 1.2.2. Fig. 1.1 shows an artist's impression of the Curiosity rover on Mars.

The MSL mission is part of NASA's Mars Exploration Program, for which the four main science goals are as follows:

- Determine whether life ever arose on Mars
- Characterize the climate of Mars
- Characterize the geology of Mars
- Prepare for human exploration

The aim of the mission is to contribute to these four main goals via the following mission objectives.

Biological objectives:

- Determine the nature and inventory of organic carbon compounds
- Inventory the chemical building blocks of life (carbon, hydrogen, nitrogen, oxygen, phosphorous, and sulfur)

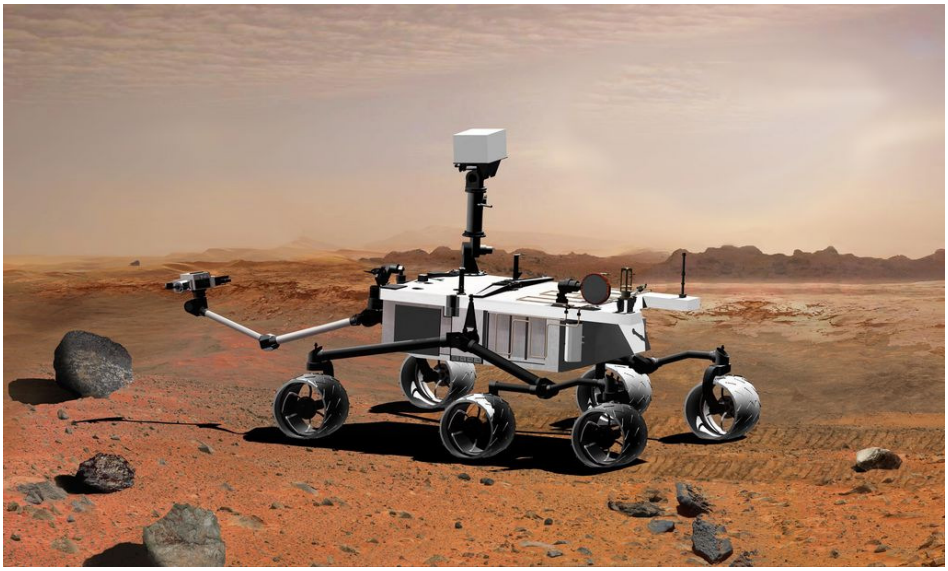

Figure 1.1.: Artist's concept of the MSL rover on the Martian surface. Taken from `http://marsprogram.jpl.nasa.gov/msl/multimedia/images/`.

- Identify features that may represent the effects of biological processes

Geological and geochemical objectives:

- Investigate the chemical, isotopic, and mineralogical composition of the Martian surface and near-surface geological materials
- Interpret the processes that have formed and modified rocks and soils

Planetary process objectives:

- Assess long-timescale (i.e., 4-billion-year) atmospheric evolution processes
- Determine present state, distribution, and cycling of water and carbon dioxide

Surface radiation objective:

- Characterize the broad spectrum of surface radiation, including galactic cosmic radiation, solar proton events, and secondary neutrons

Curiosity was launched successfully on November, the 26$^{\text{th}}$ of 2011 and is currently on its way to Mars where it is slated to arrive in August 2012. The landing site is the Gale Crater near Elysium Planitia at 4°36'S 137°12'E / 4.6°S 137.2°E. The surface mission duration is scheduled to be at least 1 Martian year (687 Earth days).

1.2.2. Radiation Assessment Detector

As mentioned above, one of the instruments on-board the MSL rover is the radiation detector RAD. In this section, a brief description of the instrument is given, a more elaborate explanation of RAD's functionality may be found in [*Kortmann*, 2010] or [*RAD Proposal*, 2006]. RAD was developed by the department of Extraterrestrial Physics at the Christian-Albrechts-Universität (CAU) Kiel, in collaboration with the Southwest Research Institute (SwRI) (San Antonio, Texas), overseen by the German Aerospace Center (Deutsches Zentrum für Luft- und Raumfahrt (DLR)) and NASA. The left of Fig. 1.2 shows a picture of the RAD flightmodel, the right side shows the MSL rover. As RAD is implemented in the inside of the rover, the instrument itself is not visible but the light-shaded cone shows the upward-directed field-of-view RAD would have.

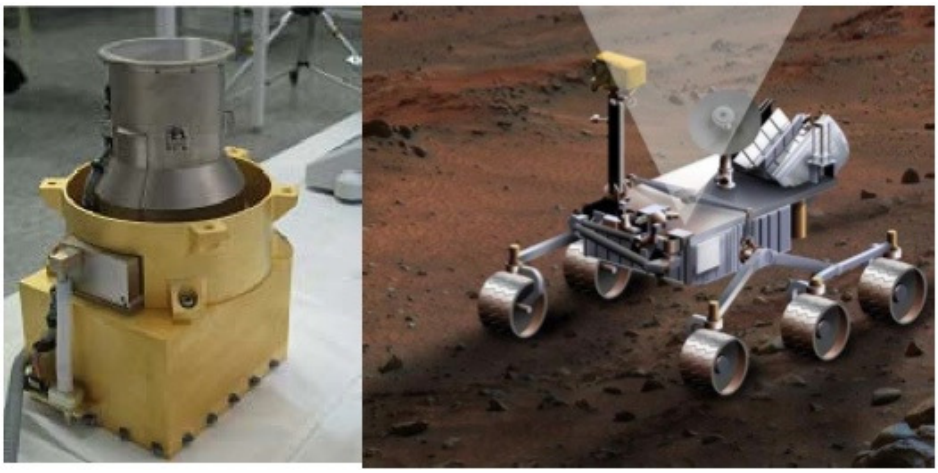

Figure 1.2.: Left: Picture of the RAD flightmodel. Right: Artist's impression of the MSL rover. The light shaded cone indicates the field-of-view of RAD implemented in the rover.

One of the scientific goals of RAD is to characterize the radiation environment on the surface of Mars, measuring charged particles, as well as neutral particles [*RAD Proposal*, 2006]. As can be seen in the schematic on the left in Fig. 1.3, the instrument's sensorhead consists of five particle detectors A, B, C, D, E, and an Anti-Coincidence (AC) made up of F1, F2. The detectors A, B, and C are Solid-State Detectors (SSDs) made of silicon. D is consists of CsI, whilst E, F1, and F2 are plastic scintillators. To detect neutral particles RAD uses the D and E detectors. However, as charged particles also can make signals in these detectors, F1, F2, and additionally C, are used as a tight AC for the neutral particle detection. As the scintillators are of different

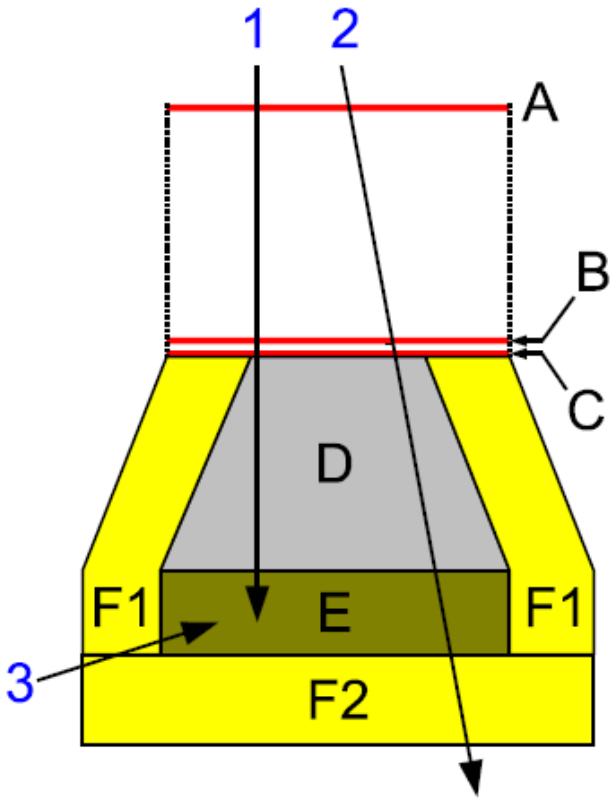

Figure 1.3.: A schematic of the RAD sensorhead. The numbered arrows indicate different possible particle tracks. Track 1 shows a particle stopping in E, track 2 a penetrating particle. Track 3 shows a particle stopping in E, but entering the detectorhead from the side through the AC. Taken from [*Kortmann*, 2010].

materials, they can further be used to distinguish between neutrons and gamma rays, i.e. D is more sensitive to gammas, E to neutrons. As mentioned, charged particles can be detected in all detectors, but RAD requires at least a coincidence in A and B for a successful measurement. A more detailed detection concept can be found in Ch. 7.1.

1.3. Structure of this work

This section gives an outline of how the following chapters of this thesis are structured. As mentioned above the research conducted for this work can be broken down into two topics: The radiation exposure simple life forms would have been subjugated to on early Mars, and the calibration of the RAD instrument's internal logic to process charged particles. Both parts have in common that they deal with radiation conditions on Mars and so a broader knowledge on the formation of this radiation field, as well

as conditions on current and ancient Mars, is necessary for the understanding of this work.

Therefore, in chapter 2, first, background information on the creation and propagation of GCRs and their interactions with planetary atmospheres is given. Next, possible interactions between ionising radiation and matter are described, as well as the effects of radiation on organic matter and, in particular, simple, unicellular life forms. Last, certain dosimetric terms, used to quantify radiation exposure, are introduced.

Chapter 3 focuses on the planet Mars. After a description of its physical characteristics, relevant information on its present-day surficial, hydrological, and atmospheric properties is given. Subsequently, the current state of research on the early Mars of about 4 Ga ago is presented, as well as how this knowledge about ancient Mars is gained. As a conclusion, it is described how conditions on early Mars could have changed to the present-day status.

In the next chapter, the model for the analysis of the radiation environment is introduced. For this work, a Monte-Carlo (MC)-based analysis code was developed to calculate the radiation exposure under different atmospheric conditions on present-day and early Mars. The underlying MC toolkit `GEANT4` and its application `PLANETOCOSMICS` are described. Furthermore, an overview is given how present-day Martian features are pre-implemented in this application, as well as how it was adapted to consider certain early-Mars-like conditions in the developed analysis code. At the end of the chapter, a description how the model derives dose rates from calculated particle fluxes for a given radiation environment is given.

In chapter 5, the results from the above mentioned simulations are presented. This chapter is subdivided into three parts. First, the influence an increase of atmospheric pressure would have on the surface radiation exposure (in terms of particle fluxes and absorbed dose rates) is analysed. In the second subchapter, an analysis of the subsurface radiation exposure under the above mentioned conditions is given, as an emergence of life is not constricted to the surface of a planet. Third, the influence of water (in liquid or ice form) is analysed.

Subsequent to these results, chapter 6 gives implications on how the findings presented here might affect the chances of emergence and sustainment of simple life on Noachian Mars. Additionally, an estimation of the amount of radiation, other sources than the GCR-induced radiation field contribute to the radiation exposure on Mars, is given.

Chapter 7 represents the second main topic of this thesis. The approach for calibrating the RAD charged-particle detection is introduced. For this, an analysis code was developed that mirrors the instrument electronics' on-board processing logic. By applying the code to measured calibration data, certain cut values and trigger thresh-

olds are determined, which the onboard logic will use to identify charged particles, and, subsequently, charged penetrating or stopping particles. To help with the calibration, simulations of different energetic particle species with a `GEANT4` model of the detectorhead are conducted. The results from these simulations are also presented and compared to the data from the calibration runs.

The final chapter gives a concluding summary of the findings presented in this work and offers an outlook on possibilities of further research based on the developed models. The subsequent appendix contains information that is not directly necessary for the understanding of this work but nonetheless complements the presented research and furthers the understanding.

2. Theoretical Background

In this chapter, an overview of several topics relevant to the understanding of this work will be given. To be able to analyse and comprehend the research presented in this thesis, it is important to understand how the radiation field on the Martian surface is created. Therefore, insight on the origin, propagation, and modulation of galactic charged particles, that are mainly responsible for the creation of said radiation field, is provided. Furthermore, important processes of particle-matter interactions with relation to their effect on atmospheric and organic matter are described. Additionally, basic definitions and concepts relevant of the field of radiation dosimetry are introduced.

2.1. Galactic Cosmic Rays

The radiation environment on the Martian surface, which constitutes one of the main subjects of this work, is to a large amount influenced by energetic charged particles entering the Martian atmosphere. These particles are so-called Galactic Cosmic Rays (GCRs), originating somewhere outside our Solar system in our galaxy. This section will give an overview of the creation of these GCRs, the processes they are subject to before they reach the Martian atmosphere, as well as their interaction with planetary atmospheres. For further insight on the topic of GCRs, the reader is referred to [*Allkofer*, 1974].

As mentioned previously, GCRs are energetic charged particles. They are comprised of 98% atomic nuclei and 2% electrons. The nuclei show a composition of 87% protons, 12% helium, and 1% heavier nuclei ($Z \geq 3$) [*Simpson*, 1983]. The energy range of GCRs extends to roughly 10^{18} eV, whereas cosmic rays with even higher energies (up to 10^{21} eV) are considered to be of extragalactic origin (as the flux of these latter particles is distinctively low, they are not further covered in this work).

Fig. 2.1 shows energy spectra of different particle types of GCRs. One can see that for higher energies the distributions can be approximated by a power law (with a spectral index γ depending on the ion species). Furthermore, it can be nicely seen that protons are the most dominant species and the fluxes of the other species are comparably low.

The current understanding of GCR creation is that they originate mainly from Supernova (SN) explosions. Given generally assumed occurrence rates (2 SN explo-

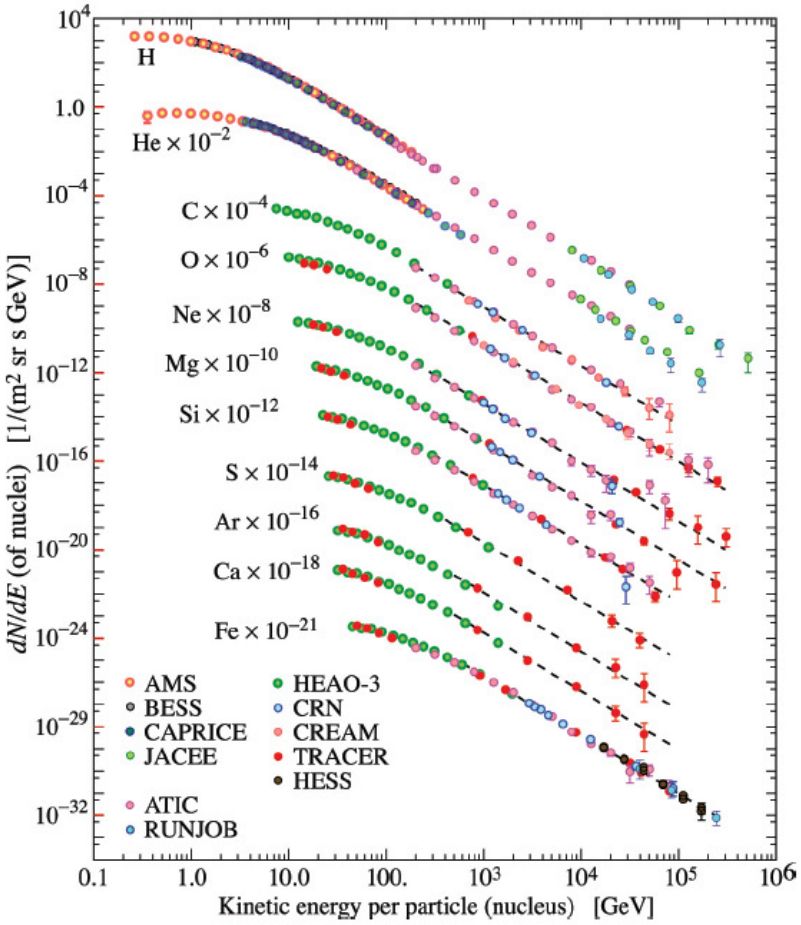

Figure 2.1.: GCR spectrum for selected particle types. Taken from [*Amsler et al.*, 2008].

sions per hundred years) and energy releases (10^{51} erg), the kinetic energies released by such events are believed to provide sufficient energy for the estimated radiant power of GCRs in the Milky Way ($\sim 10^{41}$ $\frac{\text{erg}}{\text{s}}$) [*Prantzos*, 2011]. Furthermore, the creation of shock waves by such Supernova Remnants (SNRs) can explain, how GCRs are accelerated to their observed energies of 10^{15} eV, and possibly even up to 10^{18} eV [*Hillas*, 2005].

As GCRs are charged particles, they are constantly deflected by magnetic fields during their propagation through the galaxy, which is why they are isotropically distributed when arriving in the Solar system. When GCR particles enter the heliosphere they are modulated by the Sun [*Heber et al.*, 2006]. The main driver for this modulation is the Solar magnetic field, which changes with the Solar activity. Thus, a higher Solar activity results in a lower GCR flux in the heliosphere and vice versa. This anti-correlation can be observed in Fig. 2.2, where count rates of the Kiel Neutron Monitor (upper

panel) and the sunspot number (lower panel) are shown for the same time frame. The

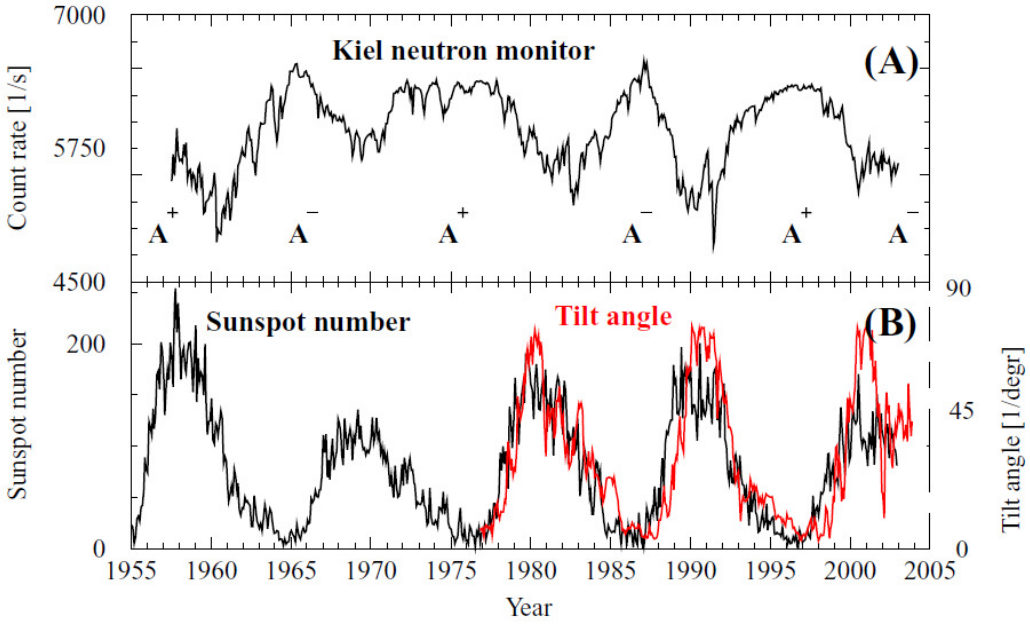

Figure 2.2.: Solar modulation of GCRs. In panel (A), the count rates of the Kiel Neutron Monitor, which serves as a measure for the GCR flux, is shown. Panel (B) shows the sunspot numbers observed on the Sun (black line), a measure for Solar activity, and the tilt angle of the current sheet (red) in the same time frame. Note that the tilt angle, however, is not further considered in this discussion. Adapted from [*Heber et al.*, 2006].

Solar modulation mainly affects the lower-energetic GCRs. While the high-energetic tails of the particle spectra stay constant, the particle fluxes for energies below the flux maxima are strongly affected, resulting in lowered intensities in the low-energetic tails of the GCR spectra.

2.1.1. Interactions with planetary atmospheres

Now, when a primary GCR particle reaches a planetary atmosphere – in this case the Martian, but the principle holds true for other planets as well – it can interact with the molecules of this atmosphere when propagating through it. As a result, such a primary particle can create other secondary particles on its way. To add to that, the deeper it propagates into the atmosphere, the denser the latter gets and the interaction probability increases accordingly. All this leads to the creation of so-called air-showers or secondary particle cascades in the atmosphere, where one primary can be responsible for creating cascades consisting of up to millions of secondaries. The principle of such

a particle cascade is illustrated in Fig. 2.3 and will be explained in more detail in the following, whereas the underlying, physical processes will be explained further below in Sec. 2.2.1.

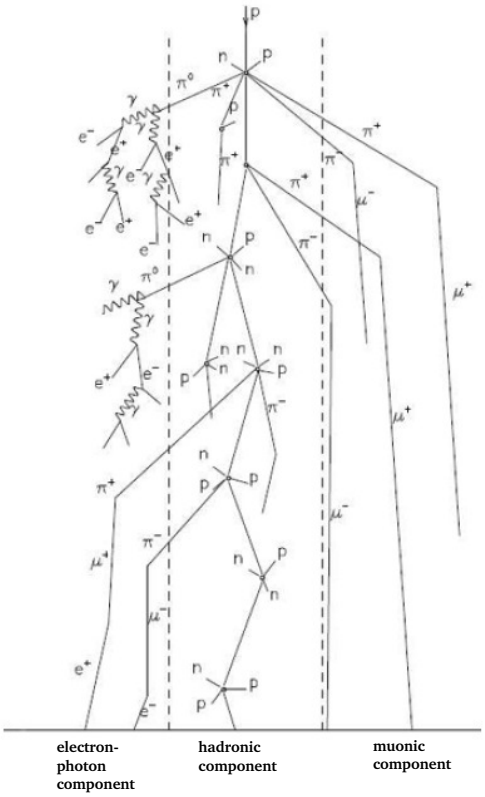

Figure 2.3.: Schematic of the development of a particle cascade in a planetary atmosphere, with the distinction in three different branches (from left to right: electron-photon component, hadronic component, muonic component) [*Allkofer*, 1974].

As described by *Allkofer* [1974], a particle cascade can be divided into three different branches, corresponding to the ones seen in Fig. 2.3:

- the hadronic component,
- the electron-photon component,
- and the muonic component.

As illustrated in Fig. 2.3, the hadronic cascade is generally the starting point of an atmospheric air shower. It forms when primary particles undergo interactions with the nuclei of the atmosphere. For one, an incoming GCR particle, in most cases a

proton, can lose energy by ionisation or excitation, when interacting with electrons of atmospheric molecules or atoms. Another possibility for primaries is to undergo inelastic interactions with atmospheric nuclei, thereby creating nucleons and mesons (mostly pions) via spallation (see Sec. 2.2.1). Subsequent to that, a possible excitation of the nucleus can lead to creation of further lower-energetic nucleons, and sometimes even alpha particles or nuclei fragments. Additionally, primary heavy ions will fragment with their first interaction in the atmosphere, yielding lower-Z fragments that might propagate further. In general, primary particles can traverse through the atmosphere, as long as any interaction leaves them with enough energy to go on, advancing the cascading effect deeper into the atmosphere.

As mentioned above, mesons produced in these hadronic cascades are mostly pions. Charged pions decay into muons and neutrinos, either via $\pi^+ \rightarrow \mu^+ + \nu_\mu$ or $\pi^- \rightarrow \mu^- + \bar{\nu}_\mu$, depending on their charge, which leads to the muonic component of the air shower. Even though muons have a rather short lifetime of $\sim 2.2 \cdot 10^{-6}$ s, relativistic muons can still travel relatively deep into the atmosphere. This is due to time dilatation effects and further due to the fact that muons mainly lose energy by ionisation (and not significantly through other interactions) when travelling through the atmosphere.

The electron-photon component of the air shower can, for example, be started by neutral pions created in the hadronic cascade. These pions decay into two gamma rays ($\pi^0 \rightarrow \gamma + \gamma$). Given high enough energies, these gammas can then create subsequent electron/positron pairs (via pair production), which can then, in turn, create gamma rays via bremsstrahlung (or annihilation of a e^-/e^+ pair), and so on, as long as these particles still have enough energy for further processes.

If particles of such an extensive air shower reach the ground of a planet, they can, of course, also undergo interactions with the molecules in the soil. This leads to a GCR-induced radiation field on a planetary surface, not only made up of particles cascading down from the atmosphere, but also from particles scattering back from the ground. An exemplary schematic of the situation can be seen in Fig. 2.4, where on the left a primary proton is stopped in the atmosphere and a large part of secondaries produced by its propagation through the atmosphere cascade down to the ground. The right side shows a higher-energetic proton that propagates to the ground and creates secondaries by interacting with the soil.

Other particle sources

In addition to the particle field induced by GCRs, there are other particle sources that can interact with a planetary atmosphere or soil. The main contributors, here, are Solar Energetic Particles (SEPs) and Ultra-Violet (UV) radiation, both originating from the

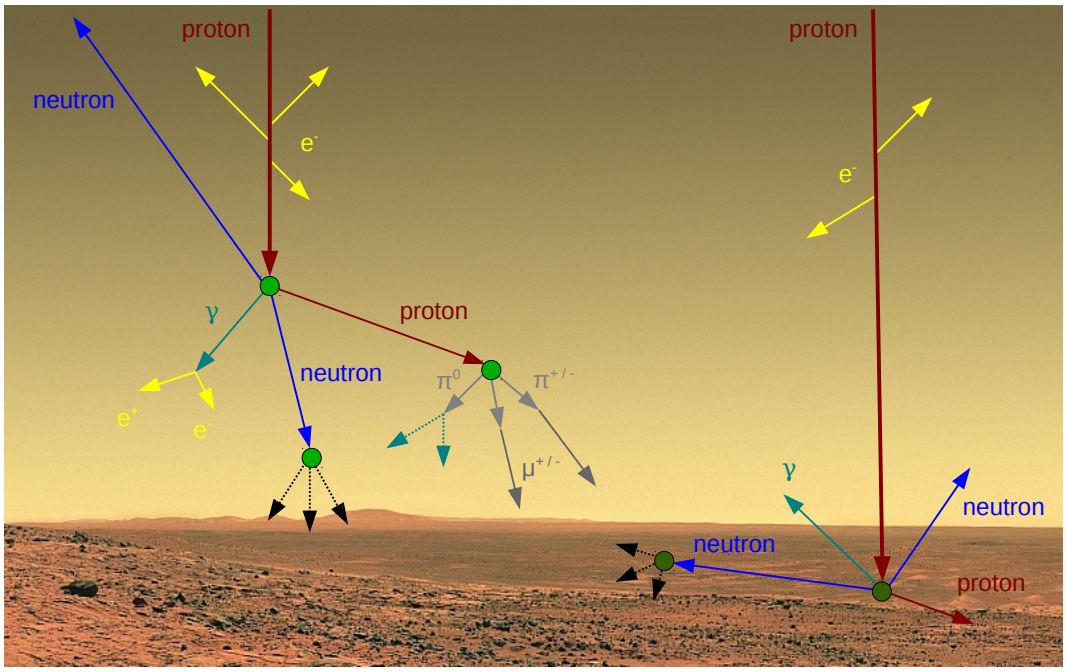

Figure 2.4.: Schematic of primary GCRs propagating through the Martian atmosphere for the exemplary cases of two primary protons with different energies. The lower-energetic one (left) is stopped somewhere in the atmosphere and only its secondaries can cascade further to the ground. The proton on the right has high enough energy to reach the soil and interact with the molecules in the ground, creating secondary particles in the soil. Note that on the right, for the sake of simplicity, further interactions of the proton with atmospheric molecules are not sketched. Background picture adapted from `http://www.db-prods.net/marsroversimages/galerie.html`. Credits: NASA / JPL / CalTech / Damien Bouic.

Sun. As this work focuses on the interactions of GCRs, these other sources will only be briefly discussed in this section.

SEPs are energetic particles (protons, heavier ions, electrons) emitted from the Sun and accelerated by Solar flares or Coronal Mass Ejection (CME)-driven shock fronts. In general, they can reach energies of up to several hundred MeV (for strong events higher energies are possible). Compared to the GCR spectrum, they can reach significantly higher fluxes, as illustrated in Fig. 2.5 where GCR fluxes for Solar minimum and maximum conditions, and the peak flux of Solar protons for the September 29 1989 event with its intensity scaled to Martian orbit are compared. Furthermore, as SEPs originate from the Sun, their occurrence rate and fluence are correlated to the

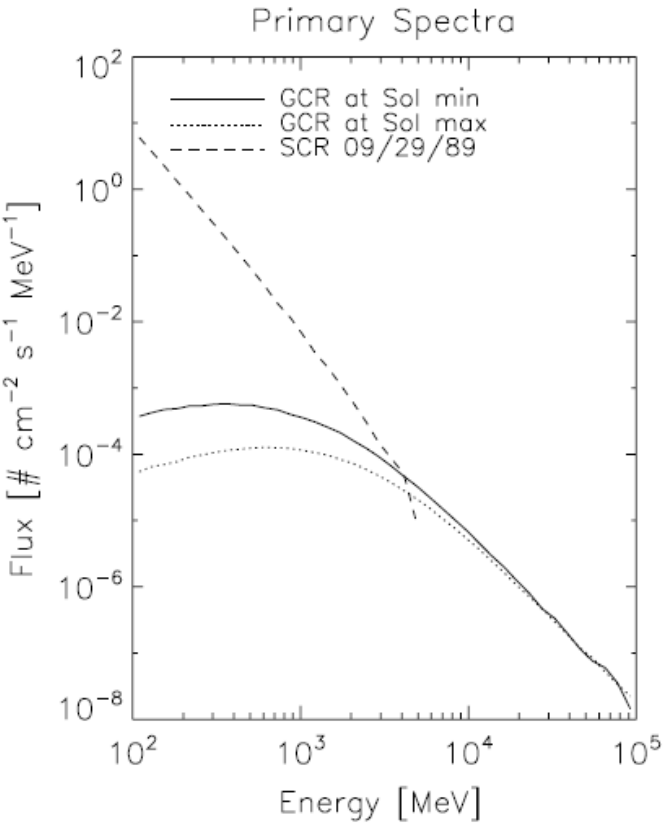

Figure 2.5.: Comparison of GCR and SEP proton fluxes, for the example of the September 29, 1989, event. Shown are the GCR flux at Solar minimum (solid line) and maximum (dotted), and the SEP peak flux (dashed) with intensity scaled to Martian orbit. Taken from [*Gurtner et al.*, 2005].

Solar activity, e.g. during Solar maximum the number of Solar Particle Events (SPEs) is higher [*Barnard and Lockwood*, 2011].

In the context of this work, SEPs are insofar of interest, as present-day Mars does not possess a good protection against higher-energetic SEPs, due to its thin atmosphere and missing magnetic field [*Leblanc et al.*, 2002]. Although no calculations for SEP-induced dose rates were conducted in this work, relevant findings from other research regarding this topic are presented and brought into context in Ch. 6.

Solar UV radiation is a part of the radiation constantly emitted by the Sun, with wavelengths in the range of 10 – 400 nm, respectively energies between 3 – 124 eV. On Earth, we are protected from UV radiation propagating through the atmosphere by the ozone layer. Furthermore, the magnetic field protects the part of the atmosphere, that is ionised by UV radiation, from Solar wind erosion. On Mars, where a global

magnetic field is missing, this erosion takes place and the Solar wind can sweep the atmospheric ions away [*Pérez-de-Tejada et al.*, 2009]. Furthermore, as Mars possesses no significant ozone shielding, even far-UV radiation can reach the Martian ground, creating highly hazardous effects for simple life forms, such as rapid deactivation of cells directly exposed to the resulting UV environment on the surface ([*Cockell and Raven*, 2004], and references therein).

2.2. Radiation and dosimetry

Traversing through matter, radiation interacts with molecules or atoms. This section introduces the basic forms of interactions, as well as, in particular, describes the resulting effects on organic matter, such as cells or Deoxyribonucleic acid (DNA) strands.

2.2.1. Interaction of radiation and matter

Sec. 2.1.1 introduced possible interaction processes for radiation and planetary atmospheres. This section, now, aims to describe some of the basic, underlying physical processes, as well as placing them in a more general context, i.e. radiation can not only interact with atmospheric molecules but, naturally, also with other kinds of matter. For elaborate insight on particle-matter interactions refer to [*Allkofer*, 1974] and [*Bethge*, 1996].

If a charged particle propagates through matter, the main energy loss processes that occur are ionisation and excitation of the target matter via inelastic scattering. Note that elastic scattering, such as Coulomb scattering, can also occur. However, as in this case the incident particle's energy is conserved, the topic will not be dwelled upon. Ionisation or excitation happens as the incoming particle interacts with the shell electrons and thereby loses energy, which in turn is used to excite or ionise the atomic target material. If the energy of an incoming particle is high enough compared to the energy loss by one single interaction, this yields an ongoing process of interactions for a certain path length. Then, the total energy loss dE of a charged particle along the path length dx through the target matter can be described by Eq. 2.1, the Bethe-Bloch formula:

$$-\frac{dE}{dx} = \frac{4\pi N Z z^2 e^4}{m_e v^2 A}\left[ln\left(\frac{2m_e v^2}{I(1-\beta^2)}\right) - \beta^2\right], \tag{2.1}$$

with N being the Avogadro's number, Z, A the atomic number and mass of the target matter, ze the charge of the incoming particle, m_e the electron mass, v the velocity of the particle, I the effective ionisation potential of the target, and $\beta = \frac{v}{c}$. There are further correction terms for the Bethe-Bloch equation, such as the shell correction and corrections for density effects at high energies, which are not introduced here.

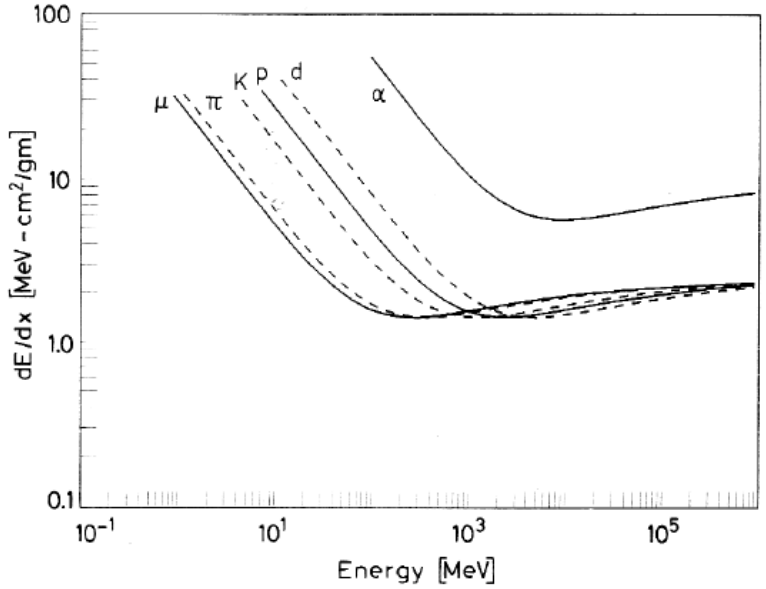

Figure 2.6.: Energy loss according to the Bethe-Bloch formula for different particle species versus the incident particle's energy. Taken from [*Leo*, 1994].

Fig. 2.6 shows the specific mean energy-loss spectra, derived from Eq. 2.1, for different particle types. As one can see, all species show a distinct minimum value in their energy-loss distribution. Although the shape of the spectra is similar for all particle types, the positions of these minima (and the general characteristics of the spectrum) lie at higher energies for higher-charged particles. Furthermore, the mean energy loss of the minimum is also higher, the higher the charge of the species.

As the interaction cross section with the matter increases for decreasing particle energy (at least at lower energies than the minimum position of the curve), the energy loss increases with distance traversed. If the depth of matter is high enough, the energy loss reaches a peak value, the so-called Bragg peak, and thereafter decreases rapidly to zero and the particle is stopped in the material.

Another inelastic interaction is the so-called spallation. When an incoming charged particle impacts the target matter, it interacts with the nucleons of the target nucleus. These nucleons, now, can interact with further nucleons, leading to a cascading effect inside the nucleus. During this process, some high-energetic nucleons (with energies up to the energy of the impacting particle) are emitted. Furthermore, if the impacting particle has high enough energy, an emission of mesons, mostly pions, can occur. This leaves the target nucleus in a highly-excited state, where the transferred energy is equally distributed over the remaining nucleons. In a secondary spallation step, the

nucleus boils off further nucleons, or even fragments of the nucleus.

Accelerated charged particles can also lose energy via the emission of radiation, called bremsstrahlung. This occurs when the charged particle is deflected and thereby decelerated in the electric field of an atomic nucleus. In this process, the energy loss is antiproportional to the square of the mass of the particle, or $\frac{dE}{dx} \sim m^{-2}$, from which it can be seen that bremsstrahlung plays a more prominent role for lighter particles, such as electrons.

If a charged particle and its antiparticle collide, they can annihilate each other. The most common case is the annihilation of an electron and a positron where two gamma photons, each with 511 keV and opposite directional vector (due to conservation of energy and momentum), are created ($e^- + e^+ \rightarrow \gamma + \gamma$). Somewhat reverse to this process is the so-called pair production that can occur if a gamma photon interacts with a target nucleus and converts into an electron/positron pair ($\gamma \rightarrow e^- + e^+$). The minimum needed energy of the gamma for this process is twice the rest energy of the electron, or $E_{min,\gamma} = 1.022$ MeV. If the gamma photon has a higher energy, this additional energy is converted into kinetic energy of the electron and positron.

Besides from pair production there are two further main processes by which gamma photons interact with matter: Compton scattering and the photoelectric effect. The latter process is dominant at lower energies (10 keV to 1 MeV), whereas Compton scattering becomes more important from 1 MeV on [*Allkofer*, 1974]. The photoelectric effect describes the absorption of a photon by an atom, during which an electron with the photon's energy minus the binding energy is emitted. During Compton scattering, which is an inelastic scattering at an atomic electron, the gamma photon transfers some of its energy to the scattering electron.

Neutrons, having no charge, interact with matter via the strong interaction with atomic nuclei. Fast neutrons undergo elastic scattering at nuclei, transferring part of their initial energy to the now energised nucleus. Such a recoil nucleus can then lose its energy by ionisation while propagating through the target matter. The energy transferred during such elastic scattering thereby depends on the mass of the nucleus. The lighter the nucleus is, i.e. the more similar its mass is to the mass of the neutron, the higher the energy that can be transferred. Therefore, hydrogen is especially well-suited for this slowing down of neutrons. Inelastic scattering can also play a role in neutron-matter interactions. Here, the target nucleus absorbs the incoming neutron, and then, at high enough initial neutron energy E_0, re-emits a neutron with an energy E' smaller than the initial energy, along with a gamma photon with the energy $E_\gamma = E_0 - E'$. The cross section for inelastic scattering increases with the size of the nucleus and with increasing initial neutron energies. High-energetic neutrons can also undergo compound nucleus reactions with the target material, i.e. spallation of target nuclei. Neutrons of

sufficiently low energies, i.e. thermal neutrons, can be captured by nuclei. Here, the neutron is absorbed by the target nucleus, which ends up with a mass number increased by 1 and emits a gamma photon (but no neutron as in the inelastic scattering process).

2.2.2. Effects of radiation on organic matter

In the previous sections, it was established how a GCR-induced radiation field can be created in a planetary environment. To, now, be able to draw conclusions from such a presence of a radiation environment on hazards to or obstacles for a development of life, it is important to understand the influence of ionising radiation on life forms. Therefore, in this section, the effects radiation has on organic matter are described.

As mentioned, when radiation traverses matter, it can deposit energy via ionisation and excitation of electrons in the target matter. In organic cells, which comprise to 40 – 70 % of water, this ionisation can lead to direct deactivation of biomolecules, e.g. DNA molecules or proteins, or indirectly via creation of radicals that interact with biomolecules, deactivating them [*Baumstark-Khan and Facius*, 2001].

Depending on the radiation exposure, the DNA damages can range from repairable, e.g. single- or double-strand breaks, to irreparable. These irreparable damages, in turn, can have various effects from, e.g., the damage leading to programmed cell death to prevent genetic damage, over nonlethal DNA mutation, to damage that leads to transcription errors and, therefore, to cell malfunctioning, and e.g. leading to cancer.

Unicellular life forms

If life possibly emerged on Mars, it would have mostly likely been in the form of unicellular microorganisms, e,g, bacteria. Therefore, here, some basic principles regarding survival possibilities of these simple life forms under exposure to ionising radiation are introduced.

In general, when talking about survival chances or rates of cells, one looks at the ability of sustained reproduction [*Baumstark-Khan and Facius*, 2001]. For unicellulars, survival rates are normally coupled to the Colony Forming Ability (CFA) of such microorganisms, meaning a single organism retaining its ability of reproduction and colony forming. As described by *Barendsen* [1992], a loss of CFA is seen equal as the cell death. To, now, classify the survival chance of these organisms, the so-called D_{37} value is used, which gives the dose (for the definition of dose, see Sec. 2.2.3) required to reduce the fraction of surviving cells of an irradiated test population to e^{-1}, and is the value stated for the loss of CFA of the organism [*Battista*, 1997]. To determine this value, a cluster of cells is irradiated with increasing doses. By comparing the fraction of surviving cells to the non-irradiated number of cells for different irradiation doses, a

survival curve (fraction of surviving cells over dose), showing a continuous decrease, is yielded and the D_{37} value is determined. On Earth, we find bacteria in a wide range of radiation resistances. For example, the common *E. coli* bacteria, found in the human gut, has a D_{37} of 30 Gy (for an explanation of the unit Gy, see Sec. 2.2.3), while the extremophilic *Deinococcus radiodurans* has a D_{37} value of $\sim$ 6000 Gy.

2.2.3. Dosimetry

In general, the field of radiation dosimetry deals with measurements and calculations of ionising-radiation-induced energy deposits in matter and tissue. For this, the common measure is the absorbed dose D, which states the energy dE deposited in a volume with the mass dm by ionising radiation, and is given in Gray (Gy), with 1 Gy = 1 J/kg:

$$D = \frac{dE}{dm}. \tag{2.2}$$

However, when evaluating radiation risks for humans, one has to be aware that different types of radiation can be differently hazardous. Absorbed dose is more of an absolute measure of energy deposited in a target volume and can, for example, not account for how the energy is transferred. Highly-ionising, charged particles deposit their energy along rather linear, dense tracks, with the amount of energy loss per track length following the Bragg curve, with the Bragg peak of highest energy loss at the end of the ionisation track. Furthermore, they can, as shown, create secondary particles in the matter that can then ionise and cause biological damage on their own, leading to deposit track lengths exceeding the range of the primary particle. Neutrons follow the same principle, as they deposit their dose only indirectly. For example, in organic cells, which mostly consist of water, they transfer their energy via elastic scattering to hydrogen, creating energetic recoil protons that ionise the target along their track through the matter. Ionising photons, e.g. gamma rays, undergo scattering processes during each interaction with the target, creating energy deposits over a wider range and on non-linear tracks in the matter. Additionally, their energy loss over traversed depth shows an exponential decay [*Nelson*, 2003].

In general, one can say that charged particles are more biologically damaging than energetic photons depositing the same absorbed dose. For charged particles, this gradient increases with high energies and high atomic numbers of the particle [*Baumstark-Khan and Facius*, 2001].

Therefore, a further radiation dosimetry unit was introduced by the International Commission on Radiological Protection (ICRP), the dose equivalent H. For its calculation a quality factor Q, which accounts for the differing biological effectiveness of

different types of ionising radiation, is applied to the absorbed dose D:

$$H = Q \cdot D. \tag{2.3}$$

As the quality factor is dimensionless, the unit for the dose equivalent is the same as for the absorbed dose, but to indicate that the biological effectiveness is considered the dose equivalent is given in Sievert (Sv), rather than Gy, with 1 Sv = 1 J/kg. To create a reference value for the differing types of ionising radiation, the quality factor for lowly-ionising photons (e.g. gamma rays) was set to Q = 1. According to *ICRP60* [1991], the quality factor for charged particles is coupled to the particle's Linear Energy Transfer (LET) in water, as can be seen in the upper panel of Table 2.1. In this context, the LET describes the energy dE transferred to a material by a traversing ionising particle on a path length dx. The Q for neutrons is coupled to the initial neutron

Table 2.1.: Quality factors for charged particles and neutrons, according to *ICRP60* [1991]. For charged particles the factor depends on the particle's LET in water (upper panel). For neutrons, the factor depends on the neutron's initial kinetic energy (lower panel).

Charged particle	
Linear Energy Transfer	Quality factor Q
LET < 10 keV/µm	1
10 keV/µm < LET < 100 keV/µm	0.32 · LET - 2.2
LET > 100 keV/µm	$\frac{300}{\sqrt{\text{LET}}}$
Neutrons	
Energy	Quality factor Q
E_{kin} < 10 keV	5
10 keV < E_{kin} < 100 keV	10
100 keV < E_{kin} < 2 MeV	20
2 MeV < E_{kin} < 20 MeV	10
20 MeV < E_{kin}	5

energy (seen in the bottom panel of Table 2.1).

Note that in the scope of this work, we concentrate on the absorbed dose. The analysis of the radiation environments in this work is conducted with the idea in mind to estimate the effects these environments would have on a possible emergence of simple life forms. And for unicellulars radiation exposure hazards are usually stated in absorbed dose values (e.g., see the D_{37} value in Sec. 2.2.2), as it is not ascertained how well the defined, human-based quality factor applies to simple bacterial life forms. Calculated

dose equivalent rates are, therefore, placed in the appendix (App. A.3) and not discussed in the same detail as the absorbed dose values.

3. Mars

Going from the Sun, Mars is the fourth planet in our Solar system, orbiting the Sun with a period of 687 days on an orbit with a semi-major axis of 228 million km, respectively $\sim$ 1.5 AU. Mars is smaller and lighter than Earth, with a radius of $\sim$ 3400 km, which corresponds to roughly 0.5 r_{Earth}, and about 11% of the Earth's mass.

Due to its relative vicinity to Earth – during opposition Mars approaches Earth as nears as 0.37 AU (2003) – Mars has a long history of Earth based observations, even dating back to ancient Egypt. Especially since the beginning of telescopic observations in the early 17^{th} century, Mars has been studied extensively by astronomers, leading to a broad base of knowledge long before the beginning of the Space Age. In particular, the observation of thin dark lines on the Martian surface by the Italian astronomer Giovanni Schiaparelli in 1877 led to increased focus on Mars research, even though this was based on a misunderstanding. Schiaparelli believed these lines to be channel-like structures crossing the surface. The Italian word for channels – *canali* – was, however mistranslated into canals, suggesting artificial creation of these structures. This helped to develop the long-persisting conception that Mars might harbour intelligent life, even after the idea of artificially-built structures was disproved, as could be done with similar misconceptions, e.g. the "Face on Mars".

However, because of Mars' accessibility for scientific research and, also to a large part, driven by the question if life could exist or have existed on Mars, the interest in research and exploration of our neighbour planet remained high. To date, more space missions – with varying success – have been aimed for Mars than for any other planet in our Solar system, only the Earth's moon has seen more mission attempts. In Fig. 3.1, an infographic of the attempted and successful Mars missions from 1960 to 2007 is shown.

Due to its long and extensive history of observation and explorations, it would prove quite a task to provide a complete overview of the current state of knowledge of Mars in the scope of this thesis. For a more detailed look on specific topics, the interested reader is referred to [*Kieffer et al.*, 1992], a most thorough summary of the knowledge and understanding of Martian atmospheric and surficial science, and the subsequent work of *Barlow* [2008], which contains more recent discoveries and findings.

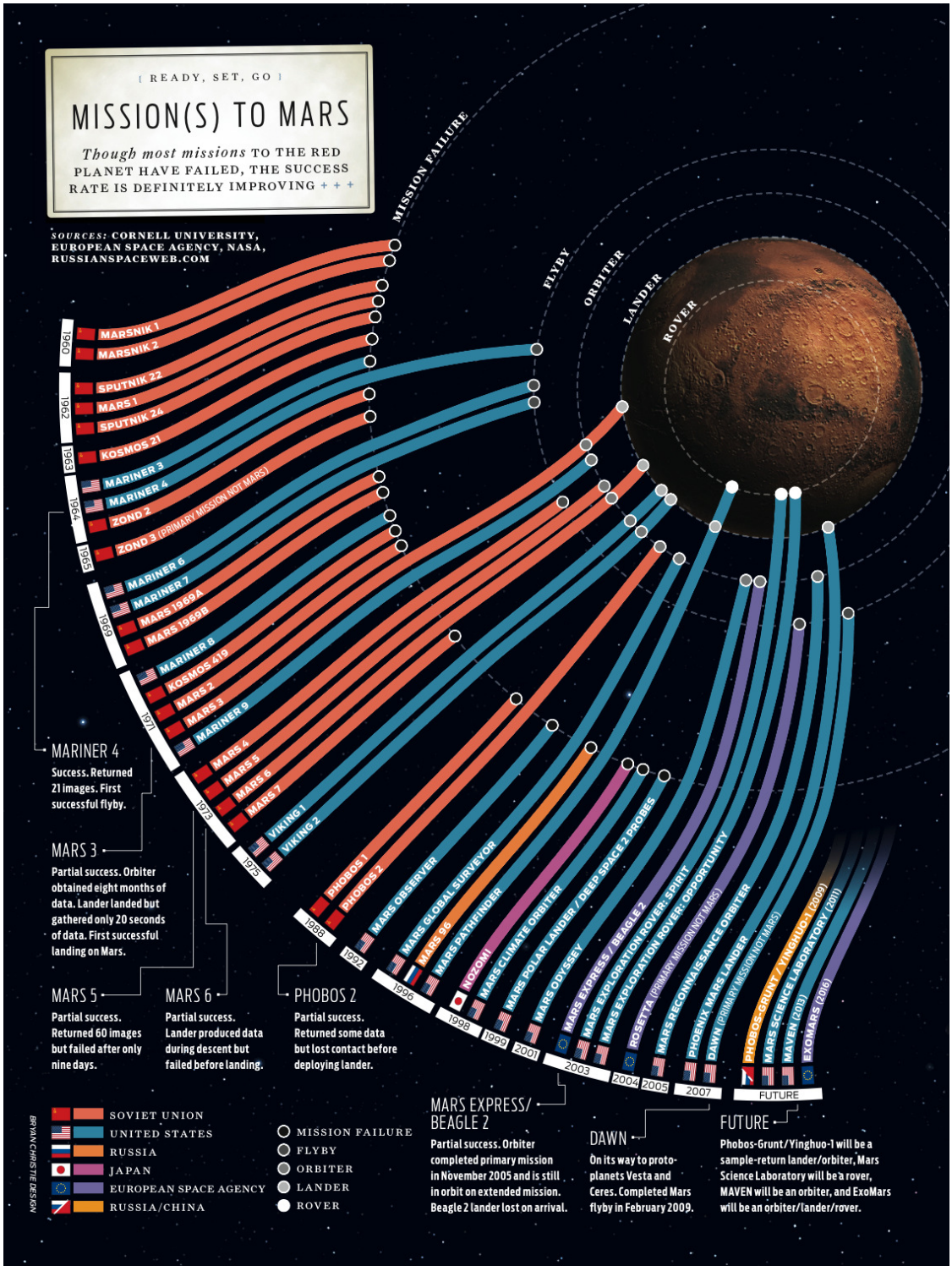

Figure 3.1.: Infographic on previous missions to Mars (as of 2007), divided into the following five categories: mission failure, flyby, orbiter, lander, and rover. Credit: Bryan Christie Design on behalf of IEEE Spectrum.

3.1. Present-day Mars

After having introduced some of Mars' basic physical characteristics, this section briefly describes the modern-day characteristics of Mars, regarding its geography, surface geology, and atmosphere.

Thanks to the Mars Orbiter Laser Altimeter (MOLA), that operated as part of the Mars Global Surveyor (MGS) orbiter mission from 1997 to 2006, the topography of the entire Martian surface was mapped in high resolution. A resulting topographic map of Mars can be seen in Fig. 3.2. One interesting point is the clearly visible dichotomy of

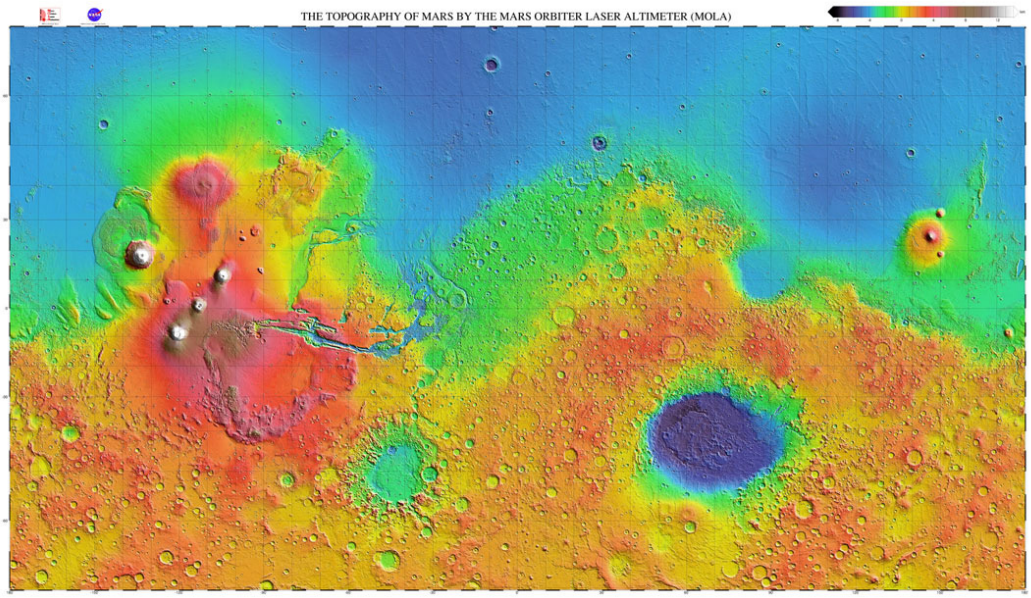

Figure 3.2.: Martian topography as established by the MOLA experiment. Surface elevations are colour-coded from black (lowest) to white (highest) From: `http://mola.gsfc.nasa.gov/images`.

the topography between northern and southern hemisphere which is believed to have been caused by a giant impact within the first 50 Ma of the Solar system formation [*Marinova et al.*, 2008]. Mars, especially in the southern hemisphere, is pockmarked by thousands of impact craters, the largest of which is the Hellas Basin (the large crater in the southeast of the map in Fig. 3.2). Furthermore, with Olympus Mons (height of $\sim$ 22 km), Mars features the largest, planetary mountain in the Solar system. Comparing the elevation differences occurring on Earth and Mars, one can say that the latter shows a much more rugged surface (higher elevation difference), especially when also considering Mars' smaller diameter.

For the study of the Martian surface radiation, induced by extraplanetary radiation,

e.g. GCRs, primarily the topmost layers (the regolith) of the planet are of interest, as the incident radiation only has a limited penetration depth [*Dartnell et al.*, 2007A]. The regolith, or soil, consist mainly of SiO_2, while iron oxides are also featured to a larger degree. The presence of iron oxides in soil and dust further leads to the characteristic reddish hue of Mars (see the left picture of Fig. 3.3 at the end of this chapter). However, the exact composition of the soil can vary from place to place, which – along with differences in the grain sizes of the regolith – leads to the observable colour variations on the Martian surface [*Barlow*, 2008]. An example of the Martian soil composition, as analysed by the Pathfinder-Sojourner mission [*Boyce*, 2002], can be seen in Table 3.1.

Table 3.1.: The composition of the Martian soil, as analysed by the Pathfinder-Sojourner mission. Abundances are normalised to 100 % [*Boyce*, 2002].

Material	SiO_2	Fe_2O_3	Al_2O_3	MgO	CaO	SO_3	Na_2O	TiO_2	other
Abundance (%)	46.8	18.8	8.1	7.7	6.2	6.0	1.5	1.1	3.8

One of the main effects of the present-day conditions on Mars for this work is that it only has a very thin atmosphere. Surface pressures range from roughly 0.3 mbar (highest elevation) to 12 mbar (low elevations). At datum altitude one finds $\sim$ 6 mbar, which corresponds to $\sim 16 \frac{g}{cm^2}$. Note that due to Mars' different surface gravity (about 0.38 g), pressure values on Mars and Earth are not one-to-one comparable, e.g. 6 mbar on the Earth corresponds to $\sim 6 \frac{g}{cm^2}$. However, as pressure is mainly given in mbar in Mars research literature, this unit is also applied in this work. The Martian atmosphere is mainly consisting of CO_2 (about 95 %), along with $\sim$ 3 % N_2, and about 1.5 % Ar, as established by the Viking lander missions in 1976 [*Owen et al.*, 1977].

The average surface temperature is about $\sim$ 218 K, and can range from 140 K at the winter side pole to about 300 K on the day side during Martian summer. Together with the low atmospheric pressure, this means that present-day Mars can not sustain bodies of liquid water for extended periods of time.

However, nowadays, it is affirmed that Mars at least contains larger amounts of water in the form of subsurface water ice. E.g., the permanent part of the northern polar ice cap is believed to be dominated by water ice [*Langevin et al.*, 2005]. The permanent southern polar ice cap is also composed of water ice, however covered by a roughly 8 m deep layer of dry ice (CO_2). Furthermore, as shown by *Feldman et al.* [2004], the northern and southern subpolar, high-latitude belts of Mars are covered by regions of permafrost, with the soil containing on average $\sim$ 20 % (by mass) water ice, with the fraction increasing polewards. Even mid-latitude regions can hold larger amounts of water as subsurface permafrost ice, e.g. Arabia Terra with 16 % by mass of water, as

shown by *Mitrofanov et al.* [2004].

Today, Mars does not have a noteworthy planet-wide, intrinsic magnetic field that could shield the planet from the Solar wind or GCRs. However, the MGS mission discovered regions on Mars with strong, remnant crustal magnetic fields. In the Martian highlands, the crust shows a magnetisation that is one order of magnitude higher than in the terrestrial crust. These crustal remnants can create local magnetic fields, reaching up several hundreds of km and, thereby, providing protection from charged particles from the outer space via highly-localised magnetic umbrellas ([*Connerney et al.*, 1999], [*Acuña et al.*, 2001]).

3.2. Early Mars

In this section the Martian planetary evolution is retraced to the Noachian epoch. It is explained how early Mars most likely would have differed from the present, as well as based on what evidence/theories such conclusions are drawn. Furthermore, the Noachian Mars conditions are brought into context with the overlying topic of this work – Could life have emerged on Mars? – and why, especially, the Noachian epoch is a prime candidate for this possible emergence.

As established above, in present times the surficial and atmospheric conditions on Mars do not seem to be well-suited for the presence of life. The Martian surface is, for most parts, a dry and barren desert, albeit larger volumes of water can be found as ice beneath the surface and in the polar caps. The thin atmosphere and lack of a global magnetic field do not provide ample protection from energetic particles bombarding the atmosphere from outer space.

However, there is substantial evidence that Mars, in the past, possessed an environment much more convenient for an emergence of life. It is widely accepted that the early-Mars climate was warmer and wetter than today, and that the planet still possessed a global magnetic field, as well as a much denser atmosphere. Before the environmental changes are described in more detail, first, a short explanation of the terminology used in reference to the Martian historic timeline is given for a better understanding.

The planetary history of Mars is, generally, divided into three periods, based on certain geological features. Especially the differing crater densities in different regions are a convenient tool for linking a region to a certain time period, as, in general, the occurrence rate of impacts decreased from the time of the Late Heavy Bombardment (LHB), roughly 4 billions years ago, to the presence. The different eras are named after locations of Mars belonging to that respective time period [*Barlow*, 2008]:

- the Noachian epoch ($\sim$ 4.1 – 3.7 Ga ago), named after Noachias Terra, a heavily cratered region in the Southern highlands

  Formation of the oldest remaining surface areas. Noachian regions show high crater density due to impact during the LHB. More detail about this period can be found further down.

- the Hesperian epoch (3.7 – 3.0 Ga ago), named after Hesperia Planum, also situated in the Southern highlands

  Marked by the cessation of impacts from the LHB, high volcanic activity and subsequent creation of extensive lava plains.

- the Amazonian epoch (3.0 Ga ago – present), named after Amazonis Planitia, a smooth plain in the Vallis Marineris region

  Characterised by low meteoric impact density and localised volcanic activity.

For more detailed information on the geologic history of Mars, the reading of [*Carr and Head*, 2010] is recommended.

The current understanding is, that a planet's ability to have developed and/or sustained any kind of life, the so-called planetary habitability, depends on the sustained existence of liquid water on the planet. This approach stems from the fact that liquid water is regarded as the key component for all terrestrial life forms [*Chyba and Hand*, 2005]. Therefore, the search for life on Mars is strongly connected to the search for water, as expressed in the astrobiological National Aeronautics and Space Administration (NASA) motto *"Follow the water"*.

Now, as mentioned before, there are several indications that Mars once possessed large amounts of liquid surface water. In regions, whose formation is dated back to the Noachian, one can find large amounts of valley networks and outflow channels that are assumed to have been formed by fluvial movements of liquid water. Furthermore, the impact craters show signs of high erosion rates, again supposedly due to fluvial movements of water. The highly-distributed existence of phyllosilicates, created under the presence of water, is another strong indicator for the presence of liquid water in the Noachian ([*Carr and Head*, 2010], and references therein). *Fassett and Head* [2008] further suggest the presence of numerous lakes in the highlands during the Noachian period.

To sustain liquid water on long enough time scales, Noachian Mars must have had considerably different atmospheric conditions than today, as average surface pressure ($\sim$ 6 mbar) and temperature ($\sim$ 218 K) are too low for a prolonged existence of liquid water. Furthermore, the early Sun only had a luminosity of 25 – 30 % compared to present times. Model calculations for photochemically stable atmospheres yield that

at least 0.6 bar of CO_2 are needed to raise the Martian surface temperature above 273 K ([*Kahn*, 1985] and references therein), while other findings suggest necessary surface pressures between 1 – 5 bar ([*Lammer et al.*, 2002] and references therein).

The fact that the MGS mission found crustal magnetic field remnants in the early-Noachian-dated Martian highlands, but not to such an extent in younger terrains, indicates that during the early Noachian Mars still possessed a global, magnetic field, which then disappeared still in the Noachian due to the cessation of the Martian dynamo [*Acuña et al.*, 1999]. For one, such a planetary magnetic field is important as it serves as a shield against Solar wind erosion of the atmosphere, thereby being one of the reasons early Mars could have had a denser atmosphere [*Lammer et al.*, 2002]. Second, the magnetic field not only shields the planet from Solar particles, but also to a lesser degree from the higher-energetic GCRs. It is, however, not assured that the latter shielding effect would have had a significant influence on the GCR-induced surface environment if the atmosphere was dense enough [*Grießmeier et al.*, 2005]. E.g, *Molina-Cuberos et al.* [2001] showed that surface particle fluxes at a 1 bar atmospheric surface pressure do not change significantly by adding an intrinsic magnetic field with a magnetic moment comparable to Earth.

All these factors – together with the fact that the Noachian epoch correlates with the estimated time of an origin of life on Earth ($\sim$ 3.7 Ga years ago) – make the Noachian Mars a well-suited candidate for a possible emergence and sustainment of life. The right image of Fig. 3.3 hints at how an ancient Mars might have looked like.

To conclude this chapter insight, on why conditions on Noachian and present-day Mars differ that greatly from each other (i.e. loss of the global magnetic field, considerably thinner atmosphere), is given.

Measurements of the crustal magnetisation show that inside impact basins created in the late Noachian period, such as Hellas Planitia, there is a distinct lack of magnetisation, most probably due to demagnetisation during the impact. This, in turn, suggests that during that time the magnetic dynamo was already turned off, as otherwise the basins would have been remagnetised. Why and how the dynamo ceased to exist is still not entirely clear. The current theory is that the vigour of core convection decreased to levels too low to sustain a magnetic field, due to cessation of Martian plate tectonics [*Arkani-Hamed*, 2004] or giant meteoric impacts in the mid-Noachian [*Roberts et al.*, 2009]. Either way, the loss of the magnetic field subsequently played a major role in the loss of the denser, Noachian atmosphere.

It is assumed that the postulated dense atmosphere was already lost at the end of the Noachian period [*Barlow*, 2008]. However, similar to the uncertainties about the exact cessation mechanisms of the Martian dynamo, how the atmosphere thinned out is not totally established. The assumption is that three main processes were involved,

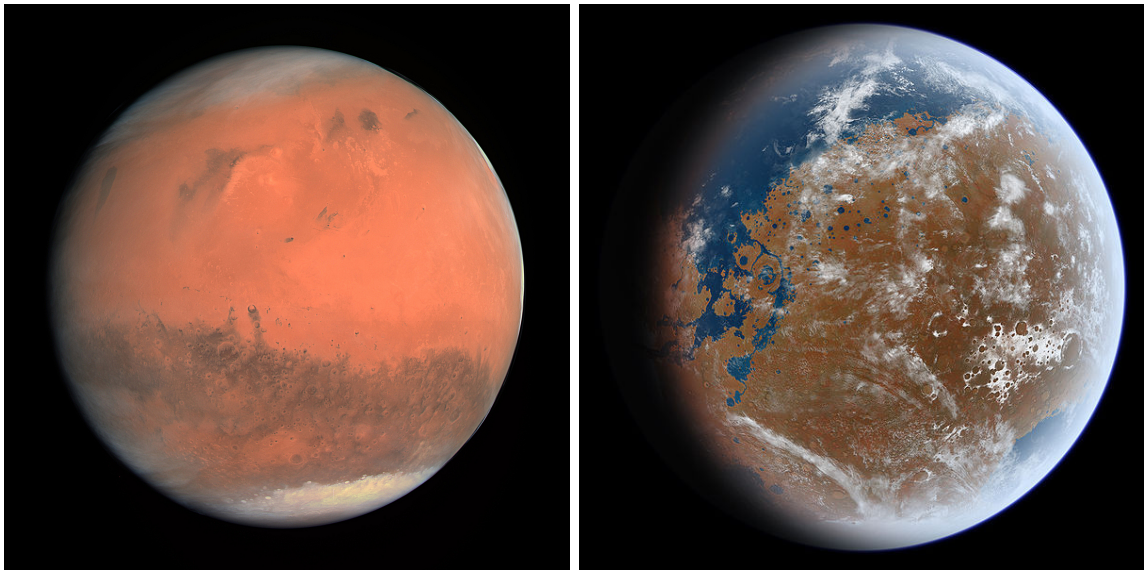

Figure 3.3.: Present-day and early Mars. Left: True colour image of Mars, as seen by OSIRIS during the Rosetta flyby in 2007. The reddish hue of Mars, caused by iron oxides in the regolith and dust, can be nicely seen, as well as variations in the colour due to variations in composition and grain sizes of the soil. At the poles Mars is covered by caps of dry ice and water ice. From: `http://rosetta.jpl.nasa.gov/dsp_images_mars.cfm`. Right: Artist's impression of what early Mars might have looked like. Note that this is not strictly a conception of Noachian Mars, as some later, Hesperian features are also incorporated in this image. From `http://ittiz.deviantart.com/art/`.

besides the thermal Jeans escape of lighter atoms [*Brain and Jakosky*, 1998]:

- Solar wind erosion,
- impact erosion,
- sequestration into regolith and polar caps.

After the loss of its magnetic field, Mars was not any longer protected from Solar wind impact. Without such a shield, Solar wind particles can impact the atmosphere unimpeded. Due to this, two processes of atmospheric escape happen [*Chassefière and Leblanc*, 2004]. For one, atmospheric ions, produced by UV ionisation or direct ionisation by Solar wind particles, can be swept away by the magnetic field of the Solar wind. Second, the atmospheric ions are accelerated by the magnetic field of the Solar wind and can then, subsequently, ionise further atmospheric neutrals and eject them into outer space.

Impact erosion refers to atmospheric escape processes induced by large impactors that hit Mars as part of the LHB. As the impactors propagate through the atmosphere, they can heat the atmospheric gas, leading to the molecules being able to reach escape velocity. Furthermore, given a large enough impactor, the expanding vapour cloud of the impact can also drag significant amounts of atmosphere away from the planet [*Melosh and Vickery*, 1989]. Due to Mars' relatively low escape velocity, impact erosion possibly had a significantly larger effect on Mars than on Earth.

Brain and Jakosky [1998] calculated that the first two processes could have removed 95 – 99 % of the initial atmosphere. A part of the atmosphere is also lost due to sequestration in the regolith or the ice caps. As the major part of the atmosphere was removed due to the above processes, the amount of CO_2 necessary to be sequestered in this scenario lies in realistic orders of magnitude.

4. Model for Dose Rate Calculations

This chapter describes the model, developed for this work, to calculate the radiation exposure on the Martian surface due to interactions with GCRs. As the model makes use of the Monte-Carlo (MC)-based toolkit `GEANT4`, first a brief description of this tool and the MC method is given. Next follows a more detailed description of the `GEANT4` application `PLANETOCOSMICS`. This application was developed to particularly calculate interactions of GCRs with magnetic fields, atmospheres and soils of the planets Earth, Mars, and Mercury. To better understand how `PLANETOCOSMICS` can be used in the scope of this work, it is explained how the present-day environment of Mars is modelled. Of course, not only the current situation on Mars is of interest for this research. Therefore, a description of the implementation of the parametric changes analysed in this work, to estimate Noachian conditions, is given. Subsequently, the modelling process is described step-by-step, i.e. how the dose rates are determined from an initial calculation of Martian particle fluxes.

To give a brief overview of the modelling process: With the help of `PLANETOCOSMICS` particle fluxes of all considered species are calculated for the altitude of interest, e.g. the Martian surface under present-day atmospheric conditions. Then, the effects of this resulting radiation field are determined, in terms of what amount of dose they would induce. For this, the derived particle spectra are taken as input and shot-in on a `GEANT4`-modelled detector, consisting of a globe of water. This globe has a chosen volume of 1 l to allow for an easy conversion of the energy deposited by the particle spectrum into the dosimetric unit Gy.

4.1. GEANT4

Geometry and Tracking (GEANT) 4 [*Agostinelli et al.*, 2003] is a toolkit to simulate particle propagation through matter. To track such a particle, interacting with matter, `GEANT4` makes use of the so-called MC method, which is explained below in Ch. 4.1.1. The code provides a wide range of input particles, such as heavy charged particles or neutrons. `GEANT4` allows for a detailed construction of the detector geometry to track a particle's movement through it, with the possibility of visualisation of detectors and particle tracks. Here, detector can refer to any volume of constructable matter,

e.g. a silicon detector commonly used in radiation measurements. The particle-matter interactions on the path are calculated dependent on the implemented, changeable physical processes (for an example of processes that can be included, see Ch. 2.2.1). Aside from the tracking of the incident particle's movement, GEANT4 also calculates energy deposits of the particle in matter.

A typical tracking output for an interaction of a particle with a detector could contain information like the incident particle's initial energy and direction, the energy deposited in the volume, and the particle's direction after leaving the volume. Its properties make GEANT4 an extremely helpful tool in the field of particle measurements, as expected detector responses can be simulated before the instrument is used for actual measurements.

4.1.1. Monte-Carlo method

A Monte-Carlo (MC)-method, in general, is based on repeated random drawing of numbers from a given input class. A classical example of the MC technique is the determination of the number π. Here, one takes a square with the side lengths 1, and draws a quarter circle with the centre in one corner of the square. Now, coordinates p_x, p_y for a point inside the square are randomly determined, with the condition that $p_x \in \{0,...,1\}$ and $p_y \in \{0,...,1\}$. This process then is repeated multiple times. If one counts the number of points placed inside the quarter circle, and builds the ratio with the total number of drawn points, this value approaches $\frac{\pi}{4}$, the ratio between the areas in and out of the quarter circle.

In the following, a short description of the MC method used by GEANT4 will be given. For a more detailed look on MC methods, refer to [*James*, 1980].

In principle, the GEANT4-MC process works the same way as described in the example above. The occurrence probabilities of nearly all particle-matter interactions depend on the cross section of that interaction for the given particle and matter. In general, a given particle and matter can undergo several types of interactions with unique cross sections for each process. Therefore, GEANT4 first has to define which of these possible interactions happen. For this, for each interaction the distribution function of the interaction probability per path is calculated per numerical integration. Based on these functions, GEANT4 creates a randomly-drawn, proposed step length for each interaction. The interaction with the smallest step is then taken and the particle is stepped through its new position in the matter.

After, the interaction is determined, changes to initial values, such as energy and the direction vector, of the incident particle and the interacting matter, and possible, resulting secondary particles are calculated. Again, via random sampling for the

differential cross sections of the involved particles' parameters.

The above described process is then repeated for the next interactions with the target, until the particle leaves the defined volume or its energy decreases below a certain threshold, e.g. 0 eV. Possibly created secondaries are also independently propagated through the matter in the same way.

4.2. PLANETOCOSMICS

PLANETOCOSMICS [*Desorgher et al.*, 2006] was developed as an application for GEANT4. In general, it uses the same underlying code, e.g. for interactions of particle and matter or particle tracking. However, it was especially designed to calculate particle propagation in magnetospheres and atmospheres of planets. The advantage of PLANETOCOSMICS for the user is that several important features necessary to simulate such particle interactions with magnetospheres and atmospheres are already pre-defined in the code. The so-called physics list, containing the considered physical processes, includes all relevant interactions and is automatically initialised. In the basic GEANT4, the user has to model the geometry of all interacting matter volumes himself, whereas in PLANETOCOSMICS the planetary atmosphere and the top layers of the surface are also already incorporated as "interaction targets". E.g., the atmosphere is modelled in several layers of equal atmospheric depth and with the corresponding mean atmospheric composition and density of the layer's altitude.

PLANETOCOSMICS provides further features, not per se provided by GEANT4, and is set up in a way that the user only needs to set flags to use these features. For this, the PLANETOCOSMICS code accepts input parameters defined by the user, in the form of so-called "macro"-files. These files mainly contain sets of user-selected, code-compliant input commands.

For example, PLANETOCOSMICS provides various predefined selections of incident particle sources, such as mono-energetic proton beams or beams that are shot-in monodirectionally. A helpful feature here is, in particular, the provision of primary galactic-cosmic-particle spectra, which will be explained in the following:

To simulate the incident radiation of GCRs, PLANETOCOSMICS provides predefined particle spectra for protons and alpha particles, with an isotropically-distributed incident direction. The energy distribution for these spectra is modelled based on the work of *Gleeson and Axford* [1968] and *Garcia-Munoz et al.* [1975], with flux values corresponding to 1 AU distance from the Sun. Note that Mars orbits the Sun at ~ 1.5 AU. However, according to *Webber* [1987], one should only expect small changes in the fluxes from 1 AU to Mars. Therefore, in this work, the PLANETOCOSMICS-provided GCR-fluxes were used without further adjustments for the farther distance of Mars. This is

an approach also used by other analyses, e.g. [*Gurtner et al.*, 2005]. PLANETOCOSMICS lets the user choose between GCR models for Solar minimum, mean, and maximum activity. As the GCR flux is highest during Solar minimum, this work confines itself to research for this condition.

Due to the setup of the GCR-flux-selection command, it is, in general, also possible to simulate other particle species, instead of protons and alphas. However, one problem posed here is that High Charge and Energy (HZE) ions can not simply be substituted, due to the way PLANETOCOSMICS handles ions as input particles. Now, one has to be aware that the contribution of HZE ions to the dose is not negligible, despite their comparably low fluxes [*Dartnell et al.*, 2007A]. So, simply disregarding the HZE-GCR flux is not a desirable approach. Therefore, in App. A.4 a way of estimating this contribution with the presented model is introduced.

Compared to the GEANT4 run output, the data output provided by PLANETOCOSMICS is also customised. Before starting a simulation, the user can define which atmospheric altitudes (or soil depth) should be read out by the code. The data output then provides a set of output parameters, as defined by the user. The interesting read-outs for this work are mainly histograms of the downward- and upward-directed particle fluxes at certain altitudes, e.g. at the surface. Downward- or upward-directed, here, refers to particles coming from the upper or lower half space with respect to the altitude.

These histograms contain a user-defined binning (linear or logarithmic), where minimum and maximum energy, as well as the number of bins can be chosen. As the process of deriving the flux values for each bin is basically a scaling of the number of counted particles in a respective energy bin with the determined incident particle flux at the top of the atmosphere, PLANETOCOSMICS further gives a poisson-distributed error (also scaled with the incident flux) for each bin. Which particle species are tracked also has to be set by the user. Other output parameters include, e.g., histograms of azimuthal or zenithal angular distributions. For a complete overview of all available commands, refer to [*Desorgher et al.*, 2006].

4.2.1. Implementation of Martian features

In the following, a description of how, in particular, Mars and its atmosphere are modelled is given. Note that, here, the modelling of the Martian crustal magnetic fields is left out, as it is not considered in the presented dose calculation model. As the occurrence of the crustal fields are localised phenomena, i.e. not uniformally distributed over the whole surface, and this research aims at making generally valid estimations about the radiation exposure, this omission is deemed justifiable.

Present-day features

The model of Mars consists of three components: planetary core, soil, and atmosphere. The core is modelled as a sphere with a radius of the mean radius of the planet minus the depth of the soil. Furthermore, the core is modelled to absorb all incoming particles, i.e. no interactions occur beneath the soil and particles can not penetrate the planet.

The soil, situated atop of the core, is per default modelled as a 10 m layer of material with 1.7 $\frac{\mathrm{g}}{\mathrm{cm}^3}$ density. The default composition is according to the Pathfinder measurements (see Table 3.1 for abundances). This composition reflects a "dry" Mars. However, in Ch. 3.1 it was established that Mars contains larger amounts of water ice in the polar caps and as subsurface permafrost in the upper-latitude regions (and occasionally even at lower latitudes), which is supposed to yield changes in the resulting radiation exposure [*Dartnell et al.*, 2007A], as the neutron surface flux contains a significant amount of backscattered neutrons from the soil [*Clowdsley et al.*, 2001]. These water-ice-containing conditions are, therefore, in this work accounted for in separate simulations and are presented alongside simulation results for a "dry" Mars.

As mentioned above, the modelled atmosphere is divided into layers of equal depth. The composition and density of each layer are calculated from an atmospheric table file, fed to the code. For this research, a homogeneous composition ratio, as given in Ch. 3.1, is considered. Densities and pressures for different atmospheric and surface altitudes were extrapolated from atmospheric pressure measurements, available in the `PLANETOCOSMICS` installation package.

Adaptation of Planetocosmics for the research in this work

After having introduced how the present-day Mars is modelled in `PLANETOCOSMICS`, here, an overview of the changes undertaken to adjust said modelling for the purposes of this work is presented.

As explained in Ch. 3, compared to present-day conditions the Noachian Mars presents itself as a much-more suited candidate for a possible emergence of life. Therefore, a modelling of Noachian conditions and the resulting radiation environment is of high interest. Now, to model an all-encompassing representation of early Mars is not quite feasible. Researchers do have a good idea, how the Noachian could have looked like, but exact conditions are rather unknown. E.g., it is assumed to be certain that early Mars had a much denser atmosphere, and extensive modelling has been conducted to calculate this atmosphere. However, even generally accepted findings differ about one order of magnitude (see Ch. 3.2).

One possible approach is, thus, not to model "hard" values, but to look at trends brought about by approximating possible Noachian values, which is what is done in this

work. E.g., increasing the atmospheric pressure (and hence the density) stepwise to orders of magnitude possible in the Noachian, should give indications of how the resulting radiation environment would have differed from today. Changing the atmospheric pressure level in `PLANETOCOSMICS` is a rather straightforward procedure and is done, by simply adjusting the pressure values provided in the atmospheric table. To have a reasonable progression from current-day to early-Mars pressures, for this research the pressure level was raised in three steps (by factors of 25, 50, and 100), with the largest increase placing the mean surface pressure (~ 0.6 bar) in the order of magnitude suggested by the mentioned simulations.

Proposed liquid surface water in the Noachian can also be accounted for by changing the modelling of the soil. Instead of just modelling the default layer of soil at the bottom of the atmosphere, for this analysis, first a "soil" layer consisting of liquid water was created, which was then followed by a layer of normal, dry soil. To simulate different amounts of water, several different simulations were conducted with layers of 1 m, 10 m (e.g. a river), and 200 m water (e.g. a larger lake or sea).

Subsurface permafrost water ice was modelled in a similar way, by changing the default soil into small alternating layers of water ice and dry regolith. Determining this mixing ratio and the depth of the permafrost layer was done in accordance with research from *Mitrofanov et al.* [2004].

A possible, functioning global magnetic field was not yet considered in this model. Again, due to uncertainties in possible field strengths, incorporating fields with different strengths (to estimate trending tendencies) adds another dimension to the existing parameter space. As the magnitude of the effect of a global magnetic field on the resulting surface radiation exposure for dense atmospheres is, at least, debatable [*Grießmeier et al.*, 2005], [*Molina-Cuberos et al.*, 2001], this Noachian "feature" was left out of this research. However, `PLANETOCOSMICS` allows for custom-built magnetic fields to be added into its modelling, so that a future research on this topic is possible.

One further circumstance that is not considered in this research at the moment, is the temporal evolution of the GCR flux. E.g. as cosmic ray sources are not uniformally distributed throughout our galaxy, the Solar system's relative positioning in the galaxy could have an influence on the GCR flux [*Shaviv and Veizer*, 2003]. For more insight on this topic, a reading of [*Scherer et al.*, 2006] is recommended. As the exact nature of these changes is not ascertained at the moment, the present-day GCR flux was assumed for this work.

However, all the above mentioned left-out features can be incorporated in future research. Here lies a great advantage of the developed model. Due to the high adaptability of `PLANETOCOSMICS` and the way the output is processed by the model, a wide range of changes to the Martian radiation environment can be implemented. E.g., in-

put spectra can range from different GCR fluxes at Solar maximum or minimum or intermediate activity, to the simulation of SEP spectra.

The flexibility of the model code also allows to calculate resulting dose rates not just subdivided into contributions by different particle species (as presented in this work). For example, calculated contributions of particles coming from the upper/lower hemisphere, or particles of a certain energy range are also a possibility.

4.3. Processing steps

In this section the model used in this work, to derive the dose rate values presented in Ch. 5, is described step-by-step. In general, calculating the dose rates for each respective subset of results, e.g. as shown in Chs. 5.1.1, 5.1.2, 5.2, or 5.3, can be broken down into the following steps:

1. Determine the surface (or subsurface) fluxes for different particle species with the help of `PLANETOCOSMICS` simulations for the respective environmental conditions.
2. Convert these in spectra to be used with the `GEANT4` modelling of a detector consisting of a globe of water.
3. Simulate interactions with the detector for incident particles.
4. Derive necessary parameters for dose calculation from the simulation results.
5. Calculate absorbed dose or dose equivalent rates from these data.
6. Reiterate steps 1 to 5 several times. Calculate the final dose rate from the data of all iterations.

To get a better idea of the processing, Fig. 4.1 shows a flow diagram of these processing steps (with the step numbers referring to the numeration as described above). The steps are now described in more detail:

1. For all dose calculations, the first step is always to develop the necessary control files, or macro-files, to run the `PLANETOCOSMICS` simulations. As mentioned in Sec. 4.2, these macros contain information on which particle species should be tracked, and in what altitudes (or soil depth) these particles should be counted. Furthermore, the atmospheric model, in terms of pressure or density and composition, is fed into this macro. After having decided, how the Martian environment should be modelled, and the corresponding control files are arranged, simulations are conducted. The output of these simulations, created by `PLANETOCOSMICS`, is then processed with an analysis code, developed for this work, to derive omnidirectional particle fluxes for each particle

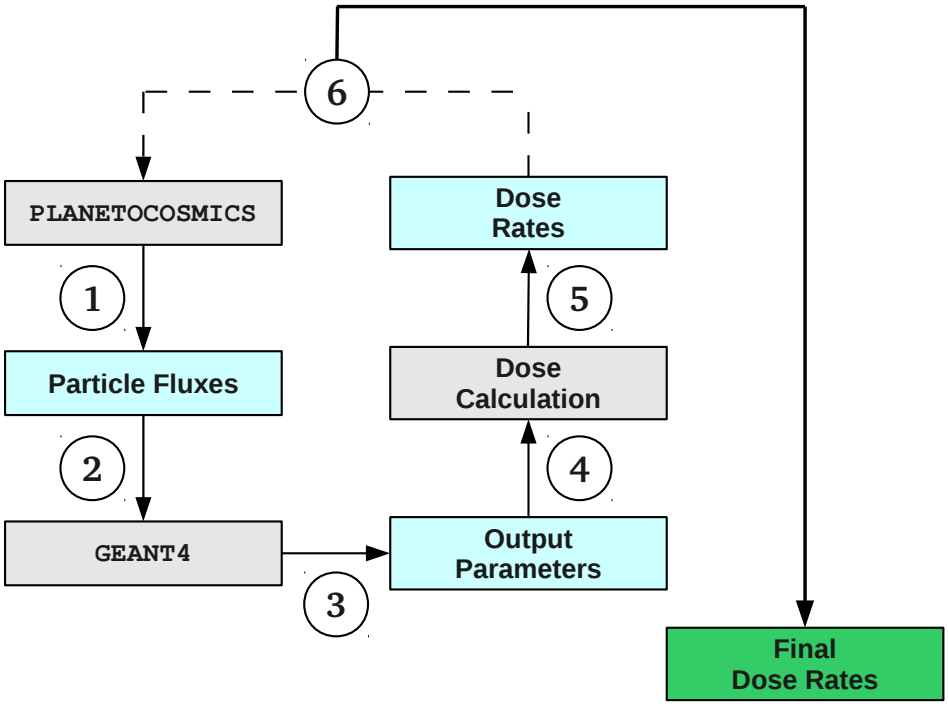

Figure 4.1.: Flowchart of the processing steps for the dose-rate model. The numbers refer to the numeration in the text. Thin black arrows indicate the processing flow. The dashed arrow denotes that the sequence is started over after dose rates for one sequence are calculated. The thick black arrow indicates the final step of the processing, the calculation of the final dose rates averaged over all cycles.

species to be considered at the wanted altitude or depth. As mentioned above, the fluxes and their respective poisson-distributed errors are derived for each logarithmic bin in the pre-defined energy range.

In this model, for each environmental condition to be analysed, e.g. the influence of higher atmospheric pressure, several `PLANETOCOSMICS` simulations were set up with different surface altitudes, ranging from -10 km to +10 km (with respect to the Martian reference surface at 0 km). Although on Mars there are several mountains known to be higher than the +10 km chosen here (e.g. Olympus Mons, Elysium Mons), this upper value is deemed high enough for the purposes of analysing changes in the surface doses with differing elevations. Furthermore, if not described otherwise in the appropriate section, the other input parameters for the Mars model of `PLANETOCOSMICS` (e.g. density and composition of atmosphere and soil, and primary GCR fluxes) were chosen as described in Sec. 4.2.1. The tracked particle species for all runs are protons, alphas, gammas, neutrons, electrons, positrons, muons, and antimuons.

The derived fluxes from each simulation are carried over to the next steps, allowing for subsequent dose calculations for different surface altitudes in the environment.

2. To use the information gathered in step 1 for simulations with the `GEANT4` toolkit, as a next step a further set of control macros has to be developed. The derived files containing the flux values are processed into an appropriate tabular form to be used with `GEANT4` (these macros, of course, contain further specific control commands for the following simulation). To be more precise, for this not the pure simulated flux value Φ of a certain bin is taken, but rather a randomly poisson-distributed noise is added to the respective Φ by taking into account the corresponding $\Delta\Phi$, to incorporate the uncertainties in the "measured" (or better, simulated) flux spectrum.

3. `GEANT4` then simulates the interactions of incident particles with the water detector. Incident particles are randomly drawn, according to the spectral distributions given in the macros.

4. The stored output of the simulations provides certain sets of information, such as the particle species, the particle's initial energy, its energy deposit in the water globe, its directional vector, and so on, for each incident particle. The data from these simulations is, then, processed further with another analysis code.

5. Here, dose values are calculated for each incident event. The absorbed dose in water D_i of any event i is calculated by:

$$D_i = \frac{E_{Dep,i}}{e} \cdot m_{Det}, \tag{4.1}$$

where $E_{Dep,i}$ is the deposited energy in eV by this event, e the elementary charge, and m_{Det} the mass of the water detector (1 kg). The absorbed dose rate $D_{R,i}$ can then be calculated by:

$$D_{R,i} = D_i \cdot A_{Det} \cdot n_j, \tag{4.2}$$

with D_i being the absorbed dose as calculated with Eq. 4.1, A_{Det} the surface area of the detector, and n_j the scaled number of particles per cm^2 per s this incident particle corresponds to, as determined by the `PLANETOCOSMICS` simulations in step 1. After calculating dose rates for each particle, the analysis code processes the data to arrange into different data sets, e.g. containing total and particle-type-specific absorbed dose rates for each considered elevation.

With the model developed in this work, it is also possible to calculate the dose equivalent rate H of each incident event, by multiplying the absorbed dose rate with the respective quality factor Q, where the respective Q is dependent on the particle species and its specific energy loss $\frac{\mathrm{dE}}{\mathrm{dx}}$, as described in Ch. 2.2.3. For the calculation of the energy loss the track length of the incident particle in the water globe is taken into account.

6. To estimate the errors in the dose rate calculations with this model, a bootstrap MC method is applied. As mentioned under 2., the `GEANT4` input spectrum is taken as a poisson-noise-distributed spectrum of the `PLANETOCOSMICS` simulation results. To estimate the variation of calculated dose rates, steps 1 to 5 are, therefore repeated with another set of randomly determined, noisy fluxes. This cycle is reiterated several times with the calculated dose rates of each repetition being stored. The final dose rate, as used for the analysis of the results in Ch. 5, is calculated as the arithmetic mean $\bar{D}_R$ of the dose rate $D_{R,n'}$ of each iteration n', and the resulting error as the standard deviation σ.

5. Modelling the Noachian Radiation Environment

This chapter will give an overview of the results from the simulation work as described in Ch. 4.3. In the scope of this work, three influencing factors on the Martian radiation environment were analysed, and how changes in these parameters affect the resulting radiation exposure:

- an increase of the atmospheric pressure level,
- the depth beneath the surface soil,
- the existence of liquid surface water or sub-surface water-ice.

From these the first point will be analysed in the most detail, as the pressure conditions build the focus point of this research. However, for a more complete overview of the possible situation research on the latter two factors will also be presented, albeit in a more condensed scope.

5.1. Influence of atmospheric pressure

To analyse the influence of possible higher atmospheric pressure conditions on the Martian surface radiation, it is first necessary to simulate the Martian radiation environment under present-day conditions. Going from this benchmark further simulations with changed conditions can then be derived.

As mentioned before, one of the main goals of this work is to analyse the influence of changes in the atmospheric conditions for a broad set of parameters, e.g. the resulting total dose rate for different surface altitudes, or dose rates of different particle species contributing to the radiation field, along with providing surface fluxes for each particle species. This broadening of the parameter space can be helpful for researchers dealing with the topic of radiation on Mars (present-day or ancient), as to date there is only research on certain subsets of the here presented parameter space available. Nonetheless, these existing researches may aid in evaluating the model presented in this work by comparing results derived with this model to other findings.

The following section, thus, presents results for present-day Martian conditions and an evaluation of these results is conducted with findings from the existing research. In Sec. 5.1.2, the model is applied to different atmospheric pressure conditions, i.e. increase factors of 25, 50, and 100, and results from simulations for these scenarios are presented. Subsequently, a conclusion on the influence of atmospheric pressure on the dose is drawn.

As stated in Ch. 4.2, the model currently takes GCR-protons and alpha-particles into account, as heavier-ion input spectra are, at the moment, not implemented in `PLANETOCOSMICS`. The approach to give an estimate on how HZE ions would affect the presented dose values, is introduced in App. A.4.

5.1.1. Present-day radiation environment

As described in Ch. 3, today Mars has a very thin atmosphere which allows primary galactic particles to propagate deep into the atmosphere and even into the soil. Fig. 5.1 shows `PLANETOCOSMICS` simulation results for monoenergetic primary protons (of different energies) under present-day Martian conditions. By shooting different monoen-

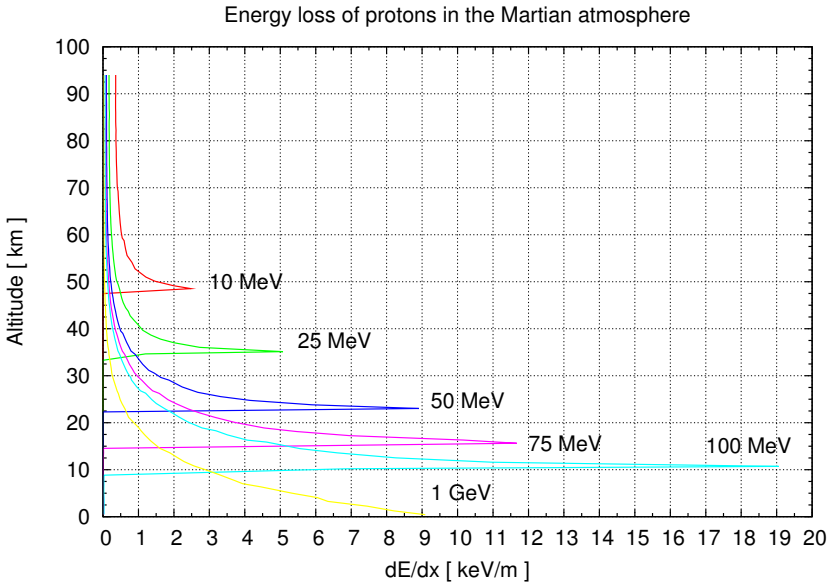

Figure 5.1.: Specific energy loss of primary galactic protons in the Martian atmosphere. Results from `PLANETOCOSMICS` simulations, where pencil beams of monoenergetic protons were shot-in at the top of the atmosphere with straight-downward direction. The given atmospheric altitudes refer to the datum altitude of 0 km.

ergetic proton beams into the atmosphere, with straight-downward direction, insight on the penetration depth into the atmosphere of said protons can be derived. In the

plot, one can see that the higher their initial energy the deeper these primaries traverse through the Martian atmosphere. For the simulated energies, protons with energies of 100 MeV and lower do not reach the surface. This energy threshold, of course, varies with the surface altitude, as different altitudes have different atmospheric depths.

Aside from directly adding to the surface radiation field, the primary particles can create a large amount of secondary particles in the atmosphere and soil, which in turn can also contribute to said radiation field (see Ch. 2.1.1). The resulting surface radiation environment induced by GCR-protons and -alpha particles for Solar minimum conditions, as simulated with `PLANETOCOSMICS`, can be seen in the top panel of Fig. 5.2 for an example of the 0 km reference surface altitude. It is interesting to see that at energies higher than $\sim$ 250 MeV the radiation field is dominated by charged particles, mainly protons (plotted in red), whereas for lower energies neutral particles, i.e. neutrons (green) and gammas (blue),make up most of the radiation field. All said, the plot gives a good indication of the diversity of the present-day Martian radiation environment, i.e. several different particle species have a significant influence.

Based on these particle fluxes, the lower panel of Fig. 5.2 shows the resulting total absorbed dose rate at the Martian surface, as well as the contributions of selected particle types, in dependence of the surface altitude. Note that, for the sake of clarity, some particle species (i.e. gammas, electrons, and positrons) are not shown here, but can rather be found in App. A.1. The analysed elevations correspond to surface pressures ranging from $\sim$ 2 to 16 mbar, with around 6 mbar at datum altitude. The total absorbed dose rate (plotted in black), including all simulated particle species (even if they are not shown in the plot), is found to have values between 0.16 and 0.175 Gy/a. No strong dependence on the surface altitude is detectable, if at all there is a slight trend that higher elevations show higher dose rates.

A stronger correlation is found for protons and alpha particles (magenta). The proton contribution to the total absorbed dose decreases from $\sim$ 0.1 to 0.075 Gy/a with lower ground-levels, while the slope for the alpha contribution is even more pronounced, decreasing from 0.024 (at +10 km) to 0.01 Gy/a (at -10 km surface altitude). This effect can be explained rather straight-forward and is illustrated in the left panel of Fig. 5.3. The main part of the proton and alpha spectra (and subsequent dose rate contributions) are made up of primary GCRs, i.e. particles coming from the upper hemisphere. As mentioned, the higher-energetic particles can easily propagate all the way to the soil, even for low surface altitudes. However, as one can see in the plot, due to the additional atmosphere, through which particles arriving at low surface altitudes have to travel, these particles lose more energy the deeper they propagate, resulting in comparably lower surface fluxes (and thus resulting in lower dose rates). As one can further see, the difference in the surface fluxes is more pronounced for alpha particles, and therefore the

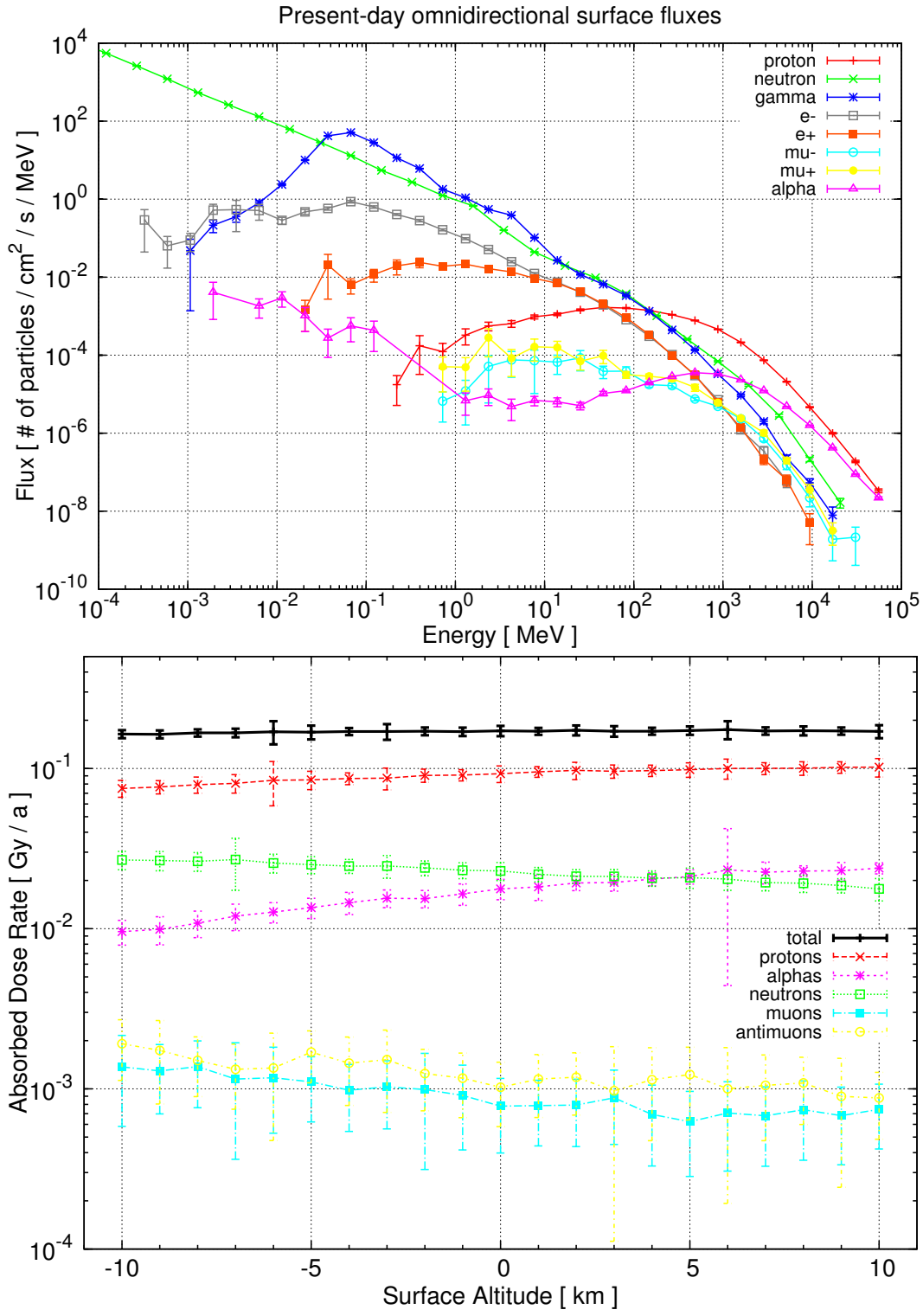

Figure 5.2.: Top: Exemplary omnidirectional particle fluxes at the Martian surface at datum altitude. Simulated with PLANETOCOSMICS for Solar minimum conditions, considering GCR-protons and -alpha particles. Bottom: Resulting absorbed dose rate contributions of selected particle types for present-day atmospheric conditions in dependence of the surface altitude.

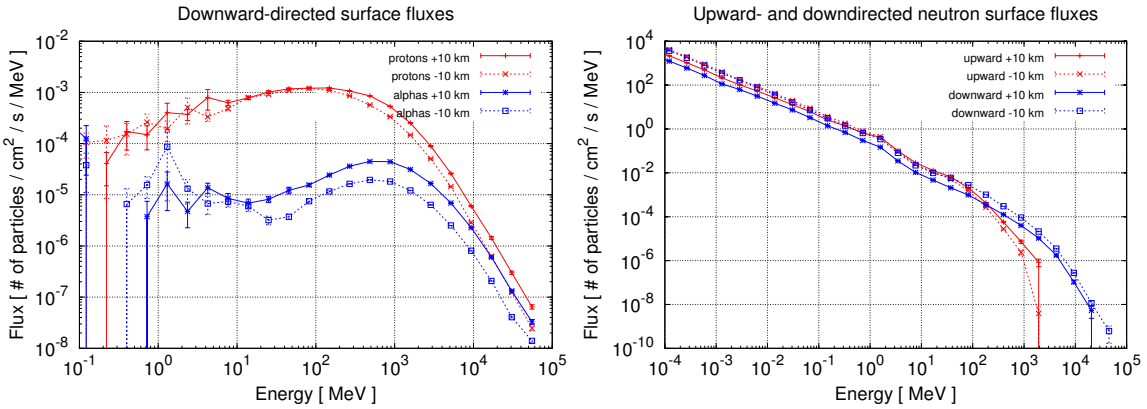

Figure 5.3.: Martian surface fluxes for present-day conditions, calculated with PLANETOCOSMICS. Left: Downward-directed proton (red) and alpha particle (blue) fluxes for surface altitudes of +10 km (solid) and -10 km (dashed). Right: Downward- (blue) and upward-directed (red) neutron surface fluxes for surface altitudes of +10 km (solid) and -10 km (dashed).

decrease of the dose rate with lower surface altitudes is steeper compared to protons. This is due to the fact that the energy loss of a particle is proportional to the square of its charge, or $\frac{dE}{dx} \sim Z^2$ (see Eq. 2.1).

Analysing the neutron dose rates (shown in green in Fig. 5.2), one can find a slight increase in dose with decreasing ground-level elevation, contrary to protons or alpha particles. At +10 km surface, we find an absorbed dose rate of 0.018 Gy/a, which increases to 0.027 Gy/a at -10 km surface altitude. This anti-correlation to the elevation can be explained when analysing the neutron surface fluxes of high and low altitudes. The right panel of Fig. 5.3 shows these fluxes divided into downward- and upward-directed components. As can be seen, the deviation between upward-directed fluxes, i.e. neutrons produced in the soil, between +10 (solid red line) and -10 km (dashed red) is rather small, meaning the backscattered component of neutrons is more or less equal for different elevations. The fluxes of downward-directed neutrons show a more pronounced difference. Over the whole shown energy range the flux at -10 km surface altitude (solid blue) is higher. This is due to the fact that the neutron production rate in the additional atmospheric layers over deep-situated elevations outweighs the slightly decreasing primary particle flux.

The gamma, electron, and positron contributions to the dose rate show the same (at different absolute dose values) characteristics as the one for neutrons. Therefore, a brief discussion of these species is placed in App. A.1, where the corresponding plots are found.

The antimuon and muon contributions (plotted in yellow, resp. light-blue in Fig. 5.2), as should be expected, show very similar characteristics to each other, with the antimuon contribution being a bit higher. Interestingly, they show an even more pronounced increase in dose rates with decreasing elevation than neutrons. Similar to the neutron increase, this anti-correlation can be explained by the fact that for deeper-situated elevations, there is more atmospheric depth available in which muons can be produced. The antimuon contribution ranges from 0.6 to 1.3 mGy/a, while for muons dose rate values between 0.9 and 1.9 mGy/a are calculated.

Evaluation of the model

When comparing the results presented above with other research, one has to first be aware of how these other results were derived. I.e., what are the differences in the models used, what influences would these possible differences have on the results, or which subset of the results from this work can effectively be compared to the respective research? These influences can sometimes be hard to determine, so that a strict one-to-one comparison of dose values is often not possible. However, a comparison with other works can at least help in estimating if the here presented model yields reasonable results.

To give an example of the above mentioned difficulties in comparing: *Cucinotta et al.* [2002] found present-day dose equivalent values of $\sim$ 0.1-0.2 Sv/a, dependent on the surface altitude analysed. In contrast to the model of this work, their analysis also considers HZE ions, which should lead to higher dose values. However, they analysed the radiation environment for Solar maximum conditions, where resulting dose rates should be lower, as the GCR flux is decreased compared to Solar minimum conditions. E.g., *Dartnell et al.* [2007B] calculate the difference between those conditions to be about 50% (from minimum to maximum). Furthermore, the backscattered component of neutrons is not considered in [*Cucinotta et al.*, 2002]. Additionally, the calculation of the particle propagation through the atmosphere was conducted with a different simulation model (HZETRN). The dose equivalent rates of our model are calculated as $\sim$ 0.31 - 0.38 Sv/a (as presented in App. A.3). We now try a vague estimate of the influences of these differences: Further considering HZE ions to the GCR spectrum would yield an additional absorbed dose of 5 - 10 % in our model. For the dose equivalent this factor should be higher, due to the higher LET of heavy ions. Let's assume an increase of to the dose equivalent of $\sim$ 30 % (in the style of findings from *Dartnell et al.* [2007A]. Subtracting the dose equivalent induced by backscattering neutrons in our model would yield a decrease of around $\sim$ 10 %. The difference in the Solar activity could then account for an additional subtraction of about 50 %. Considering these

three influences, our total dose equivalent rate might end up in the range of 0.19 - 0.23 Sv/a. Considering the differences between the two model and the very rudimentary estimation, the results can be seen as matching up tolerably well.

The research by *Dartnell et al.* [2007A] presents a surface absorbed dose of ~ 0.155 Gy/a, including a model to estimate the dose of HZE ions, at a surface pressure of 6 mbar. This corresponds to a surface altitude of ~ 0 km in this research, where the resulting absorbed dose rate is calculated to be about 0.17 $\pm$0.01 Gy/a. For better comparison of these values, one can derive, in a rough estimation, a dose rate excluding the contributions of all ions with $Z \geq 2$ from their analysis, which yields a value of ~ 0.14 Gy/a. Excluding the alpha particle contribution in our work leads to a dose rate of $\sim 0.155 \pm 0.01$ Gy/a. With the difference in the results from both works being in the range of 10 %, the models show values in good agreement. Further findings, e.g. [*Mileikowsky et al.*, 2000], [*Pavlov et al.*, 2002], also compare relatively well to the respective results from this work.

To add to that, calculations from measurements conducted by the Martian Radiation Environment Experiment (MARIE) [*Zeitlin et al.*, 2004] onboard the Mars Odyssey mission yield dose rates in a Martian orbit ($\sim$ 400 km) of around 21 mrad/day, which corresponds to $\sim$ 76 mGy/a, for the example of August 2003 [*Saganti et al.*, 2006]. The model, presented in this thesis, yields a dose rate of about 165 mGy/a in an altitude of 90 km, which is the highest resolvable altitude for this model. Again, these two values are not strictly comparable. E.g., the latter dose rate was calculated using Solar minimum conditions, whereas in August of 2003 the Sun was in its maximum activity phase. As mentioned above, these different conditions can have an effect of $\sim$ 50%. Considering this would lower our dose rate to around 83 mGy/a, placing it in the same range as the one shown by *Saganti et al.* [2006].

5.1.2. Radiation environment under increased atmospheric pressure conditions

Comparing applicable findings derived from this work's model with other analyses leads to the conclusion that, with the accuracy available for these comparisons, the model calculates dose rates of reasonable congruency. Therefore, the present-day results from presented in Sec. 5.1.1 are taken as a baseline for the studies presented in this section. To gain an overview of the influence an increase of the atmospheric pressure would have on the Martian radiation environment (as expected for early-Mars conditions), three increased pressure levels were analysed, with factors of 25, 50, and 100. For one, this gives a broad range of possible pressure scenarios (e.g., ranging from 6 to 600 mbar at datum altitude), and further the upper limit was chosen to include an atmospheric pressure, believed to at least be the lower boundary for CO_2 pressure necessary to allow

for a continuous existence of liquid water on the surface [*Kahn*, 1985]. If Noachian pressure conditions were significantly higher than $\sim$ 0.6 bar, estimations about these conditions might still be extrapolated from our results.

For this analysis, the PLANETOCOSMICS modelling of Mars was altered by increasing the atmospheric pressure values given in the control macro files with the above mentioned factors.

Pressure increase by a factor of 25

Increasing the atmospheric pressure by a factor of 25 corresponds to a surface pressure at the datum altitude of $\sim$ 155 mbar, covering a range from roughly 60 to 395 mbar for all altitudes. The top panel of Fig. 5.4 shows, exemplarily for 0 km elevation, the PLANETOCOSMICS-simulated surface radiation environment for this scenario. In comparison to the present-day environment, one can see an overall decrease in fluxes of all particle species, which is expected, as the atmospheric depth above the surface is considerably higher in this scenario and, therefore, primary particles should lose considerably more energy propagating down to the surface.

Furthermore, under these conditions, neutral particles are dominating the spectrum nearly over the whole energy range. From energies above some hundred MeV on, the neutron and proton spectra converge, while for energies above $\sim$ 5 GeV muon and antimuon fluxes show the highest values. Furthermore, the change in the fluxes of protons and alphas is the most pronounced. This can be explained by the fact that their spectra are mostly made up of primary GCRs with relatively small contribution of secondary particles, and so the pressure increase has the most effect on them. In particular, it is noticeable that the alpha particle flux is the lowest of all analysed and that we find no alphas below energies of 1 GeV at the surface. However, the latter is an effect of the PLANETOCOSMICS particle tracking process, i.e. in reality a hard cut-off at these high energies is not expected. But due to the low flux of alpha particles this is a negligible side effect.

The resulting absorbed dose rates from the simulation of this scenario can be seen in the bottom panel of Fig. 5.4. One can see that, now, a clear correlation of total dose rate and surface altitude is visible. The total dose rate decreases from 0.085 Gy/a at +10 km elevation to $5 \cdot 10^{-4}$ Gy/a (-10 km). This correlation is due to the influence of the increased atmospheric pressure on the primary particles. In this scenario, the additional atmospheric depth between elevations of +10 and -10 km is much greater than for present-day conditions. Therefore, a significant decrease in the primary particle's energy, and subsequently in its dose contribution and secondary particle production, takes place between these two elevations. This can be seen in the significant devia-

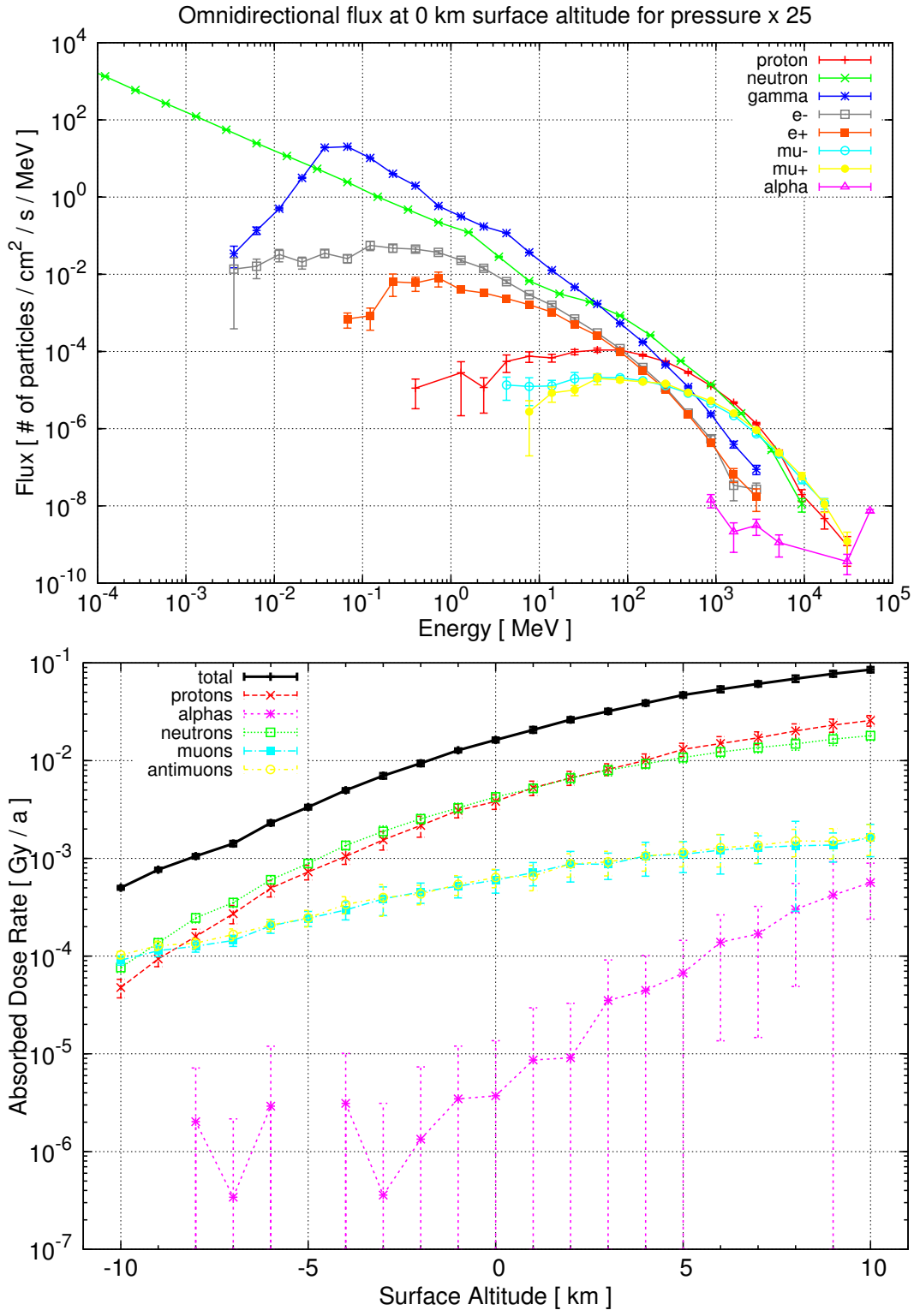

Figure 5.4.: Top: Omnidirectional particle fluxes at the Martian surface at datum altitude for an atmospheric pressure increased by a factor of 25. Simulated with `PLANETOCOSMICS`. Bottom: Resulting absorbed dose rate contributions of selected particle types in dependence of the surface altitude.

tion of fluxes between +10 and -10 km in the left plot of Fig. 5.5, and when further comparing it with the present-day situation shown in Fig. 5.3.

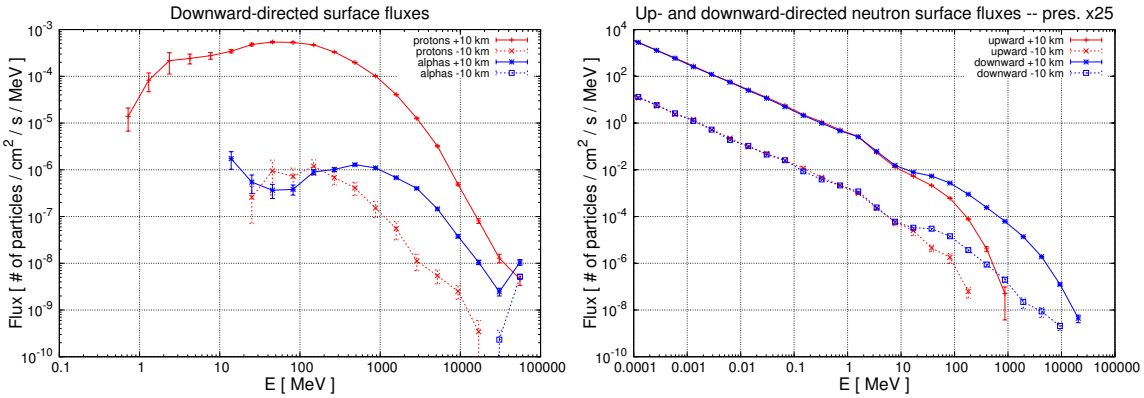

Figure 5.5.: Martian surface fluxes for an increased atmospheric pressure by a factor of 25, calculated with `PLANETOCOSMICS`. Left: Downward-directed proton (red) and alpha particle (blue) fluxes for surface altitudes of +10 km (solid) and -10 km (dashed). Right: Downward- (blue) and upward-directed (red) neutron surface fluxes for surface altitudes of +10 km (solid) and -10 km (dashed).

Following from this decrease in the surface fluxes with decreasing surface altitudes, the resulting downward slope of the proton dose rate is also much more pronounced than for present-day pressure conditions, yielding rates between 25 mGy/a at +10 km and 0.05 mGy/a at -10 km elevation. The absorbed dose rates for alpha particles are calculated to be decreasing from 0.6 mGy/a to 2.5 µGy/a at around -2 to -3 km surface altitude. Due to the low statistics for alpha particles at lower elevations, the bootstrap MC errors are in the same magnitude of or even higher than the mean calculated dose rates for elevations below +5 km, which is why the statistical relevance of the depicted dose values for alpha particles at low elevations is not assured. A further effect of the decrease in the alpha particle flux is – and this becomes more and more pronounced the higher the analysed surface pressure gets – that alpha particles create secondary neutrons and protons via fragmentation due to interactions with the atmospheric molecules (see Ch. 2.1.1). This effect, coupled with a decreasing primary proton flux for higher atmospheric pressure, leads to the mentioned convergence of neutron and proton particle fluxes. The rate of neutrons and protons, created via alpha fragmentation, in their total fluxes increases, the higher the atmospheric pressure is.

Differing from present-day conditions, the neutron dose rates are, in this scenario, not increasing any more with decreasing surface altitude. The neutron contribution rather shows a nearly identical slope to the proton contribution, with a bit lower rates for

high elevations and higher rates from $\sim$ -1 km elevation on downwards. The similarity in the proton and neutron curves is caused by the above mentioned effect that they are influenced by alpha-particle fragmentation at these pressure conditions. The decreasing trend further stems from the fact, that the more pronounced decrease of the primary fluxes with altitude, in this case, outweighs the fact that more secondary neutrons might be produced in the additional atmosphere above lower ground-levels. The right plot in Fig. 5.5 illustrates this. For the high surface altitude both, downward- and upward-directed, neutron surface fluxes are considerably higher over all energy ranges, whereas for present-day conditions the downward-directed flux at low altitudes is higher. The calculated neutron dose values decrease from 18 mGy/a (+10 km) to around 0.075 mGy/a at -10 km.

The decrease in the slope of muon and antimuon dose rates is the least pronounced for all analysed particle species. They are least affected by the pressure increase and the corresponding amount of additional atmosphere they have to propagate through to reach the ground, due to the effects (relativistic energies, lower energy loss) described in Ch. 2.1.1. The rates decrease, nearly equally for both species, from $\sim$ 1.6 mGy/a at high elevations to 0.1 mGy/a (low). Therefore, at low elevations (from roughly -8 km downwards) one can already recognise the situation where the muon/antimuon contribution to the total dose rate begins to outweigh the contributions of the other particle species. This effect is expected for higher atmospheric pressure-levels, e.g. as can be seen on Earth.

Pressure increase by a factor of 50

In the next step, the atmospheric pressure level was set to 50-times the present-day value. This translates to surface pressures between $\sim$ 120 and 800 mbar, with the pressure at datum altitude being around 310 mbar. The resulting radiation environment is shown in the top panel of Fig. 5.6, for the example of 0 km surface altitude. At a first glance, it can already be seen that, while the spectral shapes for the different particle species remain more or less the same compared to the previous scenario, overall the fluxes are expectedly further lowered. Again, muon and antimuons show the highest fluxes for energies $\sim$ 1 GeV, in this scenario with a larger separation to the next highest fluxes. Following the trends shown in Fig. 5.4, the decrease in proton and alpha particle fluxes from the previous scenario is again very pronounced, to the point that statistics for the alpha particle dose calculations is nearly non-existent.

Using these fluxes, the calculation model yields the altitude-dependent absorbed dose rates as shown in the bottom plot of Fig. 5.6. As expected by judging from the previous scenario, the total dose rates are further decreased and still show their correlation

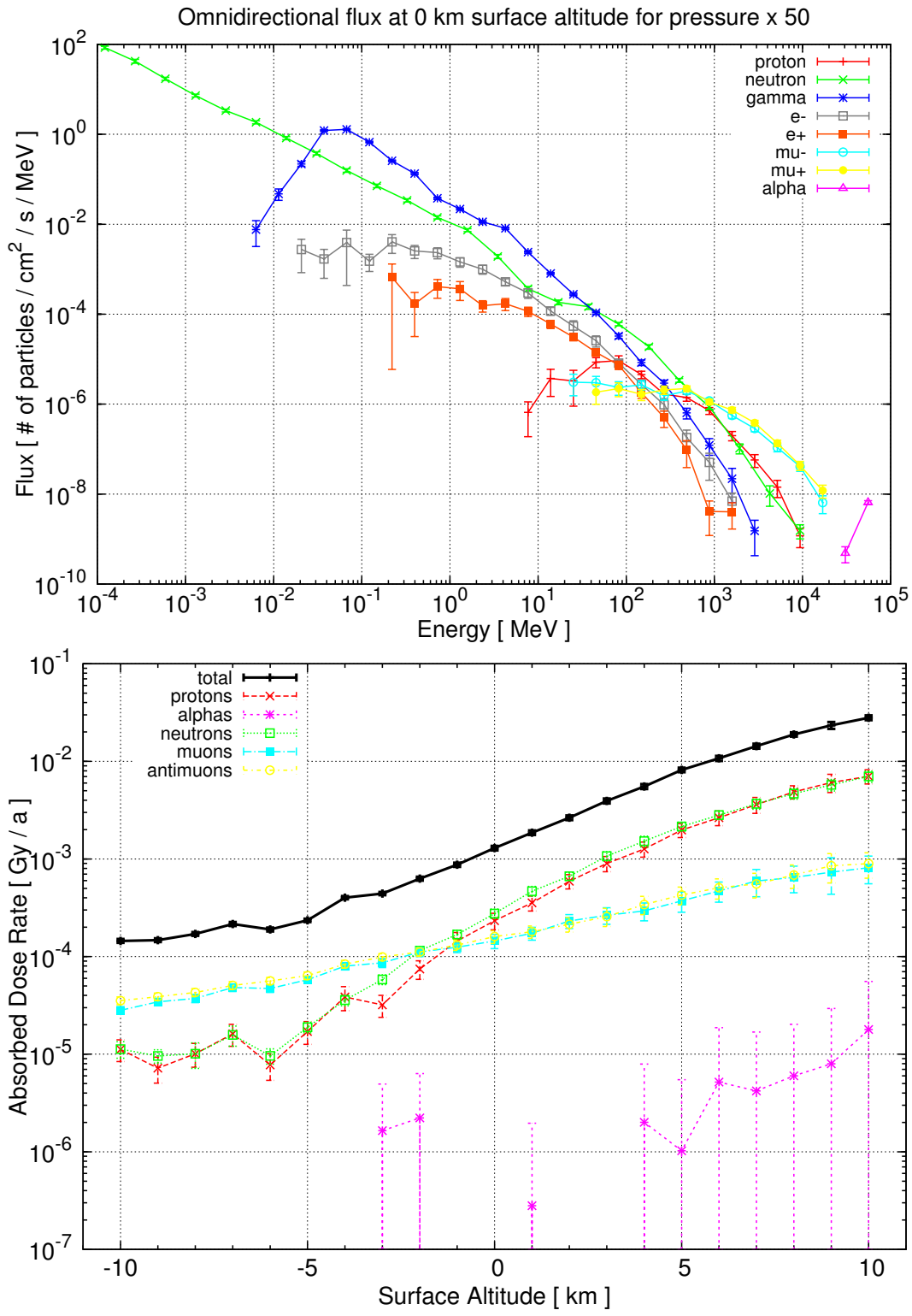

Figure 5.6.: Top: Omnidirectional particle fluxes at the Martian surface at datum altitude for an atmospheric pressure increased by a factor of 50. Simulated with `PLANETOCOSMICS`. Bottom: Resulting absorbed dose rate contributions of selected particle types in dependence of the surface altitude.

with decreasing surface altitude. In this case, they range from $\sim$ 1.45 mGy/a at low elevations to 28 mGy/a (at +10 km). Protons and neutrons show nearly identical curves, i.e. the influence of secondaries created through alpha fragmentation is more pronounced, with their dose rates decreasing from $\sim$ 7 mGy/a to 0.01 mGy/a with lowered altitudes. Furthermore, the proton dose contribution below $\sim$ -4 to -5 km elevation, stems exclusively from protons created by the alpha-particle component of the GCR, i.e. the primary-proton component of the GCR does not contribute to the proton dose rate at the lower elevations. Furthermore, one can see a flattening of the proton contribution curve below these elevations. This effect will be described in more detail in the next section.

The boundary, where muons/antimuons begin to have the greatest influence on the total dose rate, can be found somewhere between 0 and -3 km elevation. The decline in the muon/antimuon contribution slope is again less pronounced than for neutrons and protons and ranges from around 0.85 mGy/a to 0.03 mGy/a for both species. As already mentioned, the statistics for alpha particles is very low and, therefore, the calculated mean values for their dose contribution all show deviations larger than the respective mean value. E.g., at +10 km surface altitude the absorbed dose rate is calculated to be 0.018 ± 0.038 mGy/a. This means the bootstrap MC process had only very few runs in which an energy deposit of an alpha particle could be detected in the water detector.

Pressure increase by a factor of 100

The surface fluxes at 0 km elevation for a pressure increase by a factor of 100 are shown in the top panel of Fig. 5.7. All fluxes are further decreased from the previous scenarios and muons/antimuons, here, dominate the spectrum at energies above $\sim$ 250 MeV. Continuing the previously already very low statistics, a change in the alpha particle flux is not that distinct, as increasing the pressure further does not show a greater influence on the flux, in which only particles in the highest simulated energy bins can be found.

The resulting absorbed dose rates – for surface pressures ranging from $\sim$ 240 mbar to 1.6 bar, with 620 mbar at datum altitude – are shown in the bottom panel of Fig. 5.7. All total dose rates are continuously lower than in the previous scenarios, starting at 3.1 mGy/a (+10 km surface altitude) and then gradually decreasing to 0.06 mGy/a at low elevations.

Here, proton dose rates below $\sim$ +1 to +2 km stem from secondaries created by the alpha component of the GCR. For the neutron contribution this boundary is at roughly 0 km elevation. Therefore, the neutron and proton contribution curves in the

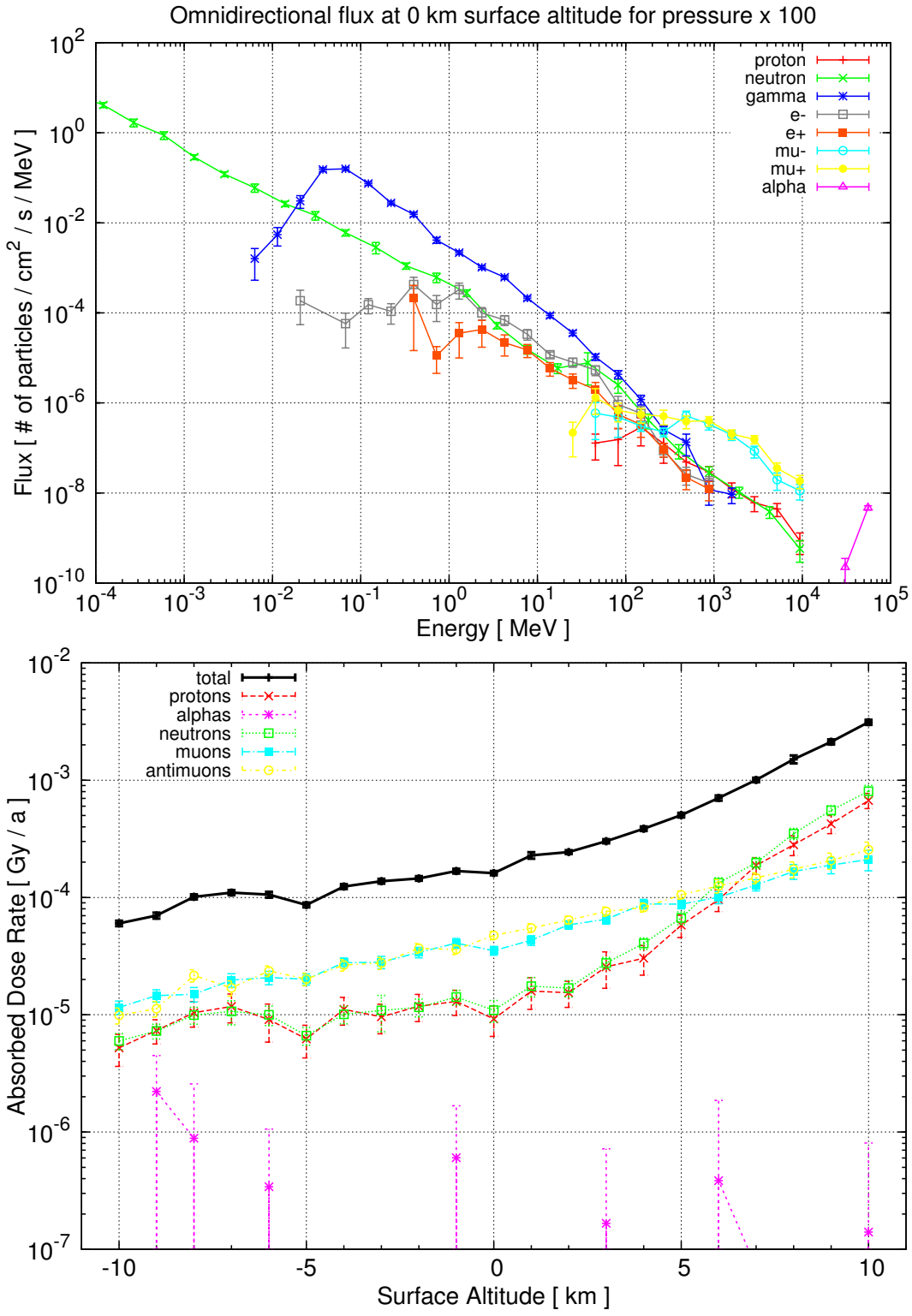

Figure 5.7.: Top: Omnidirectional particle fluxes at the Martian surface at datum altitude for an atmospheric pressure increased by a factor of 100. Simulated with `PLANETOCOSMICS`. Bottom: Resulting absorbed dose rate contributions of selected particle types in dependence of the surface altitude.

top panel of the figure are, again, nearly identical, and are lowering from 0.75 mGy/a to around 5.5 µGy/a with decreasing surface altitude. As mentioned in the previous scenario, below these altitudes one finds a flattening of the dose rate curves to lower elevations, where the primary proton contribution is zero. This effect is something that one would not expect to such an extent. The flattening can also be recognised to a lesser degree for gammas, electrons, and positrons (see Fig. A.1 in App. A.1). It is assumed that these supposedly inaccurate calculations seem to be rooted in the `PLANETOCOSMICS` calculation of the secondary fluxes created by the alpha particle component of the GCR. Investigation yields that contrary to expectations, e.g., the calculated surface proton fluxes do not decrease for deeper elevations in the afflicted range and, therefore, the dose also stays at a constant level. Normally, the dose rates should decrease further going to lower altitudes, as these secondary fluxes should be attenuated by propagating through the additional atmospheric depth. A possible explanation is that due to the very low statistics for particle fluxes for the affected elevations, this attenuation can not be properly represented and, thus, the fluxes for all elevations show roughly the same order of magnitude for the respective particle species. Possible consequences of these inaccuracies are explained in Sec. 5.1.3.

The few alpha particle contributions recognisable in the plot represent, again, mean dose rate values with large deviations. The low statistics further leads to the effect that no clear trend for the alpha distribution is recognisable. Besides from the highest surface altitudes (above $\sim +6$ km), muons and antimuons contribute the most to the total dose for all other elevations.

5.1.3. Comparison of different pressure conditions

To give a better overview of the changes in the surface dose with increased pressure, the upper plot in Fig. 5.8 shows the total absorbed dose rates for certain surface altitudes versus the pressure increase factor, as analysed in Sec. 5.1.2. The general trend shows for all elevations that a higher atmospheric pressure level causes a decrease in the absorbed dose rate at the surface. This, of course, is comprehensible as higher atmospheric pressure means that the incident GCRs have to travel through more atmospheric depth and lose more energy at higher altitudes in the atmosphere. This results in fewer particles being available for interactions in the near-surface altitudes, and therefore lower dose rates.

However, not all particle species show such a monotonically decreasing dose rate progression, or better only protons and alpha particles, whose surface spectra consist mostly of primary particles, show the same characteristics as the total dose curve. The secondary particle species curves differ. This is illustrated in the lower panel

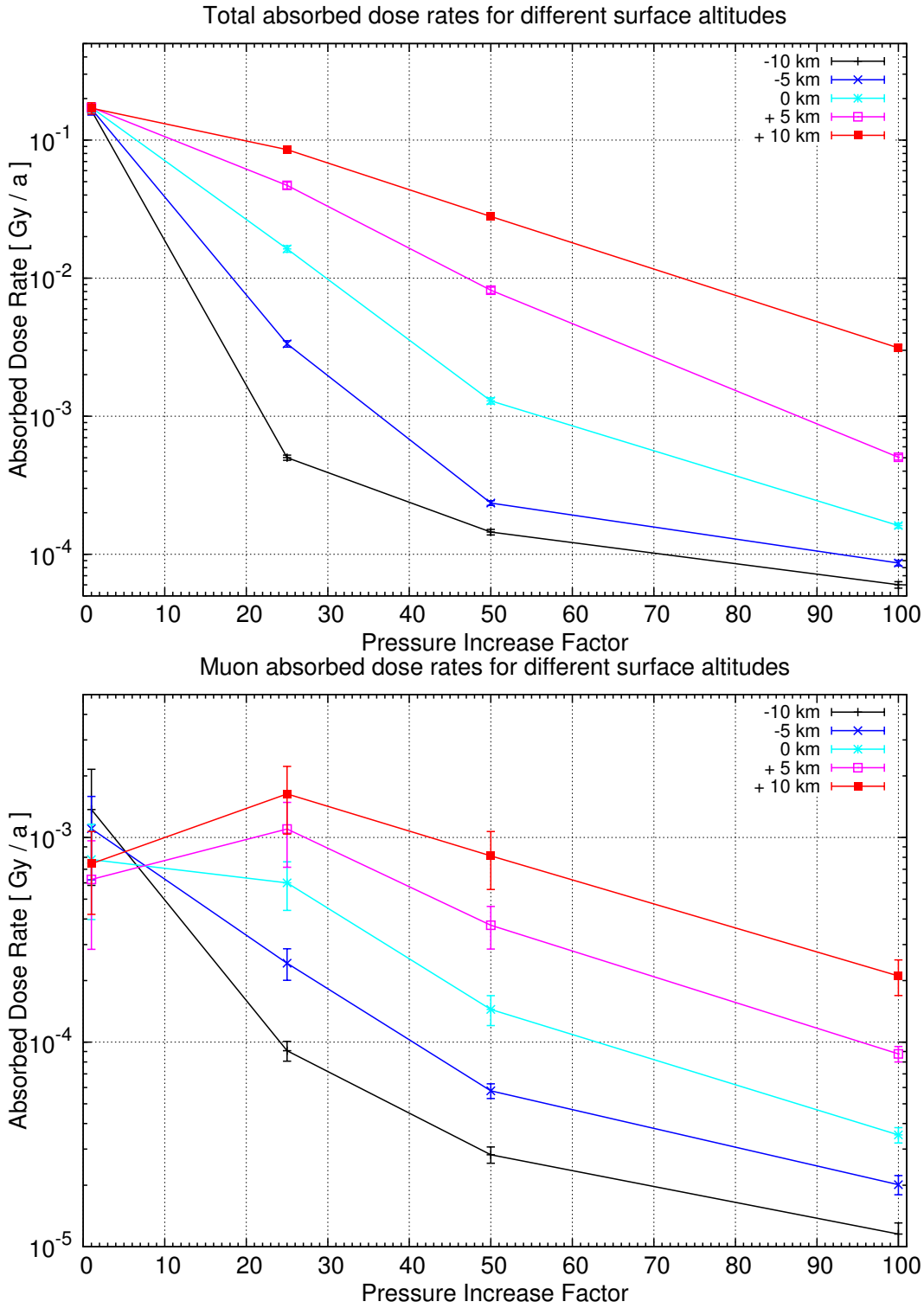

Figure 5.8.: Absorbed dose rates in dependence of the increased atmospheric pressure for different surface altitudes. Shown are -10 km (black), -5 km (blue), 0 km (light blue), +5 km (magenta), and +10 km (red) elevations. Top: total absorbed dose rates. Bottom: muons.

of Fig. 5.8, for the example of the muon-induced absorbed dose rates, as here the following effect is the most pronounced. One can see that for higher elevations the dose rate indeed increases from present-day to 25-times higher pressure conditions. At this pressure level, for high elevations the decrease in the primary particle fluxes is not yet significant enough, so that the additional atmosphere allows for a higher secondary particle production rate. In general, this is the same effect as described in Sec. 5.1.1 for the anti-correlation between neutron dose rates and surface altitude.

Furthermore, for a given pressure scenario the elevation of the surface is also relevant for the radiation exposure. E.g., for a factor of 100, the absorbed dose rate at +10 km elevation is lowered by a factor of about 55 compared to the present-day dose rate. For datum altitude the dose rate already shows a decrease of a factor of $\sim$ 1000, while at -10 km the dose is lowered by a factor of $\sim$2700.

A further interesting point is that, for the deeper shown elevations, the decrease of the total dose rates shows a flattening of the curve to higher pressure increases. I.e., the slope of the decrease is more pronounced for lower pressure levels. In general, such a flattening can be expected as for these high pressures the muon contribution to the dose dominates. As already established, these muons are least affected by increases in atmospheric pressure, respectively depth and, thus, further increases in pressure yield smaller consequences as for the pressure scenarios where other particles dominate the dose contribution. However, the extent of this flattening, found in our results, is believed to be overstated by an artificial effect. This effect happens at high surface pressures for low counting statistics of secondary particles created by the alpha component of the GCR. The `PLANETOCOSMICS`-calculated particle fluxes become inaccurate in the sense that these surface fluxes are expected to be more decreased when going to deeper elevations. Therefore, the recognisable flattened curve progressions of low elevations are likely overstated a bit. In general, this effect should not be too severe, as at the affected surface pressure levels muons dominate the dose rate contribution, and for these the artificial flattening can not be recognised to a larger degree (see Fig. 5.7).

Fig. 5.9 displays the problem in more detail. There, the total absorbed dose rate over all analysed surface pressures is shown (red curve). Note that the pressure values in mbar correspond to Martian conditions and not terrestrial. One can see that the artificial flattening starts at about 500 - 600 mbar. From this pressure on, an expected, more natural flattening would most probably yield lower dose rates than the calculated. The black line depicts an arbitrary dose rate curve for these higher pressures and attempts to indicate a more natural curve progression. Thus, the calculated surface dose rate at, e.g., 1600 mbar of $\sim 6 \cdot \sim 10^{-5}$ could well be in the range of up to one order of magnitude lower. Furthermore, although the `PLANETOCOSMICS`-limited accuracy of the model at these high pressures is regrettable, the consequences for the underlying

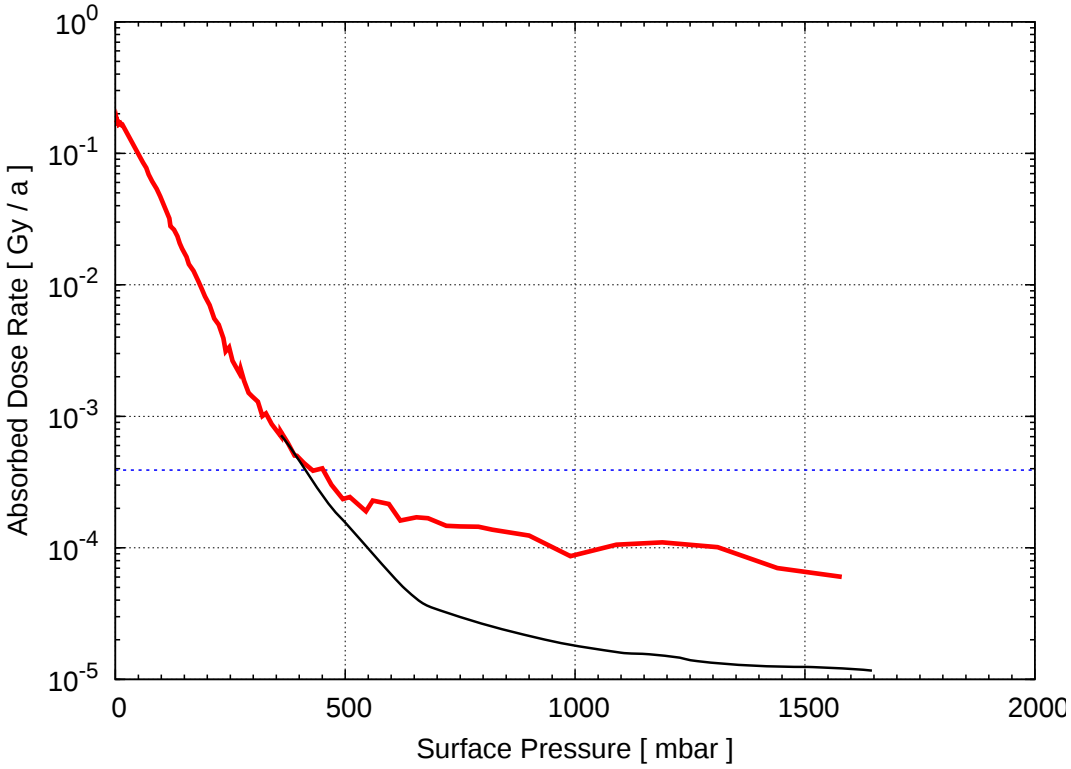

Figure 5.9.: Calculated total absorbed dose rates in dependence of the surface pressure (red line). The black line represents an idealised, arbitrary suggestion for the dose rate progression without the artificial overestimation of the particle fluxes at high pressure levels. The dashed blue line shows the value of the average GCR-induced absorbed dose on the Earth's surface at present day (from [*UNSCEAR*, 1993]).

question of life on Noachian Mars should not be too large. In [*UNSCEAR*, 1993], the annual effective dose rate at the terrestrial surface, induced by GCRs, is given as 3.9 $\cdot$ 10^{-4} Sv/a. As the quality factor of this dose is $\sim$ 1 at terrestrial surface altitudes, this translates to a value of 3.9 $\cdot$ 10^{-4} Gy/a, which is displayed as the dashed blue line in Fig. 5.9. Now, as one can see from the explanation above, for high Martian surface pressures both the potentially too-highly calculated total dose rates, as well as the estimated values for the corrected lower dose rates, are below this terrestrial value. As the average radiation environment on Earth is not, per se, detrimental to the development of life, thus, even an over-estimation of high-pressure dose rates derived from our model yields values below a boundary value for a radiation exposure potentially critical for a sustainment of possible life.

5.2. The subsurface radiation environment

When analysing the radiation exposure on Mars in the context of its influence of possible survival chances of microbial life, it makes sense to not only look at the surface, but also determine radiation doses beneath it, where such life forms also might have existed or even could possibly still exist in dormant states. Therefore, in this section results for calculated total subsurface dose rates are presented. Furthermore, the contributions of different particle species to the overall dose rates are given in tabular form.

Fig. 5.10 shows the total absorbed dose rate in dependence of the subsurface depth for three exemplary elevations, low = -10 km (plotted in blue), mid = 0 km (black), and high = +10 km (red), for present-day conditions. As one can see, for all three elevations

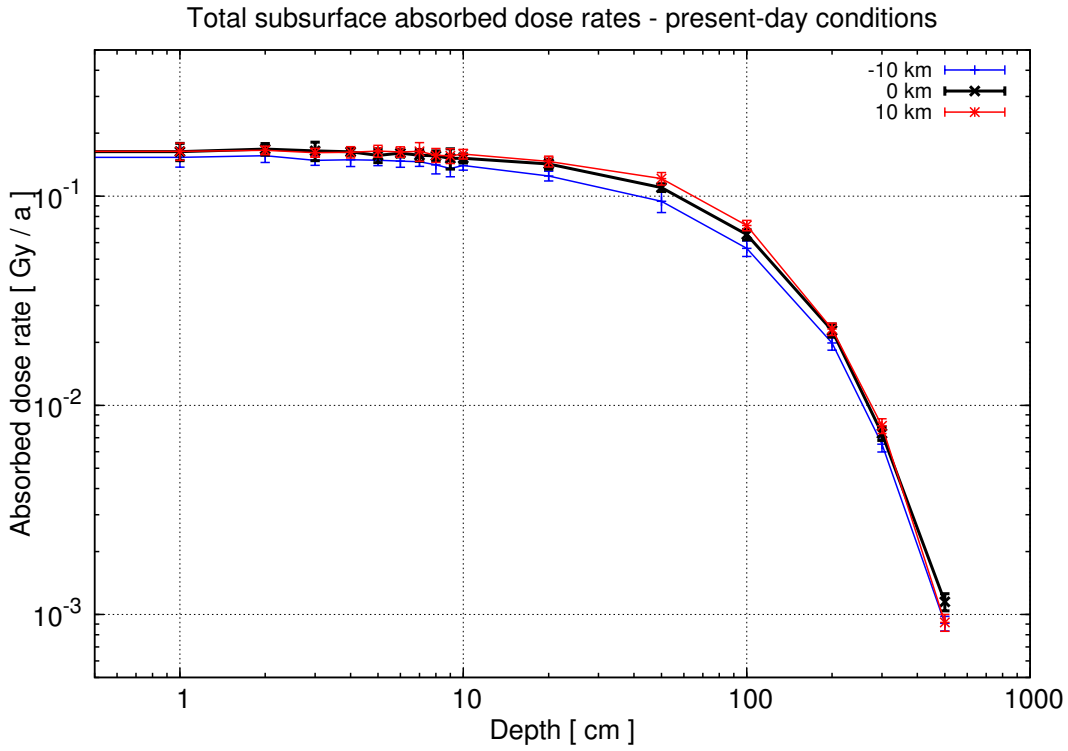

Figure 5.10.: Absorbed dose rates in dependence of depth beneath the surface for present-day atmospheric conditions. Shown for surface altitudes of -10 km (blue), 0 km (black), and +10 km (red).

the dose rate curves show nearly identical curve progressions and magnitudes of dose rates. This can be explained by the following: First, it was shown that the dose rates at the surface are roughly constant over all elevations. Second, the differences in atmospheric depths above the individual surface altitudes are rather small for the present-day pressure level. Consider the following simplified example: The difference in

atmospheric depth above -10 km and +10 km surface altitude is $\sim 37.5\ \frac{g}{cm^2}$. Converted for the soil, this would mean that a particle "starting" at +10 km surface altitude would have to propagate through $\sim$ 22 cm of soil (with a soil density of 1.7 $\frac{g}{cm^3}$) to achieve the same amount of traversed depth (soil and atmospheric) as a particle "sitting" at a surface altitude of -10 km.

On the first 10 cm the dose rate decreases about 10 % from its initial surface value, after 1 m it shows a decrease of roughly 65 % (from the surface value), after 3 m a total dose rate of about 5 % of the surface dose is found, and after 5 m the dose rate is less than 1 %. Analysing deeper soil layers should yield a further decrease in the dose rate (following the clearly visible trend in the figure) until at some depth it reaches 0. The primary particles that are for the main part responsible for secondary particle production, only have a limited penetration depth into the soil until they have lost all their energy. And as described before, at some point this continuous decrease in the primary fluxes leads to the subsequent decrease in secondary particle production.

The contributions of different particle species to the total subsurface dose rates can be seen in Table 5.1 where, for one, average total dose rates are shown for different subsurface depths. Furthermore, the mean percentages of contributions to the total dose by the different particle species are listed. In the table, the strong attenuation

Table 5.1.: Contribution of different particle species to the total subsurface dose rate for present-day conditions. Given are mean values for the total dose rate and mean percentages to that dose for each particle species.

Type	Surface	10 cm	1 m	3 m	5 m
Total Dose (mGy/a)	$\sim$ 170	$\sim$ 150	$\sim$ 65	$\sim$ 7.3	$\sim$ 1
Protons	53 %	51 %	38 %	29 %	27 %
Alphas	10 %	7.5 %	1.2 %	0.5 %	0 %
Neutrons	13 %	18.5 %	35 %	43 %	34 %
Gammas	6 %	6 %	9.5 %	12 %	10 %
Electrons	8.5 %	8 %	8 %	6.7 %	4 %
Positrons	7.5 %	7 %	6.5 %	4.1 %	5 %
Muons	0.6 %	0.5 %	0.6 %	2 %	8 %
Antimuons	0.8 %	0.6 %	0.8 %	2.7 %	11 %

of the primary particles can be nicely recognised in their percentages of total dose contribution. The proton contribution, for example, decreases from $\sim$ 53 % at the surface to 27 % in 5 m depth. The alpha particle contribution, contributing 10 % to the dose at the surface, already decreases to roughly 1 % at 1 m beneath the surface.

As a general conclusion, it can be stated that the composition of the total dose rate is dependent on the soil depth. While for the surface half of the dose is contributed by protons, deeper in the soil the contribution is more diverse, e.g. at 5 m depth nearly 20 % is contributed by muons and antimuons.

Fig. 5.11 shows the resulting subsurface dose rates for the different increased pressure conditions. In the top panel, calculations for an increase factor of 25 are shown. While the general progression of the curves is similar to the ones presented in Fig. 5.10, the difference to the previous scenario is that the surface doses show a wider distribution and, therefore, the steepness of the decrease is different for the three elevations shown. While the dose rates for 0 km (plotted in black) and +10 km (red) elevations show relatively similar decreases, the dose rate for -10 km (blue) surface altitude, where the surface dose rate is already about two orders of magnitude lower, shows a less pronounced decrease. E.g., at 1 m soil depth the deep elevation sees a decrease of $\sim$ 50 % (compared to the surface dose), while for the higher surfaces the doses are about 70 % lower than at the surface. At 5 m the subsurface dose are 20 % (low elevation) of the initial surface dose, respectively $\sim$ 2 % (mid) and $\sim$ 0.5 % (high). The contribution rates of the different particle species, again, vary with the soil depth. While we find that roughly 50 - 60 % of the total dose is contributed by protons and neutrons in the first meter of the soil, at 5 m muons and antimuons contribute about 90 %. A list of contribution percentages can be found in Table A.2 in App. A.2.

In the mid panel of Fig. 5.11, the scenario of a 50-times increased pressure level is shown. Here, the two elevations with the lower surface dose rates, again, show a less pronounced decrease, compared to the high elevation. For the latter the dose decreases about 73 % after 1 m soil depth and to $\sim$ 1.5 % in 5 m depth. For the lower elevations, the dose rate decrease after 1 m depth is just $\sim$ 53 %, while after 5 m the dose rate value still shows 20 % of the initial surface doses. However, as one can see in the plot, for these deep-situated surface altitudes, the dose rate curves are flattened in the larger soil depths, similar to the problem described in Sec. 5.1.3. As can be seen in Table A.2, again, the proton dose rates are overestimated due to the quirks in the flux calculating by `PLANETOCOSMICS`. Otherwise, one can see that the muon/antimuon contribution (23 % at the surface) is raised to $\sim$ 50 % at 1 m soil depth, where the artificial flattening is not yet that pronounced.

The pressure increase with a factor of 100 can be seen in the lower panel of the figure. Here, the artificial progressions of the curves (for low elevations) are even more visible, so that even for this high pressure environment and a large soil depth of 5 m protons and neutrons are calculated to still contribute 25 % to the dose. This overestimation gets even clearer, when comparing the contributions of 5 m soil depth with the ones from 1 m, where protons and neutrons contribute just 4 % to the dose.

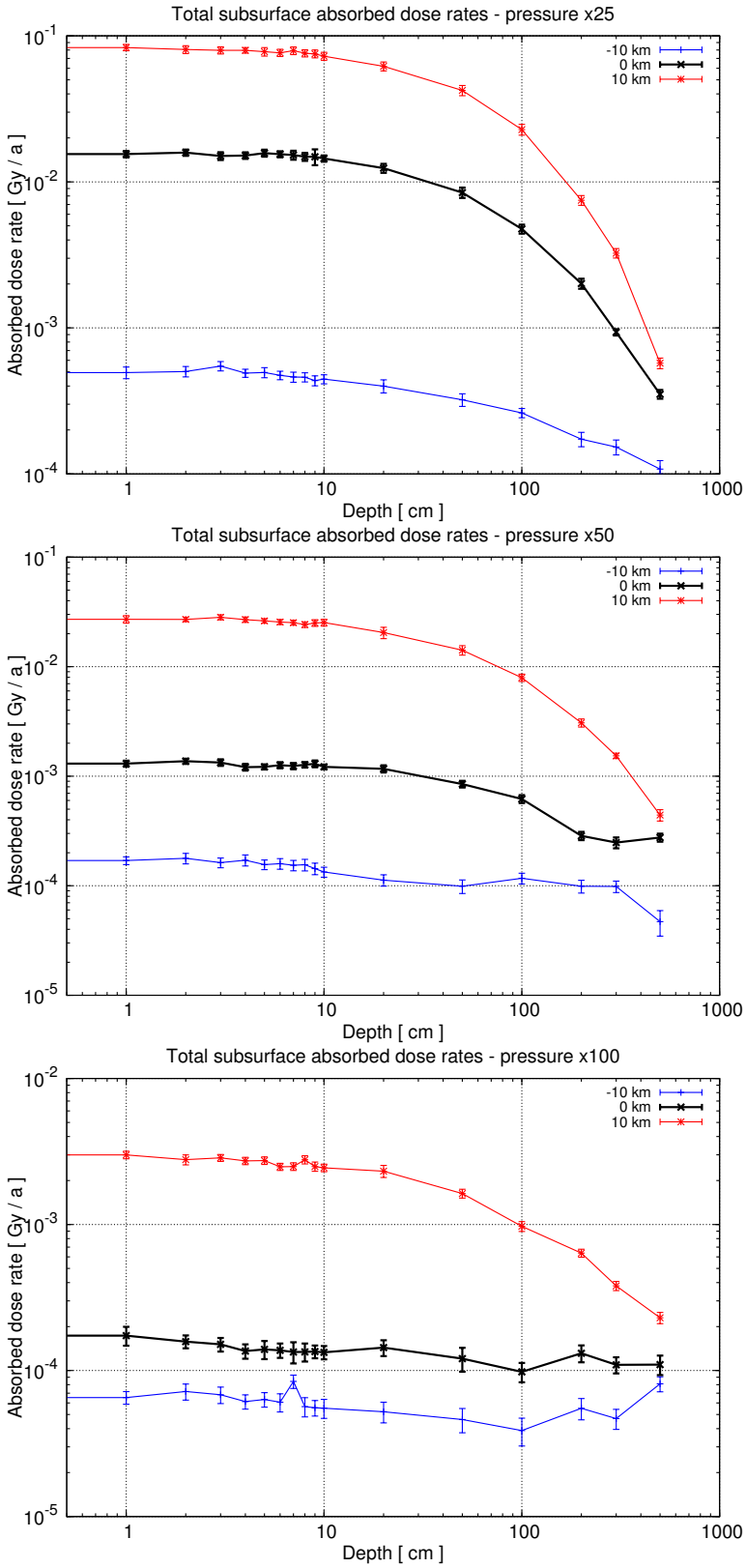

Figure 5.11.: Absorbed dose rates in dependence of depth beneath the surface for different pressure conditions. Shown for surface altitudes of -10 km (blue), 0 km (black), and +10 km (red). Top: Increased atmospheric pressure with a factor of 25. Mid: Increase factor of 50. Bottom: Increase factor of 100.

Therefore, the decreases of the total dose rates are also differing from the high elevation to the lower ones. At 1 m soil depth, the surface dose of +10 km elevation has decreased to 33 %, whereas for the other elevations the dose rates are still above 50 % of the initial value.

5.3. The influence of water on the radiation environment

Besides from the biological importance of water for an emergence of life, the influence of bodies of surface or sub-surface water can also directly influence the radiation environment. The most interesting point for this is the moderation of neutrons by hydrogen via elastic scattering, as described in Ch. 2.2.1. As established in the previous sections, neutrons can contribute significantly to the radiation exposure. Therefore, in this section the influence of water on the radiation environment is examined. This research is conducted for two different scenarios: For one, it is analysed what influence the presence of surface water has in a high-pressure-level scenario. Furthermore, the effects of subsurface water ice, modelled in accordance with present-day conditions, on the dose are researched.

5.3.1. Liquid surface water

As described, there is substantial evidence that Noachian Mars once possessed large volumes of liquid water on the surface. As findings suggest that a CO_2 pressure of at least 0.6 bar is necessary to allow for a sustained presence of liquid water on early Mars, the research on this topic focuses on the pressure level with an increase factor of 100. The model was set up to test three scenarios: a 1 m layer of water on the surface (representing a river bank or shoreline), a 10 m layer (as an equivalent to a river), and a 200 m layer (e.g. for a deep lake), with the idea to analyse if deeper water layers show a significantly more pronounced influence. In the previous sections, it was already established that for high pressure scenarios, the model probably overestimates dose rates from protons and neutrons. Therefore, here results for high altitudes are discussed. Assumed changes for deeper elevations are discussed at the end of this section.

As a starting point, the total absorbed surface dose for the standard dry Mars model was calculated as $\sim$ 3.1 $\pm$0.2 mGy/a for +10 km elevation with a pressure increase by a factor of 100. As can be seen in Table 5.2, adding a 1 m layer of water atop the soil yields a surface dose rate of 3.2 $\pm$0.2 mGy/a. Note that, when talking of surface dose rate in this and the following considerations, the dose on top of the water layer is meant. Thus, the mean dose shows a marginal increase of 3 %. However, considering

the errorbars the significance of this difference can not be assured. The 10 m water layer shows a surface dose rate of 2.9 ±0.2 mGy/a. Again, no significant deviation in the total dose rate can be detected. Modelling the 200 m layer of water yields a surface dose rate of 2.6 ±0.1 mGy/a. Here, at least a slight decrease is recognisable. However, most probably this is due to the uncertainties in the derived dose rates and not a statistically significant decrease.

Table 5.2.: Surface dose rates for scenarios with a water layer modelled above the soil. Shown are the total and the neutron-induced dose rates on top of the water layer for depths of 0 m (dry model), 1 m, 10 m, and 200 m.

Amount of surface water	none	1 m	10 m	200 m
Total dose rate (mGy / a)	3.1 ±0.2	3.2 ±0.2	2.9 ±0.2	2.6 ±0.1
Neutron dose rate (mGy / a)	0.81 ±0.1	0.64 ±0.07	0.6 ±0.09	0.58 ±0.08

Going from the following preliminary considerations, this lack of influence is not that surprising. When analysing the surface dose rate, one has to remember that part of the contributing radiation stems from particles coming from the upper half space. This contribution is not at all affected by a presence of water, as we are calculating the dose, as mentioned, on top of the water layer, respectively on top of the soil for the dry model. Thus, only the backscattered component can be afflicted by the changed surface conditions.

After having shown that the surface dose rate does not seem to be significantly influenced by an added presence of surface water, a further look at the different particle-species contributions to the doses is warranted. An analysis of the contributing species for the four presented scenarios (dry, 1 m, 10 m, and 200 m of water) shows that, expectedly, the neutron dose rate seems to be the most dependent on the amount of water added, while the doses induced by the other species show only very small deviations, if at all, under the different conditions. As summarised in Table 5.2, the initial 0.8 mGy/a for the dry model are decreased to 0.64 mGy/a for the 1 m water layer (here, considering the error bars these values can still be brought in congruence), 0.6 mGy/a for 10 m water, and 0.58 mGy/a for the 200 m layer. It can be also seen that the depth of the water layer is less essential for the surface dose rate. The mean dose rates decrease about 20 % when adding a 1 m layer of water, while expanding the layer to 200 m yields only a further decrease of $\sim$ 10 %.

As mentioned, this difference in the neutron dose rates stems from their backscattered component created in the ground. To clarify this, Fig. 5.12 shows the upward-directed neutron surface fluxes for the four scenarios. There are two interesting points to be

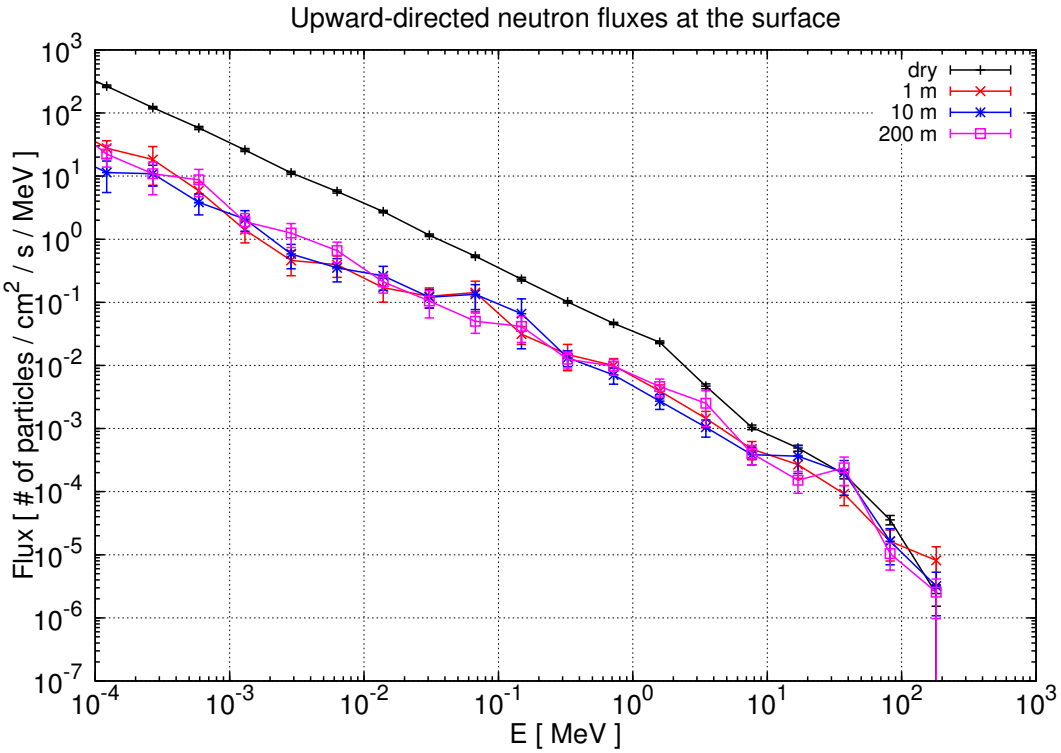

Figure 5.12.: Upward-directed neutron fluxes at the surface. Calculated for an increased pressure level with a factor of 100 at +10 km elevation. Shown are four scenarios: No surface water (black), 1 m water layer at the surface (red), 10 m water (blue), and 200 m water (magenta).

derived from this plot. For one, one can clearly see that for energies below 20 - 30 MeV the dry model (plotted in black) shows a distinctively higher flux than the models with added water (1 m: red, 10 m: blue, 200 m: magenta). The second point is that the fluxes for the water-added scenarios show no significant differences within the error bar margins. For energies above 20 MeV the integrated fluxes are nearly identical for all scenarios, at $\sim$ 0.01 particles cm^{-2} s^{-1}. In the range from 100 eV to 20 MeV (as shown in the figure), the integrated fluxes for the water-containing cases all show values $\sim$ 0.08 particles cm^{-2}. The dry model yields an integrated flux of around 0.56 particles cm^{-2}, showing the influence of the water layers on the flux. Now, why do the fluxes for the water-containing scenarios not differ? This can be explained, when remembering that, here, a high-pressure-level scenario, with a surface pressure at the considered elevation of around 240 mbar, is investigated. Therefore, the incident primary GCRs, and secondaries created in the atmosphere, are already strongly diminished when reaching the planetary surface. Subsequently, secondary

particles, created in the soil, are for the most part created in the first meters of the ground. Thus, adding a 10 m or 200 m layer of water yields no decisive difference in the flux of the upwards propagating neutrons.

Replacing the top layer of the denser regolith with water, however, does have a an influence on the subsurface dose rates. As a reminder for the following discussion: In PLANETOCOSMICS the surface water is modelled as the top layer of the soil. Therefore, when talking about surface, strictly speaking it refers to the bottom of the atmosphere. E.g., in the model containing 1 m surface water, a subsurface depth of 50 cm is actually 50 cm deep in the water (and 50 cm above the regolith), while for the dry model it would be 50 cm in the regolith.

Fig. 5.13 shows the total dose rates in dependence of the depth beneath the surface for the model with a 1 m layer of surface water (solid line) and for the dry model (dashed). As one can see, while starting out at the same level at the surface, the dose

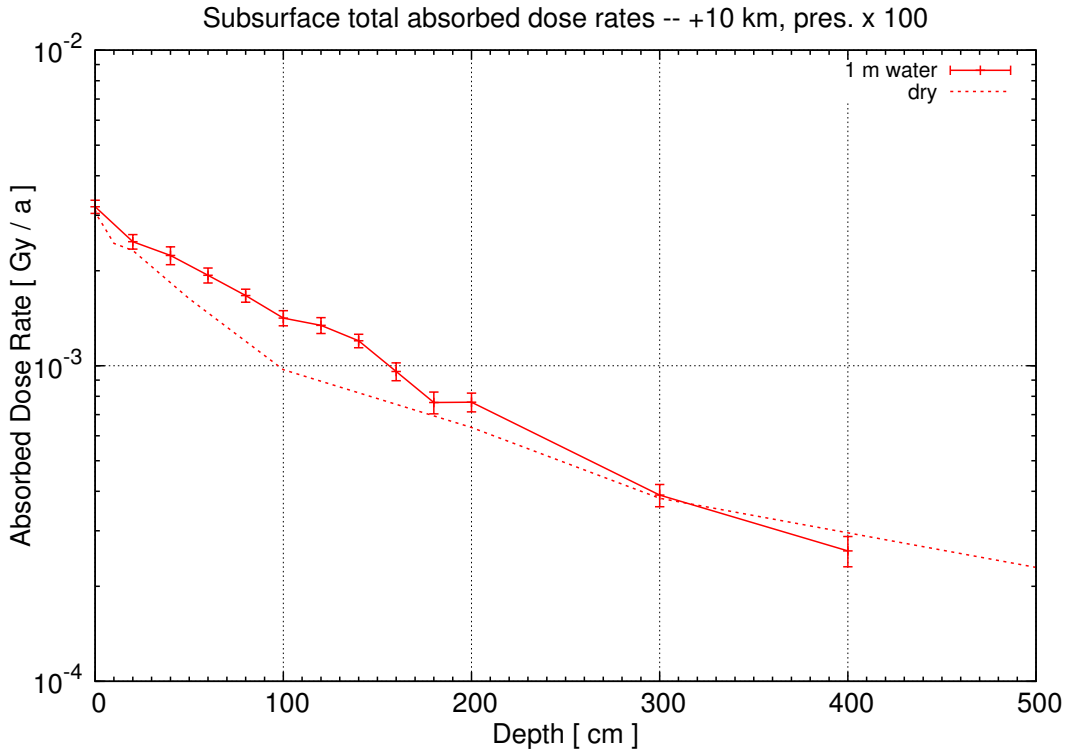

Figure 5.13.: Total absorbed dose rates in dependence of the subsurface depth at an elevation of +10 km for an increased atmospheric pressure level of a factor of 100. Shown are the calculated dose rates from the model containing a 1 m surface water layer (solid line) and from the dry model (dashed line). Note that for the water-containing model, the first meter of subsurface is actually the surface water.

rate curve of the "wet" setup shows a less steeper decline for about the first one and a half meters (including the water layer), with a maximum dose rate increase of about $\sim$ 45 - 50 % compared to the dry model. A steeper decrease then sets in and the dose rate again reaches the level as the one from the dry model at about 3 - 4 m. This behaviour stems from the fact that the layer of water has a lenser density and, thus, incident particles can propagate further, respectively lose less energy in the first meter, compared to the normal regolith. After passing the water layer, the particles have to traverse the denser regolith and the dose rates decrease faster. The dose values then approximate the ones from the dry model, as the overall traversed depths for both models get more and more similar the deeper the layer is.

In the following, assumed changes when analysing deeper elevations are discussed. For the discussion of the surface dose rates the above mentioned considerations still hold true. Thus, for deeper elevations these will not change significantly when adding surface water. The difference in subsurface dose curves between wet and dry model, however, will be less pronounced. To explain this, one has to consider that the lower the surface altitude is the more amount of atmosphere is found above that surface. Therefore, the different densities of the ground for the water-containing and the dry model have a lesser influence. As a simplified example, the atmospheric depth above the surface is 10 $\frac{\mathrm{g}}{\mathrm{cm}^2}$. 1 m of water with a density of 1 $\frac{\mathrm{g}}{\mathrm{cm}^3}$ adds an additional depth of 100 $\frac{\mathrm{g}}{\mathrm{cm}^2}$, which adds up to 110 $\frac{\mathrm{g}}{\mathrm{cm}^2}$. A 1 m thick layer of soil (1.7 $\frac{\mathrm{g}}{\mathrm{cm}^3}$ density) yields 180 $\frac{\mathrm{g}}{\mathrm{cm}^2}$ of total depth. Now, consider the case of an atmospheric depth of 1000 $\frac{\mathrm{g}}{\mathrm{cm}^2}$. Then, the resulting total depth beneath 1 m of water would be 1100 $\frac{\mathrm{g}}{\mathrm{cm}^2}$, and beneath 1 m soil 1170 $\frac{\mathrm{g}}{\mathrm{cm}^2}$. The percental decrease in depth when modelling a water layer is, thus, less pronounced for the latter scenario.

5.3.2. Subsurface water ice

The present-day Martian conditions do not allow for a prolonged presence of liquid water. However, in ice form it is found in larger amounts even today. As described in Ch. 3.1, water ice is found in the polar caps and, mainly in the subpolar, high-latitude regions in permafrost layers beneath the surface. For this research, the permafrost-containing soil was modelled in accordance with the findings of *Mitrofanov et al.* [2004], as alternating layers (one layer regolith followed by a layer of water, and so on) of a total depth of 20 m, containing a mixture of regolith (with the default, dry composition) and water (16 % water by mass).

Similar to the considerations in the section above, the resulting surface doses are not expected to show large differences to the ones found for the dry model. Deeper beneath the surface, however, we should expect higher dose rates in the water-ice scenario. Due

to the mixture of ice- and regolith-containing layers, the overall density of the soil is reduced. Thus, particles can propagate deeper into the ground, leading to a less steeper decrease of the dose rate with depth [*Dartnell et al.*, 2007B]. Contrary to the above shown surface-water model where the dose rates curves of dry and wet model converge for deeper subsurface layers, here, the shallower curve progression should be continuous to deeper depths, as the ratio between densities in the water-ice and the dry model stays constant.

The calculated results show indeed that the surface dose rates from the water-ice containing model lie, on average, around ±3 % of the dry model dose rates. The next step, now, is to analyse the subsurface dose rates. As an example, Fig. 5.14 shows the resulting subsurface dose rates for the water-ice model (solid lines), along with the subsurface dose rates of the dry model (dashed lines), for the different pressure conditions at an elevation of +10 km. For the present-day (black) and 25-times-higher

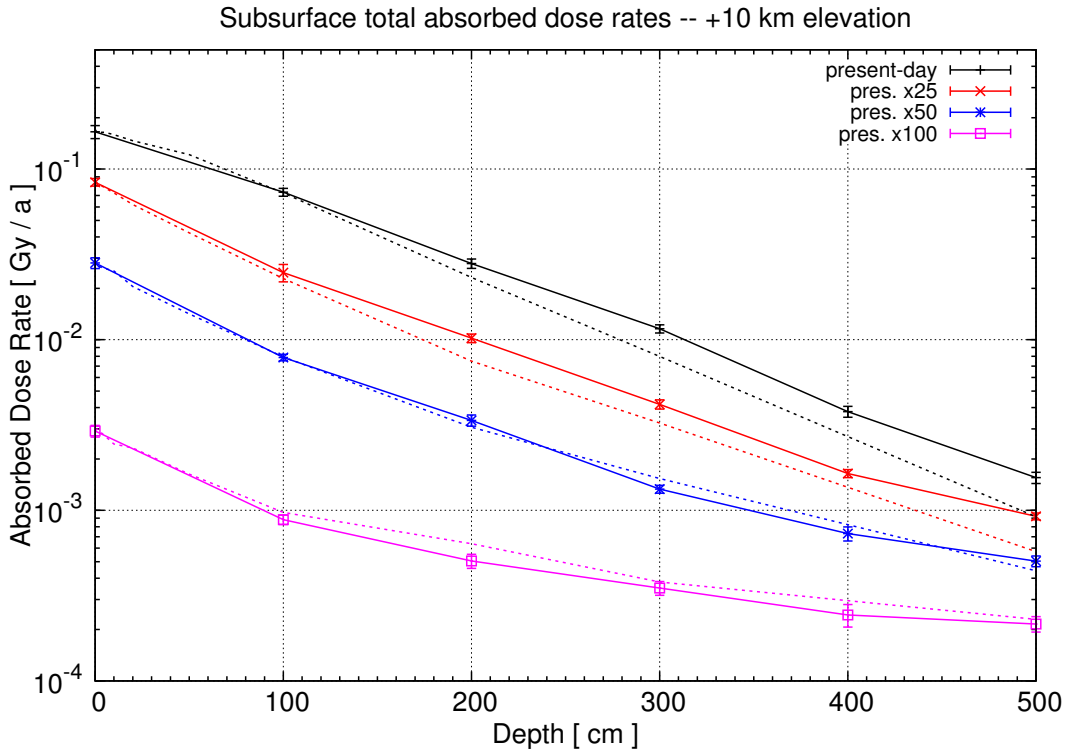

Figure 5.14.: Total absorbed dose rates in dependence of the subsurface depth for different atmospheric pressure conditions at an elevation of +10 km. Shown are the calculated dose rates from the model containing a 20 m water ice layer on top of the soil (solid lines), and from the dry model (dashed lines), for present-day conditions (black), a pressure increase factor of 25 (red), a factor of 50 (blue), and 100 (magenta).

(red) pressure levels, it is clearly visible that deeper subsurface layers see higher dose rates. While at 1 m depth the dose rates show no difference from the ones from the dry model, at 2 m depth they show an increase of about 10 - 20 % for present-day conditions (taking into account all analysed elevations), respectively $\sim$ 30 % for the increase factor 25. At 5 m subsurface depth, the water-ice model yields an average increase of 50 % for present-day (with a maximum increase of 70 % for the +10 km elevation), respectively $\sim$ 45 % with a maximum difference of 62 % (+10 km) for the pressure increase of 25. Looking at the subsurface dose rate contributions by different species, in accordance with the above preliminary thoughts, protons contribute more in deeper layers than for the dry model. E.g., at 5 m depth protons contribute around 7 % more to the dose than for the dry model. Furthermore, as due to the less dense material particles can propagate further, the percentage of muon/antimuon contribution is lessened by 10 - 20 %.

For higher pressure increases of factors 50 (plotted in blue in Fig. 5.14) and 100 (magenta), no clear deviation from the dry model can be found for the dose rates. While the curves in the figure might imply that the dose rates of the dry model might on average even be higher, the detected differences lie in the uncertainty ranges of the respective errorbars. That no significant changes are detected can be explained by the circumstance that for higher pressure levels changes in the soil density are less significant, as explained in the simplified example in the previous section.

As a conclusion, it can be stated that the model calculations yield that the presence of liquid surface water in a high-pressure scenario shows no significant influence on the surface dose rate, due to the fact that mainly upward-propagating neutrons from the soil are affected by the water. E.g., in a very simplified approach, if one was to keep the dose rates contributions from all other considered particle species fixed, the derived change by the neutron-induced contribution would yield a decrease of the total dose of about 5 - 7.5 %. However, in the soil beneath the water, dose rates can be higher than for a dry soil (when taking the bottom of the atmosphere as the reference surface), as the incident radiation is less attenuated by the less denser water. For a 1 m water surface layer at high elevations, we find peak values of about 50 % higher dose rates in the first 50 cm of the soil below the water, compared to values for a dry regolith in the same depth from the surface. For lower elevations, this difference in the subsurface doses is estimated to be less pronounced. Furthermore, the presence of permafrost ice in the ground, as can be found on present-day Mars, also has no significant influence on the surface radiation. However, dose rates beneath the ground are, again, less attenuated with soil depth. In dependence of increasing subsurface depth, the calculations yield higher dose rates of up to 50 % (at 5 m soil depth), compared to dry soil, for present-day conditions. For higher pressure levels, this water-ice-induced dose rate difference

diminishes, as here a lowering of the soil density with water ice is less influential due to the high amount of residual atmosphere above the ground.

6. Interpretation of the results in astrobiological context

In this chapter the findings from Ch. 5 are brought into the context of astrobiology, in particular how the calculated radiation exposure would have affected the survival chances of any possible life on early Mars. As this radiation exposure is not only evoked by GCRs, as analysed in this work, estimates on the influence of further contributing factors are given.

As described in Ch. 5.1, the radiation exposure, resulting from GCR-interactions with atmosphere and soil, on early Mars was in all likelihood significantly lower than today. Considering that the annual mean absorbed dose rate induced by GCRs on Earth at sea-level is about 0.39 mGy/a, the findings show that this terrestrial value is underrun for pressure increase factors higher than $\sim$ 65 - 75, in reference to the surface pressure at Martian datum altitude. However, for Noachian conditions research suggests at least an increased pressure level 100-times higher (again, referencing the datum altitude for this estimate). Our calculations for this atmospheric pressure level increase yield dose rates between 0.06 and 3 mGy/a depending on the surface altitude (from low to high), which corresponds to decreases from present-day values ($\sim$ 165 - 175 mGy/a) by factors between 55 (high elevations) and 2700 (low). Furthermore, as this pressure level presents a lower boundary for suggested Noachian conditions and the presented dose rates for the highest analysed surface pressures might be overestimated by the model, an actual Noachian surface dose rate should in all likelihood lie even lower than these values. Thus it can be concluded that the GCR-induced radiation environment should have posed no obstacle for an emergence of life.

6.1. Estimation of further dose rate contributions

If we, now, postulate such an emergence of simple life forms, such as bacteria, on Noachian Mars, it is interesting to see what the presented findings can implicate for the sustainment of this life over longer time periods. For this, it is important to consider that GCRs do not represent the only contributing factor to the radiation field.

A further influence is the natural background radioactivity from the planet, stemming

from unstable radionuclides and their decay processes. As described in *Mileikowsky et al.* [2000], this natural background is primarily created by the following long-lived radionuclides and their decay chains: Th^{232}, U^{235}, U^{238}, and K^{40}, resulting in an estimated present-day radiation dose of 0.4 mGy/a. Thus, the present-day radioactivity is less than 1 % of the GCR-induced surface radiation, and even beneath the surface our present-day model yields higher values down to the lowest analysed depth of 5 m ($\sim$ 1 mGy/a). As this radiation comes from decays of unstable elements with long half-lives, going back in time yields higher background radioactivity. *Mileikowsky et al.* [2000] calculate the expected background radiation dose 4 Ga ago as 1.6 mGy/a. This value is higher or at least in the same order of magnitude than all surface dose rates of our highest, considered pressure level.

As already described, SEP-induced radiation environments were not analysed for this work, but can constitute a further contributor to the surface radiation environment for the present-day, thin atmosphere. As calculated by *Simonsen and Nealy* [1993], a large SPE yields a cumulative absorbed surface dose of up to 20 mGy during its tenure. As mentioned in Ch. 2.1.1, the occurrence rate of SPEs strongly depends on the Solar cycle, with high rates during maximum activity and lower rates during minimum, resulting in highly different annual surface dose rate contributions over the cycle. As for this research explicit annual dose rates of a certain year are not necessarily of great interest, even an averaged annual dose rate over the whole Solar cycle is sufficient to estimate the influence of SPEs. The findings from *Dartnell et al.* [2007A] suggest a cumulative surface dose rate of 40 - 50 mGy/a for SEP fluxes averaged over the whole Solar cycle. Due to their relatively low energy (compared to GCRs) SEPs can not penetrate particularly deep into the soil, being stopped in the first 10 to 20 cm [*Dartnell et al.*, 2007A]. For Noachian pressure conditions, this low penetration depth of SEPs would lead to a significantly smaller subsurface dose, due to the much greater atmospheric shielding, as well as the presence of the global magnetic field. Furthermore, as it is also not entirely ascertained how occurrence rates and particle fluxes would change for early-Sun conditions, no estimation on a contribution to the Noachian radiation environment will be given here.

The last contribution for which an estimation will be mentioned, is the influence of heavier GCR ions ($Z > 2$) not momentarily considered in the presented model. As shown in App. A.4, we find an average additional contribution to the GCR-induced surface dose rate of about 5 % for high pressure levels and $\sim$ 8 % for present-day conditions, where the presented approach is less reliable. Note that these values do not present dose rates directly from HZE ions, but rather the dose rate induced from the primaries and their secondary particle cascade.

This leads us to the estimated total surface dose rates presented in Table 6.1. Note

Table 6.1.: Estimated total surface dose rates in mGy/a for present-day and high pressure-level conditions. Considered are the GCR-proton- and -alpha-induced surface dose rates as presented in Ch. 5.1, the additional induced surface dose by the GCR-HZE component (App. A.4), and estimated SEP and natural background radioactivity contributions. The *'s denote values found by other research (references in the text).

	Present-day	High pressure level
Modelled GCR dose rate	$\sim$ 160 - 175	$\sim$ 0.06 - 3.1
HZE contribution	$\sim$ 13.5	$\sim$ 0.02 - 0.15
SEP contribution*	$\sim$ 45	–
Background radioactivity*	$\sim$ 0.4	$\sim$ 1.6
Estimated total dose rate	219 - 234	$\sim$ 1.68 - 4.85

that for the high pressure scenario, due to the lack of representable reference values no SEP contribution was included.

6.2. Implications for possible survival of simple life forms

As described in Ch. 2.2.2, there are known terrestrial bacteria with high radiation resistances. *D. radiodurans* can withstand irradiation of up to 3000 Gy without any significant loss of viability [*Baumstark-Khan and Facius*, 2001]. It has a D_{37} value of 6000 Gy, meaning the dose required for the organism to lose its CFA and, thus, considered to be inactivated. By going from the values given in Table 6.1, one can see that neither the estimated Noachian nor the present-day radiation environment would have a limiting effect on this type of bacteria.

It is p that *D. radiodurans* withstands the radiation-induced DNA damages by highly efficient repair mechanisms and a high level of adaptability to avoid the effects of DNA strand breaks [*Cox and Battista*, 2005]. However, such repair mechanisms can only be made use of in active organisms. Under the present-day cold environment on Mars, though, it is highly likely that any life form will be found in a dormant state, in which the repair and reproduction mechanisms are laid to rest [*Dartnell et al.*, 2007A].

Considering that due to the lack of protection against UV radiation, on present-day Mars the conditions at the surface are considered to be highly hazardous and detrimental to life forms, the chances for sustainment of life seem to be higher deeper beneath this hazardous near-surface layer. Table 6.2 shows subsurface dose rates (in mGy/a) for a dry regolith and in a permafrost-containing soil, with the values given

in the table derived similar to the ones in Table 6.1. The dose rates are presented, exemplarily, for depth of 2 m and 5 m, where the effects of UV surface ionisation are diminished. Note that, in the table, no values for SEP contribution are given, as these

Table 6.2.: Estimated total subsurface dose rates in mGy/a at depths of 2 and 5 m for present-day conditions. Shown are the same contributions to the dose as explained in Table 6.1. The * denotes values found by other research (references in the text).

	Dry soil		Permafrost	
	2 m	5 m	2 m	5 m
Modelled GCR dose rate	$\sim$ 20 - 23	$\sim$ 0.9 - 1.1	$\sim$ 21 - 28	$\sim$ 1.3 - 1.6
HZE contribution	$\sim$ 1.6 - 1.8	$\sim$ 0.07 - 0.09	$\sim$ 1.7 - 2.3	$\sim$ 0.1 - 0.13
SEP contribution	–	–	–	–
Background radioactivity*	$\sim$ 0.4	$\sim$ 0.4	$\sim$ 0.4	$\sim$ 0.4
Estimated total dose rate	$\sim$ 22 - 25.2	$\sim$ 1.4 - 1.6	$\sim$ 23.1 - 30.7	$\sim$ 1.8 - 2.1

particles do not propagate that deep. The natural background activity is assumed with the same value as for the present-day surface.

To, now, evaluate the implications for a sustainment of possible life, an approach common in this research field is pursued. Taking into account the dose rates from Tables 6.1 and 6.2, it is calculated how long bacteria would endure this exposure before loss of viability [*Baumstark-Khan and Facius*, 2001],[*Dartnell et al.*, 2007A],[*Mileikowsky et al.*, 2000]. These survival times can be derived by the following process:

It is postulated that simple life on Mars emerged some time during the Noachian period, when conditions were more favourable. Furthermore, it is assumed that these life forms were sustained in a dormant form, as at the end of the Noachian the Martian climate and atmosphere evolved into the cold, barren state found in present times. With the dose rates given above, the amount of time that is needed to inactivate these life forms is calculated for dormant bacteria at the surface, in 2 m and 5 m depth in dry regolith, and in 2 m and 5 m depth in a permafrost-containing soil. Here, the time of inactivation is determined as the time when the accumulated dose equals the D_{37} value of the respective bacteria. For this determination, the atmospheric density (i.e. the pressure level) is assumed as the present-day value. This is done because the progression of the atmospheric evolution is, as of now, not exactly established, but research suggest that the atmospheric loss happened on a comparably short time scale [*Jakosky and Phillips*, 2001]. Accordingly, the GCR-induced radiation and the additional HZE contribution are considered as constant over time. For each soil depth the corresponding mean value of the dose rate ranges shown in Tables 6.1 and 6.2

is taken. Note that the surface dose is considered to be the same for both dry and permafrost soils. The SEP-induced dose rate is estimated as an average 45 mGy/a for the surface and not considered for the subsurface layers. For the natural background radioactivity, a simple time-dependent evolutionary model is considered, starting at higher values in the beginning and decreasing with time to the presented day value. With the information provided in [*Mileikowsky et al.*, 2000] and the knowledge of the half lives of the considered radionuclides Th^{232}, U^{235}, U^{238}, and K^{40}, the progression of the background activity can be calculated by:

$$D_{t,Tot} = \sum_i D_{t,i} = \sum_i D_{0,i} \cdot e^{-\lambda_i \cdot (t-t_0)}, \tag{6.1}$$

where $D_{0,i}$ is the background dose rate of the given radionuclide for present day, $D_{t,i}$ its background dose rate at the time $t < t_0$, $D_{t,Tot}$ the total considered background dose at the time t, and λ_i the decay constant of the individual radionuclide, which is calculated from the half life $t_{1/2,i}$ of a radionuclide by:

$$\lambda_i = -\frac{ln(0.5)}{t_{1/2,i}}. \tag{6.2}$$

The survival times are calculated for two types of bacteria. The radiation-resistant *D. radiodurans* with a D_{37} value of 6000 Gy and the common bacterium *E. coli* (D_{37} = 3 Gy). The starting point for the survival time calculation was set to equal the assumed end of the Noachian period (3.7 Ga years ago).

With this approach, we derive the results shown in the top half of Table 6.3. It can be seen that due to their different D_{37} values the considered bacteria species show significantly different survival times. A dormant *D. radiodurans* could survive the Martian radiation conditions at the surface for $\sim$ 26000 years after the end of the Noachian. With increasing soil depth, this survival time would increase to $2.4 \cdot 10^5$ years (at 2 m depth), respectively $2.1 \cdot 10^6$ years (5 m), for a dry soil. In a water-ice-containing permafrost soil, these survival times would be shortened to $2.2 \cdot 10^5$, respectively $1.8 \cdot 10^6$ years, compared to the dry ground. The *E. coli* shows much shorter timescales. At the surface, a dormant form would be inactivated after $\sim$ 14 years, for subsurface layers the inactivation would occur after about 100 years (2 m), respectively roughly 1000 years (5 m).

This does not have to imply that there are no chances of finding bacterial life on present-day Mars. For one, the absorbed dose rates decreases with subsurface depth and, thus, for layers deeper-situated than the here analysed 5 m survival times of dormant organisms are expanded. Secondly, the timescales given here are calculated for bacteria that have been in dormant state during the whole time. If this dormant state is interrupted, the repair mechanisms against the damages induced by the radiation

Table 6.3.: Calculated survival times (in years) of the bacteria *D. radiodurans* and *E. coli* in dependence of subsurface depth. Shown for 0 m depth (at the surface), and for 2 m and 5 m subsurface depth in a dry regolith and a permafrost-containing ground. The top half of the table shows survival times from a starting point of 3.7 Ga ago. The bottom half shows survival times from years before present.

	Survival time (yrs) after end of Noachian (3.7 Ga ago)				
		Dry soil		Permafrost	
	0 m	2 m	5 m	2 m	5 m
D. radiodurans	$2.6 \cdot 10^4$	$2.4 \cdot 10^5$	$2.1 \cdot 10^6$	$2.2 \cdot 10^5$	$1.8 \cdot 10^6$
E. coli	14	123	1052	108	909
	Survival time (yrs) before present				
		Dry soil		Permafrost	
	0 m	2 m	5 m	2 m	5 m
D. radiodurans	$2.6 \cdot 10^4$	$2.5 \cdot 10^5$	$3.1 \cdot 10^6$	$2.2 \cdot 10^5$	$2.6 \cdot 10^6$
E. coli	14	128	1590	112	1084

and, as long as the population is not inactivated, reproduction of the organisms can set in, resulting in renewed survival times [*Mileikowsky et al.*, 2000].

Therefore, in order to determine how long the organisms are allowed to have been in a dormant state, so that active organisms could be still found today, a second set of calculations was conducted. Here, the survival time was calculated backwards, starting from present day. As the contribution of GCRs and SEPs to the dose were held constant, differences in the found survival times stem from the lower natural background activity. The results are shown in the bottom half of Table 6.3 and yield that *D. radiodurans* could have been dormant for up to $2.5 \cdot 10^5$ years if situated 2 m deep in dry soil, respectively $3.1 \cdot 10^6$ years in 5 m depth. For the surface, again a survival time of about 26000 years is calculated, which is nearly identical with the one found for the survival time after the Noachian, as for the total surface dose the influence of the natural background radioactivity is negligible.

As a conclusion, it can be stated that, considering the GCRs influence, the Noachian radiation environment would in all likelihood not have been prohibitive for an emergence of life, in particular when considering the known high radiation resistances of some terrestrial bacteria. In dormant state, these organisms can withstand radiation conditions on Mars for millions of years, if resting appropriate subsurface depths. Dependent on the possibility of interim active metabolism phases, where DNA repair and reproduction can happen, it is quite possible that radiation-resistant bacteria would

have survived the radiation environment on Mars even notably longer.

7. Particle Measurements with MSL/RAD

In chapters 4 and 5 a model capable to estimate the present-day, GCR-induced radiation environment on the Martian surface and the resulting findings were described. Furthermore, an approach to evaluate this model via comparison with other findings was presented. However, a problem when dealing with Martian radiation is that, as of today, there exist no measurements of the surface radiation environment on Mars. If at all, there is only data from dose measurements in the Martian orbit available (see Ch. 5.1.1). Therefore, the described approach can only help to test whether the model yields results that are in accordance with other simulation models. From the comparison, no conclusion can be drawn if the used model produces results that comply with the "real" radiation conditions on Mars. This, of course, can only be achieved via comparison with actual measurements conducted on the Martian surface.

However, it is to be expected that the radiation environment in the Martian atmosphere and on ground should differ, mainly because of the downward-directed secondary particle cascades created by the interaction of GCRs and atmospheric molecules. To give further insight on this topic, Fig. 7.1 shows simulated proton and neutron fluxes at the top of the atmosphere and on the surface, calculated with `PLANETOCOSMICS`. Although the overall proton flux for both conditions is similar, the simulations predicts differences in the spectral shape. For high energies the atmospheric flux is dominant, for energies below $\sim$ 150 MeV the proton flux at the surface is higher. The neutron fluxes show more pronounced differences. One can see that, while both cases show a similar spectral shape, the surface flux is always higher than the top-atmospheric flux. This is due to the fact that at the surface the spectrum is made up both of neutrons created in the soil, as well as in the atmosphere. At the top of the atmosphere, one nearly exclusively finds backscattered neutrons that propagate upwards from deeper in the atmosphere or the soil.

All said, the above mentioned orbital measurements are not sufficient to provide information on the surface radiation exposure, and at the moment the best way to make estimations on this subject, e.g. make predictions for possible hazards for future manned Mars missions, is to use MC particle transport codes, such as `PLANETOCOSMICS`. The problem here is that results from these simulations can only be as good as the theoretical model behind the code. Due to its nature, such a code has to make use of

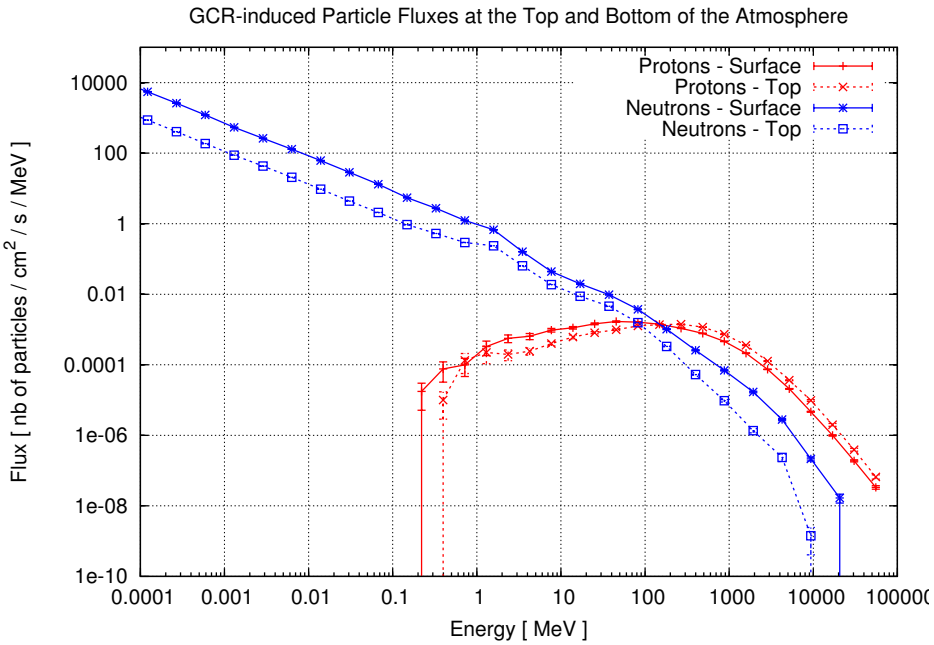

Figure 7.1.: Omnidirectional proton (red) and neutron (blue) fluxes induced by GCR protons and alpha particles, at the surface (solid) and the top of the Martian atmosphere (dashed), as calculated with `PLANETOCOSMICS`. The bottom of the atmosphere is set as the datum altitude.

several theoretical models and, to some degree, idealised assumptions about the micro- and macroscopic conditions on Mars. Having data from actual measurements available could therefore have bilateral advantage. On one hand, the simulation models can aid in verifying the measured data, on the other hand, these measurements would be essential for a verification of the theoretical transport codes.

Therefore, a Martian lander mission conducting in-situ measurements on the surface is of crucial scientific value for researchers dealing with this subject. An instrument, especially designed to measure the Martian surface radiation, was recently launched to Mars onboard the Mars Science Laboratory (MSL) mission by NASA. According to schedule, the surface measurements will begin in August 2012. The instrument in question is the aforementioned Radiation Assessment Detector (RAD), which was partially developed at the University of Kiel.

In this chapter, building the second main part of this thesis, the work undertaken to calibrate RAD's functionality for measuring charged particles is described. An accurate calibration is necessary to be able to derive reasonable conclusions from the measured data. Due to the limited telemetry with which data can be sent back to Earth, RAD

does a certain amount of data pre-processing onboard, so that the size of the data packages is reduced, before being transmitted to Earth. E.g., for charged particles measured events are coordinated in two types of 2-d histograms, one representing particles classified as having stopped in the instrument, the other particles that penetrated it. This, however, has the disadvantage that, for example, not every detector read-out is available for a later data analysis. Therefore, it is of great importance that the on-board data processing is as accurate as possible.

In the next sections, first, the process of creating the on-board size-reduced data products is explained. Then, the model developed to calibrate the on-board processing logic is introduced and results are given. Furthermore, a MC-simulation model of RAD is introduced, and it is explained how findings from these simulations are applied to the calibration of the RAD particle detection logic.

7.1. Particle detection with RAD

In the following, a description of how RAD is set up to measure charged and neutral particles will be given, as well as how a distinction of different particle types will be attempted. For a better understanding of the RAD detector nomenclature, a more detailed description of this can be found in appendix B.1.

7.1.1. Neutral particle detection

As the work in this thesis lays the emphasis on RAD's behaviour for charged particle detection, the behaviour for neutral particle detection will only be briefly touched. However, there is research available that describes this topic elaborately, for more insight refer to [*Köhler*, 2012] or [*Kortmann*, 2010].

As shown, the neutral particle contribution to the radiation environment on the Martian surface is significant. The two contributing species are gamma-rays and neutrons. To measure these neutral particles RAD is equipped with two scintillators, denoted D and E. Besides from being able to measure charged particle energy deposits, they are also sensitive to neutral particles and further allow for a separation between gammas and neutrons due to their different sensitivities to them. While the CsI scintillator D is highly responsive to gamma-rays, the hydrogen-rich plastic scintillator E is more sensitive to neutrons.

To distinguish neutral particles depositing energy in the scintillators from charged particles, the Anti-Coincidence (AC) is used. Charged particles have a high interaction probability with all the detectors in the instrument. Therefore, a charged particle depositing energy in, for example, D should have also made a signal in one or more of

the surrounding detectors beforehand, e.g. in F1 or in the Solid-State Detector (SSD) telescope. Consequently, signals detected only in D or E, but not in the AC channels, stem with a high likelihood from neutral particles (gammas or neutrons respectively, depending on the scintillator).

However, evaluating these neutral particle measurements can be problematic. Whereas the energy deposit of stopping charged particles in RAD's detectors is rather straightforward, with the initial energy equalling the deposited energy, the situation for neutral particles is way more complicated. The energy deposit of stopping neutral particles is randomly distributed, theoretically with a maximum possible value at their initial energy. This makes drawing reasonable conclusions on the initial neutral spectrum from the measured data hard to accomplish. So, to analyse neutral particles more elaborate methods are needed. *Köhler et al.* [2011] describe the efforts undertaken to solve this problem for RAD.

7.1.2. Charged particle detection

In a reasonable assumption, energetic charged particles found at the Martian surface originate mostly from the upper half-space, e.g. at high energies the charged particle field will be mostly made up of primary GCR particles that propagated through the atmosphere to the ground (compare Sec. 5.1.1 and in particular figures 5.1 and 5.2, as well as *Janitzek* [2010]). Therefore, the SSDs A, B, and C form a telescope for charged particle detection with a field-of-view that is upward- or zenith-directed.

As mentioned above, the bandwidth to send data back to Earth is limited. To reduce the amount of data, registered events are pre-processed by the instrument's electronics. E.g., certain parts of the data are arranged into pre-defined histograms, so that the energy deposits in each detector do not have to be stored separately and only the histograms are sent back. However, for some events, it is still interesting to have this additional information available, e.g. if a HZE ion hits the detector. Therefore, the recorded data is divided into two classes: High Priority (HP) and Low Priority (LP). Events assigned as HP are stored – if the free memory space of the electronics allows it at that moment – with the whole set of Pulse Height Analysis (PHA) words. A PHA word contains the whole set of stored data for a single event, e.g. containing the energy deposits in each detector. As such HP events should occur rather rarely the additional amount of data stored should not be too large. LP-assigned events (that are much more frequent) are stored only in their onboard-processed form. To give an estimate, the boundary between LP and HP particles is chosen as relativistic carbon, meaning ions species from C on upwards shall be assigned HP and species with $Z \leq 6$ LP, at least such particles with relativistic energies. Lower-energetic, low-Z particles are also

placed in HP as they lose more energy in the SSD telescope.

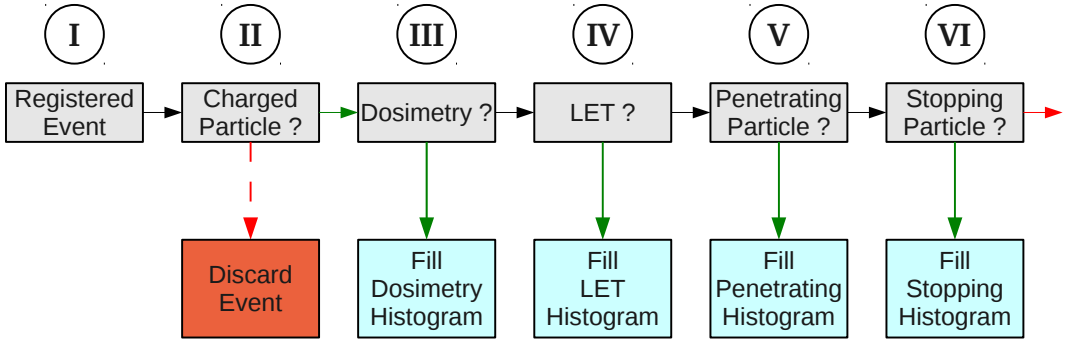

Figure 7.2.: Sequence of the RAD charged particle processing logic, starting with any registered event. Black arrows represent the order of processing checks, a green arrow indicates a successful check, a red arrow a negative result that leads to a discarding of the event. LP and HP events follow the same processing flow. Note that the arrow from II to III is also coloured green, because in this step events can be rejected absolutely from the following steps and, therefore, a successful passing is necessary.

The process flow of analysing charged particles is illustrated in figure 7.2 and described in the following (with the Roman numerals corresponding to the ones seen in the figure):

I. The instrument is triggered and starts the processing logic.

II. Is the event a charged particle? Here, it is checked if the event deposited significant energy in both A (A1 or A2) and B, otherwise it is discarded from the following steps. This logic is further used to distinguish between HP and LP particles. This can be done as higher-charged particle species deposit more energy in the A and B detectors than lower-charged ones with comparable energies per nucleon. The logic first checks if a HP assignment is warranted, and the remaining events are then checked if they qualify as LP charged particles, where the logic also looks for a significantly small energy deposit in the AC C2. These assignments are carried over for the rest of the processing chain.

III. Is the energy deposit in B or E high enough to warrant the recording of dosimetry spectra? If so, the event is recorded in the dosimetry histogram of B, respectively E. There are two histograms each for B and E. One shows number of counts (in B or E) versus time, the other number of counts vs energy deposit. This check does not use the priority assignment distinction.

IV. Is the energy deposit in A (here, the A1 or A2 is used depending on which detector recorded the higher energy deposit) significant and does the event deposit roughly the same energies in A and B? If $E_{Dep,A} \approx E_{Dep,B}$, this indicates that the particle has penetrated both A and B and therefore the minimum of the track length x in one detector is known ($x \geq d_{SSD}$, where d_{SSD} is the thickness of the SSD detectors). This is important for the LET calculation. If the check is successful the event is registered in the corresponding LET histogram. These histograms are arranged as number of entries vs energy deposit in B (one histogram each for A1 and A2).

V. Can the event be considered as a penetrating particle? These are particles that traverse through the whole detector head, depositing energy in each detector, as well as in the AC scintillator F2. As for the different priorities the processing sequences differ, the checks for these logics are described further below in more detail.

VI. Is the event a stopping particle? Particles that are not classified as penetrating are checked for the possibility of having stopped in one of the detectors (B–E). In general, a check for stopping particles is needed, as otherwise, particles, not classified as penetrating, could still exit the detector via F1. Again, the HP and LP checks differ significantly from each other. Therefore, they are also discussed separately further below.

A complete list of all analysed logic checks and derived cut values can be found in table C.1.

As mentioned above, the classification of penetrating and stopping particles differs significantly for HP and LP events. While the LP classification can be, rather simply, done via checking of certain detector trigger thresholds, for HP this method is not that reliable. E.g., when depositing energy in a detector high energetic HZE particles can cause significant cross-talk in an adjacent detector, especially in the AC detectors C2 and F. This can also lead to triggering of detectors, i.e. create a signal above the trigger threshold, even when they are not directly hit by a particle. Due to this, simple cuts, respectively thresholds, can not be used, and comparative cut conditions between two (or more) detectors are needed.

Penetrating particle logic

To classify whether an event can be considered as a penetrating particle, i.e. the incident particle deposits energy in all detectors and still has enough remaining energy to propagate further, one has to first ensure that this particle had a proper flight path through the sensorhead. The idea here is to mark a charged particle as penetrating

when it traverses through the whole sensorhead coming from the upper half-space, i.e. entering in A2 (A1 is not considered in this case for geometrical reasons) and leaving after passage of F2. Due to the processing sequence, it is already ascertained that the particle deposited a certain amount of energy in A and B (charged particle trigger).

Furthermore, for LP, it was also already checked if the deposit in C2 is small enough (via a threshold). As cross-talk effects in F1 are negligible for LP particles, a check for this AC detector is made redundant by the following checks. I.e., if the energy deposit in the remaining detectors is significant, F1 should see no significant energy. Note that the AC F2 is also considered as a nominal detector for this purpose.

For the HP events, the above described logic becomes a bit more complicated but follows the same logical chain. First, the particle telescope is checked. Particles with enough energy to penetrate all detectors can be assumed to deposit nearly the same amount of energy in each of the SSDs, as the path length through each thin detector is relatively small and the particles are so high-energetic that they do not lose significant amounts of energy in the SSDs. In an ideal case (straight, perpendicular passage through each detector) the energy loss here would then be:

$$\mathrm{E_{Dep,single}} = \frac{1}{3} \cdot \mathrm{E_{Dep,ABC}}, \tag{7.1}$$

with $\mathrm{E_{Dep,single}}$ being the energy loss in one single SSD and $\mathrm{E_{Dep,ABC}}$ the total energy loss in the telescope. Due to electronic noise, non-perpendicular flight paths, etc. this factor might be a bit lower in real measurements. However, to assure a proper penetration of the SSDs the logic compares the energy deposits in A, B, and C against the sum of the deposits of the three. Nominally, this sum is also checked against C2 to discard particles that traversed it. However, as a result of this research, this cut was changed to a total energy check in C2, as explained further in Sec. 7.2. The sum of the energy deposits in the SSDs constitutes a solid measure of energy. I.e., it can be derived more simple and definite than compared to the scintillators, where quenching or uncertainties in the light output measure make an absolute energy determination harder. Therefore, this sum is further used as a comparison for the other detectors of interest (D, E, F2), so that one ends up with seven comparison checks in total. An adjustment for the ABC vs F2 check has also been added as the result of this work (see Sec. 7.2).

Penetrating histogram

The data for penetrating particles are stored in a 2-d histogram containing the number of counts over the sum of the energy deposit in A2+B+C versus the energy deposit in detector E divided by the sum in A2+B+C. Both, HP and LP events, are stored in the same histogram for this purpose. One challenge when analysing penetrating particles

is that RAD has no measure of their total energy (as, due to their nature, they do not lose their total energy in the detectors). However, as will be described in the following, this histogram setup still allows to separate different ion species, and also enables to make rough assumptions of the energy of these penetrating particles.

The x-axis (energy deposit in the telescope) allows for a separation of ion species. Here, the energy deposit for high-energetic, penetrating particles, is dependent of the charge Z of the particle. The penetrating particles further can be roughly divided into two groups: particles with such high energies that they do not lose significant energy even when passing the scintillator crystals, and particles that are energetic enough to penetrate the whole detector but lose a significant portion of energy in the scintillator. For the first group the ratio of energy deposit in E versus the energy deposit in the telescope is nearly constant independent of ion species, similar to the ratio of energy losses in one of the SSDs compared to the whole telescope. The particles belonging to the second group, however, have a higher ratio, as they deposit proportionally more energy in the scintillators. Therefore, the y-axis allows to distinguish between these two groups as they will be stored in different bins.

However, the above mentioned, theoretical considerations neglect the so-called quenching effect. Charged particles traversing the plastic scintillators or the crystal produce light which is detected by photodiodes. Their signals are read-out for a determination of the energy deposited in these detectors. Now, the light production unfortunately is not a linear process. In regions where high LET occurs, i.e. regions with high ionisation density, there is a higher probability of radiationless deexcitation processes, yielding a comparably lower light output. Therefore, the determined total energy loss of particles stopping in D or E does not correspond one-to-one to the particle's actual energy. In the penetrating histogram, this leads to particles with high dE/dx in detector E to have lower y-values (ratio of E/ABC). Fig. 7.3 shows a sketch of how the penetrating histogram would look like. High-energetic particles, independent of ion species lie on a line parallel to the x-axis, having the same ratio of deposits for E and ABC (red line). The points on the line indicate the positions of the different ion species (higher charged species lie at higher x-values). Furthermore, the effect of quenching is also sketched (dashed blue line). The higher the charge of the ion species, the larger the decrease in the E/ABC-ratio gets.

Stopping particle logic

After the electronics processes a registered event for classification as a penetrating particle, any remaining, rejected events are checked if they represent stopping particles. Again, the logic for LP events is less complicated. As the particle should be stopped in

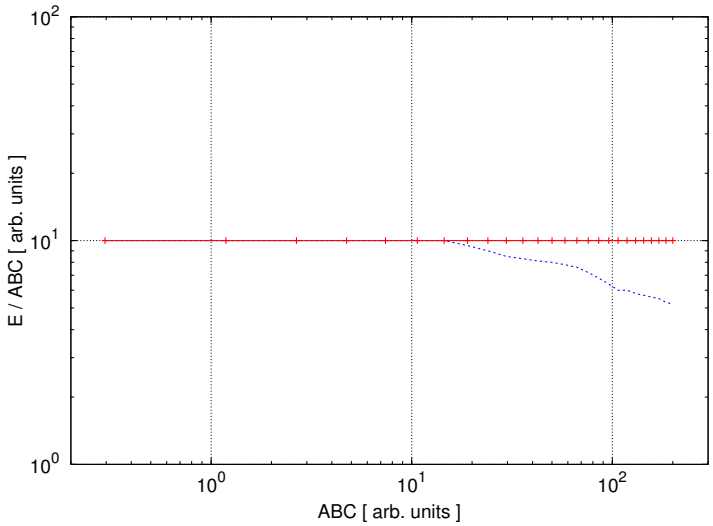

Figure 7.3.: Sketch of the penetrating particle histogram. The red line shows high-energetic penetrating particles, all with the same ratio of deposits in E and ABC. The red points further indicate positions of different ion species (with increasing Z for increasing x-values). The dashed blue lines depicts the effect of quenching that gets stronger for higher-charged particles. Note that the units on the axes are arbitrary.

one of the detectors B, C, D, or E, here, only the AC needs to be checked further. So, it is tested if the deposit in F1 and F2 is below a determined threshold. No comparative check is needed as cross-talk can be neglected for LP particles.

For HP events, the processing logic becomes more convoluted, as not only the validity of every flight path is checked, but further in which detector the particle might have stopped. A flow chart of this process is shown in Fig. 7.4. The individual steps are discussed below, with the Roman numerals referencing the ones shown in the figure:

I. AC check. The sum of the energy deposit in the telescope (here, A means either A1 or A2, whichever is higher) is compared to the AC detectors C2 and F2. After analysing the calibration data, the F1 check was removed from this step because of its previously mentioned saturation by high-LET particles.

II. The energy in C is compared to the SSD sum. This is to test if the particle reached C (penetrating it or stopping in it).

III. If the check in II. is negative, i.e. the particle did not deposit sufficient energy in C, it is tested if D does register a significant deposit. If that is not the case, the particle can be considered as having stopped in B.

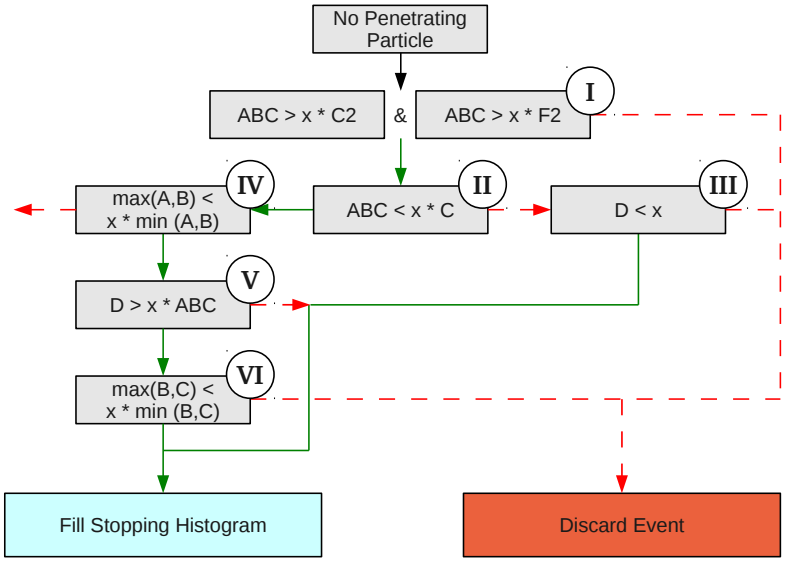

Figure 7.4.: The processing sequence for identifying HP stopping particle events. Green arrows indicate a successful check, red negative results leading to a rejection of the event. The checks are given in the grey boxes with energy values in certain detectors denoted by the specific detector name (e.g., ABC stands for the deposit in the SSD telescope) The "x"s refer to a specific cut value for each check. Note that the red arrow at box IV should also lead to the "Discard Event" box. Furthermore, the red arrow at box V signifies a negative check. However, these rejected events are also considered as stopping (explained in more detail in the text) and, therefore, the red arrow joins with the green line.

IV. This check is done to test if particles with significant energy in C have nearly the same ratio in A and B, as they should have penetrated both to reach C. As the read-out segment of B is a bit smaller than that of A2 and C, it might be possible for particles to hit A2 and C, but not directly B. As B could have still been triggered by cross-talk, these events would be rejected by this cut.

V. The energy loss in D is compared to that of the telescope to see if the particle reached D. If the deposit in D is low compared to ABC, this means the particle stopped in C and the rejected events are thus also valid.

VI. As D has seen significant energy, that means the particle should have penetrated the telescope and deposited similar energies in A, B, and C. Therefore, the ratio

of B and C is tested as a consistency check, similar to IV. A positive check means these particles then should have stopped in D or E (as a comparably low deposit in the bottom AC F2 was tested under I.)

Stopping histogram

To store the data for stopping particles, RAD makes use of a so-called "dE/dx-vs-E-method", where dE/dx means the specific energy loss of a particle in a certain length of matter, and E signifies the total energy of the particle.

According to *Goulding and Harvey* [1975] the energy loss of a charged particle in a detector can be given by a simplified version of the Bethe-Bloch-equation (Eq. 2.1), as:

$$\frac{dE}{dx} = \frac{a \cdot Z^2 \cdot c^2}{v^2} ln[\frac{b \cdot v^2}{c^2 - v^2}], \tag{7.2}$$

where Z is the atomic mass number of the particle, v its velocity, c the velocity of light, and a and b are constants depending on the detector material. As we are looking at stopping particles, i.e. non-relativistic particles, their energy can be given by $E = \frac{1}{2} \cdot M \cdot v^2$, respectively the square of the velocity by $v^2 = \frac{2 \cdot E}{M}$. Furthermore, the logarithmic term in Eq. 7.2 can be neglected, as it only changes slowly with varying energy in this case. This leads to a further simplification of the Bethe-Bloch-formula:

$$\frac{dE}{dx} \sim \frac{M \cdot Z^2}{E}. \tag{7.3}$$

As according to Eq. 7.3, the energy loss dE/dx of a particle is proportional to the inverse of the particle's total energy E, plotting dE/dx versus E in a double-logarithmic scale for different stopping ion species would lead to the following scenario:

- Particles of the same ion species (with the same M and Z) lie on the same line with the slope of -1 (due to the double-logarithmic scale).
- Different ion species are separated from another by their differences in M and Z^2.

As one can see, such a "dE/dx-versus-E"-plot therefore enables to distinguish between different ion species, considering stopping particles, i.e. particles that deposit their total energy in the detectors.

RAD now uses a variation of this method, also called "Goulding-method". Instead of storing the data in a "dE/dx-vs-E"-histogram, this method uses a transformation of the coordinates of these axes. For a more well-arranged histogram the y-axis here looks as follows: Instead of dE/dx, the y-axis is constructed as dE/dx · E. As multiplying Eq. 7.3 with the total energy E leads to:

$$\frac{dE}{dx} \cdot E \sim M \cdot Z^2, \tag{7.4}$$

the y-value now is only proportional to the specific ion species parameters mass and charge, meaning that all particles of the same species will lie on a line parallel to the x-axis. Again, this method leads to a separation of the different species. In general, the x-axis would not have to be changed, simply keeping it as the expression of total energy. However, different ion species will have different stopping energies in RAD, i.e. higher-Z ions are stopped at higher energies. Keeping the x-axis as total energy would therefore lead to different minimum and maximum x-values for measured stopping particles for different ion species. By transforming the x-axis into the expression $\frac{\mathrm{E}}{\mathrm{dE/dx}}$, higher-Z ions will be shifted more to the lower x-values than lower-Z ions of the same energy/nuc, as in connection with Eq. 7.3 this transformation leads to:

$$\frac{E}{\frac{dE}{dx}} \sim \frac{E^2}{M \cdot Z^2}. \tag{7.5}$$

The minimum possible x-value then of course will be 1 (particles stopping in detector A, as $(\mathrm{dE/dx})_{\mathrm{detA}} = \mathrm{E}$ independent of ion species). This yields a more conform arrangement of the x-values which is important for the binning of the stopping histogram. Fig. 7.5 shows a sketch of the resulting stopping histogram. In the plot, one

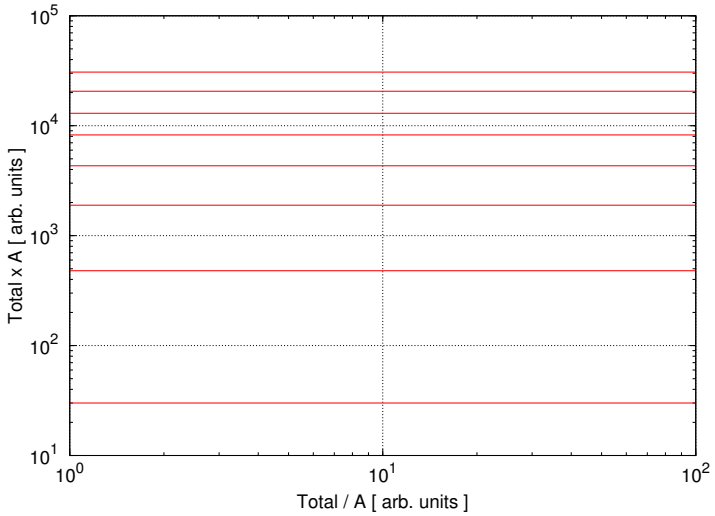

Figure 7.5.: Sketch of the stopping particle histogram. Sketched with the red lines are stopping particles of ion species with charge 1 (protons) to 8 (carbon), with protons lying on the lowest line. Note that the units on the axes are arbitrary.

can see that particles of one particular ion species would lie on one line parallel to the x-axis. Furthermore, one can see that the ion species are separated from each other and that these separation spaces decrease in the logarithmic scale for higher charges of the species (higher charges equal higher y-values).

Quenching also plays a role for the stopping histogram setup. The effect is strongest for particles stopping early in either D or E, as then these particles have a high LET in the quenching material. As a result, the theoretically calculated lines parallel to the x-axis for particles of the same ion species decline from high x-values (particles with high energies) to low x-values, where particles stopping shallow in D (or E) are situated. However, with a sufficient number of bins for both x- and y-axis, the quenching problem should not pose to big a problem for the on-ground data analysis, as one should still be able to assign the different bins to different ion species and energies.

7.2. Calibration of RAD with charged particle beams

If a particle interacts with one of the detectors, the pulse height of the resulting signal is converted into a digital value by the instrument's electronics. Now, each detector has several so-called gain channels available. For each individual channel, the pulse height of the signal is amplified differently and then the resulting digitized value is stored. As these digital values have a limited range, which is the same for all gain channels, different channels have therefore different resolvable energy ranges and, correspondingly, different energy resolutions. These are given in App. B.2.

The digital values themselves can give a relative estimate of the amount of energy deposited by an interaction, as higher values correspond to higher deposits. However, from this no information about the absolute value of the energy deposit can be gained. To achieve this, these digital values have to be calibrated to a corresponding real energy value. This is done with the help of well-known particle-emitting sources, i.e. sources emitting particles of a known energy. For the calibration of RAD, several different measurement campaigns were conducted, so that a broad coverage of energies and particle species was achieved. A list of these measurement campaigns is given in Table B.3 in App. B.3.

Besides from the absolute energy calibration and intercalibration of the different detector gain channels, these calibration data can also be used to determine values necessary for the particle detection logics described in Sec. 7.1. The latter builds the main part of work that was conducted for RAD in the scope of this thesis.

7.2.1. Modelling the onboard processing logic

To calibrate RAD's behaviour for charged particle detection, a model was developed that mirrors the logic, described in Sec. 7.1.2, used by the instrument. To determine the wanted thresholds or ratio values, the code allows to either look at the raw channel entries in a given data set or calibrates the channel entries belonging to one detector

into a total energy value. For a quick overview, this energy determination works in the following way:

As already mentioned, each detector is read-out in multiple channels with different amplifications of the detected signal to give the detector a broad measurement range. A list of these available gain channels and the measurement range for each detector is given in Table B.2. Now, if a channel is either in underflow (i.e. the measured signal is in the range of the noise) or overflow (the measured signal is greater than the available measurement range of this channel), this channel is discarded. The remaining channels are – applied with different weighting factors – then used to determine the energy value of the signal. A more elaborate description of this process can be found in [*Böttcher*, 2011] and the work undertaken to determine the necessary calibration factors in [*Kuhnke*, 2011], from which the values used in this model were taken.

Some of the logic checks simply compare the digital signal value with a certain threshold for this check, e.g. placing a cut above the noise peak. The means to derive the needed values for these cuts is to create histograms of the digital signals in the respective detector channels and place the cuts at the appropriate signal number. As this thesis places its focus on the more elaborate and convoluted HP penetrating and stopping particle cuts, the analysis of the simpler cuts is not presented here, but, for the sake of completion, can be found in App. C.1. E.g., the HP and LP charged particle and LET trigger, and the LP penetrating and stopping particle cuts are such simpler checks.

The cut or ratio values for the HP classification of penetrating and stopping particles are mainly derived in a manual, iterative process. E.g., the penetrating particle logic uses seven cuts in coincidence condition, meaning all conditions must be met at the same time, or:

$$r_{pos} = \prod_{i=1}^{N} a_i, \tag{7.6}$$

where N is the number of cut conditions, i $\in$ N, and a_i stands for the corresponding cut condition. Here, $a_i = 1$ denotes a successful check, respectively 0 a negative check, and a resulting $r_{pos} = 1$ means an event is classified as a penetrating particle. Starting with initial guesses for all cut values, which can be estimated by analysing the un-cut data or through logical considerations for certain cuts, the process is to remove one of the conditions from the check, leading to:

$$r'_{pos} = \prod_{i=1}^{N'} a_i, \tag{7.7}$$

with N' containing the number of remaining conditions. By analysing accepted and rejected events for the left-out cut condition, an adjustment to the initial value of this

condition can be applied, and the cut is reinserted in the model. In the next step, a different cut is removed and analysed, until all conditions are dealt with. Starting with the new set of derived cut values, this procedure is repeated until no further adjustments to the cut values are deemed to be necessary.

7.2.2. Determining cut values for the particle processing logic

This section presents results for the analysis of the HP penetrating and stopping particle logic, as well as the resulting histogram plots.

Cut value determination for penetrating particle histograms

As an example, the left plot of Fig. 7.6 shows a plot of the ABC vs C2 cut for the following conditions: Only events recognised as HP charged particles are regarded, all cuts except the C2 check are applied with initial guesses.

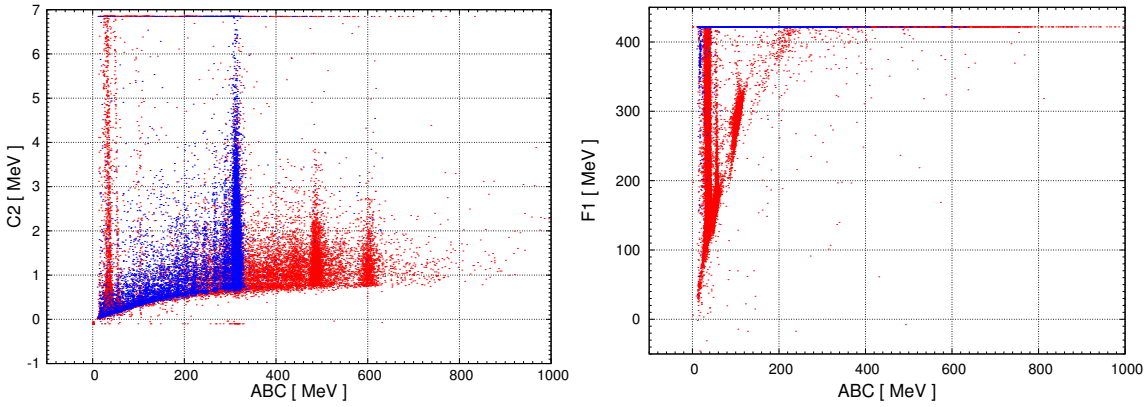

Figure 7.6.: Left: Calibrated energy deposits in A2+B+C vs C2. Right: Calibrated energy deposits in A2+B+C vs F1. Plotted for HP charged particles with all other penetrating particle cuts applied. The red dots show events rejected by any of these remaining cuts, the blue dots the events that pass all cuts.

By colour-coding events that pass all applied cuts (plotted in blue in the figures) and events that are rejected by at least one of the cuts (red), one can now investigate how to adjust the initial guess of the left-out cut condition to an improved value. However, this plot is furthermore shown for multiple reasons. Nominally, this AC check would be handled as shown in the figure by comparing the deposits in ABC and C2. But, as can be seen, there are no clear tendencies discernible regarding the behaviour of penetrating and non-penetrating events, most blue dots are found in areas where there are also rejected, red ones. In addition, cross-talk can also be observed. Normally,

one would expect that the main particle population would have $E_{Dep,\,C2} \sim 0$ MeV as a lower limit. But due to cross-talk this lower limit increases for greater deposits in ABC. Another interesting point are the clearly visible particle populations parallel to the y-axis. They are caused by knock-on electrons or delta-rays scattering back in C2.

The main point derived from this plot is, that there are some events, depositing energy in the overflow in C2, that are not rejected by the other cuts. Therefore, the AC check has to reject them as they represent unwanted particle tracks through C2. This results in the previously mentioned conclusion that instead of a comparative check of ABC and C2, rather an overflow check of C2 is sensible, i.e. it will be only checked if the energy deposit in C2 is below the overflow value.

In the right plot of Fig. 7.6, the deposit in ABC versus the deposit in the AC F1 is shown, also for all HP charged particle events, with all other seven cuts applied. One can see that applying a further cut with this condition does not make much sense. The initial, theoretical idea of the AC check is to only allow particles with near to zero energy deposit in the detector to pass the cut. However, nearly all events recognized as penetrating by the other cuts are sitting in the overflow of F1 and there are further no events with $E_{Dep,\,F1} \sim 0$ MeV found, as high-energetic particles saturate F1, most probably via knock-on electrons, even when not hitting it directly. Thus, the ABC vs F1 cut was removed from the processing logic.

As stated above all penetrating cuts are applied in coincidence condition. However, there is one slight exception: The ABC vs C2 cut is checked before the other cuts, meaning only particles passing this cut are further processed – with the remaining six cuts then being checked simultaneously. To illustrate this, in figure 7.7 a comparison between all available events and the remaining events that pass the C2 cut is shown, for the subsequent condition of a ABC vs A check.

The remaining cut conditions are shown in their final iterative stage in Fig. 7.8. Again, each plot shows the result when excluding that particular cut from the process. As can be seen, the ABC vs A/B/C cuts all show similar behaviour and the main amount of events are situated on lines with a slope of $\sim \frac{1}{3}$ in accordance with Eq. 7.1. As one can find a few events arranged around these lines, the cut conditions here are chosen a bit lower than the slope of $\frac{1}{3}$ would suggest, with the idea to also include these smeared-out events.

Finding a cut for the ABC vs D check (mid-right panel of Fig. 7.8) is also rather straightforward. Here, one wants to exclude the "blue" events at D $\approx$ 0 MeV, as they are not rejected otherwise and, of course, they should not be carried over. On a sidenote, one can also clearly see the different ion species created by fragmentation processes before entering the instrument. At a closer look, the main blue line is divided into single populations, representing different species. This partition is even better

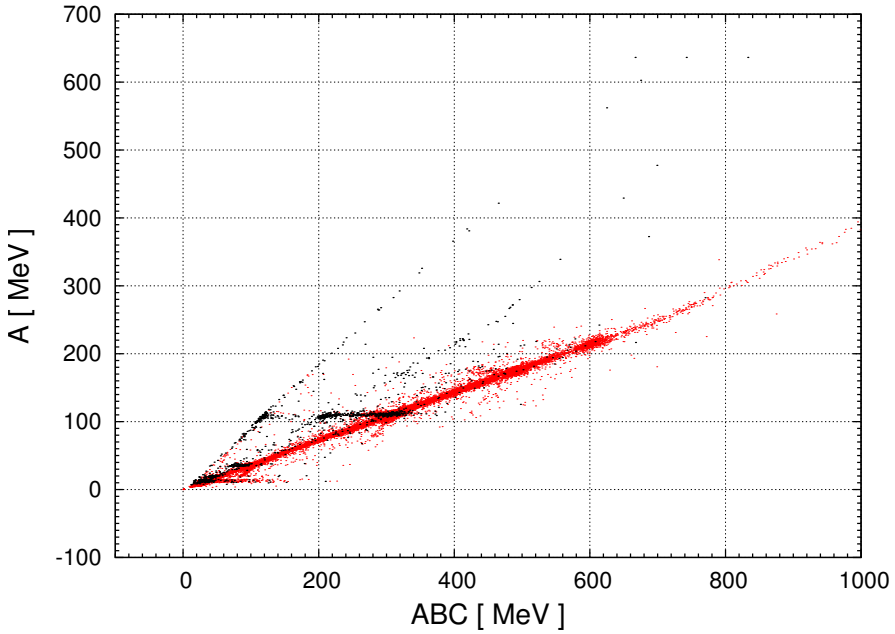

Figure 7.7.: Calibrated energy deposits in A2+B+C vs A2 for all HP charged particle events. Events rejected by the prior ABC vs C2 cut, which therefore are not carried over to this processing step, are plotted in black. Events passing the ABC vs C2 cut are shown in red.

observable in the ABC vs E plot (bottom left panel). Another interesting population here is the one parallel to the y-axis at $E_{Dep,\,ABC} \sim 320$ MeV. This line stems from the process of, in this case, Fe-ions that pass through ABC and D, undergoing fragmentation in E and creating ion species with lower Z that then deposit less energy in E. Although this line looks rather distinct in this scatter plot, compared to the number of Fe-ions not fragmented, their amount is rather low and, so, it is not that important to adjust the cut to include this parallel line. Thus, it is mainly important to ensure that the particle population on the diagonal blue line is accepted by the cut. It also should not be set at a too low ratio, meaning that E should really see comparably more energy than the telescope, yielding the observable compromising cut condition.

The ABC vs F2 cut (bottom right panel of Fig. 7.8) mainly has to reject the blue dots at F2 $\approx$ 0 MeV and to make sure that any blue dot in the overflow is accepted. The latter is achieved with an additional total energy cut adjusted to the energy value of the overflow. For clarity, this cut condition is not shown in the plot. Analysing the data in the figure, one could assume that this condition would be sufficient. However, depending on the energy calibration used, it can happen that the events in the population parallel to the y-axis at ABC $\sim$ 25-35 MeV are not rejected by the other cuts (this has mostly

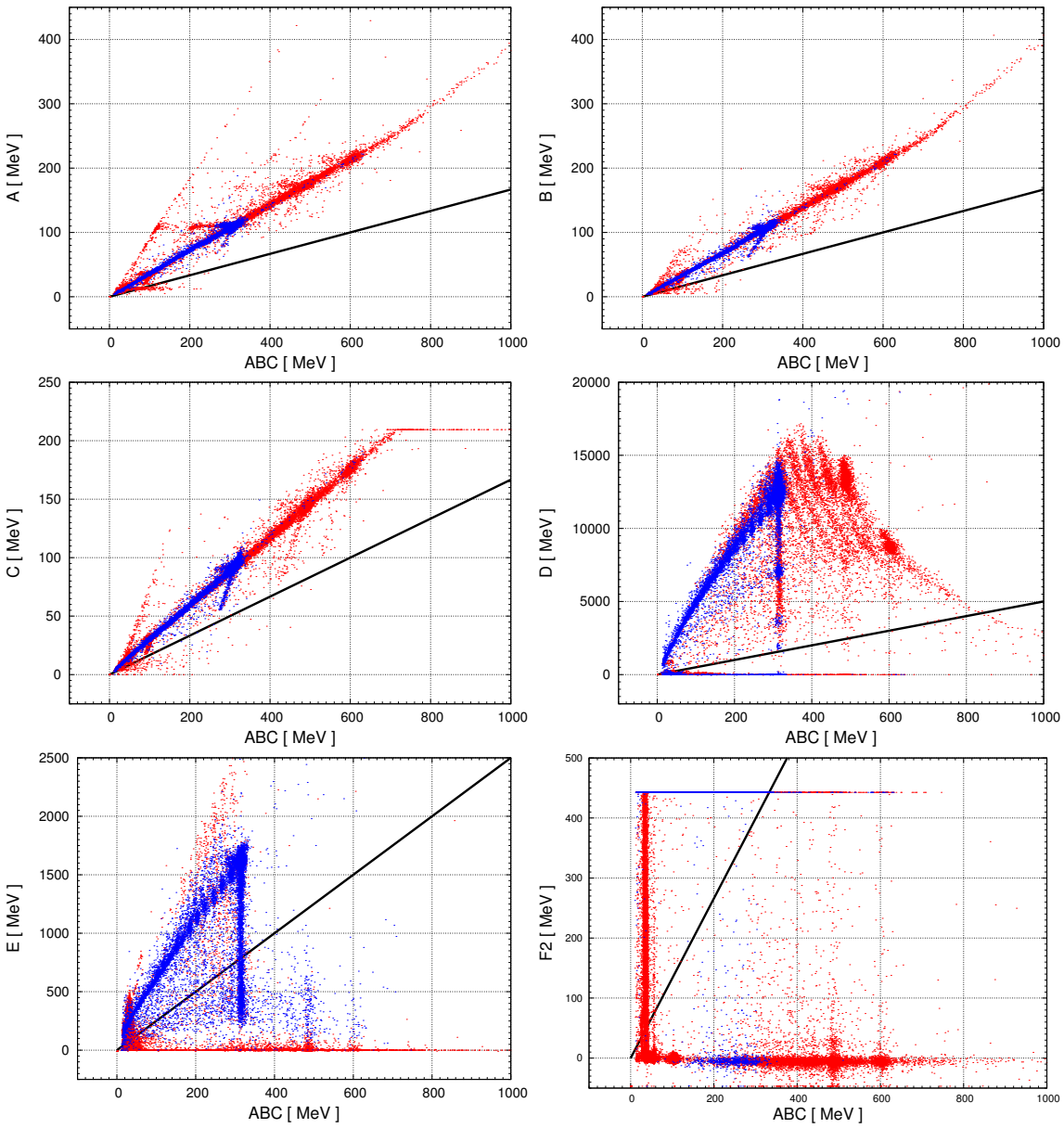

Figure 7.8.: Cut conditions for HP charged particle events. Plotted in blue are events passing all cuts, with the one analysed in the plot excluded from the cut conditions. Red dots represent events rejected by the logic. The black lines show the respective determined cut conditions, which, however, is not used in the shown plot. Top left: ABCvA, top right: ABCvB, mid left: ABCvC, mid right: ABCvD, bottom left: ABCvE, bottom right: ABCvF2.

to do with the quality of the energy calibration in D). As it can not be excluded that these particles might still have a significant energy deposit in D, the cut is set to allow them to pass.

As mentioned above, a list of all derived cut values can be found in Tab. C.1 in App. C.3. Now, applying these cuts to the calibration data and plotting it in the corresponding penetrating particle arrangement, yields the plot shown in figure 7.9. Here both, events classified as LP and HP, are shown. Over the x-axis the different

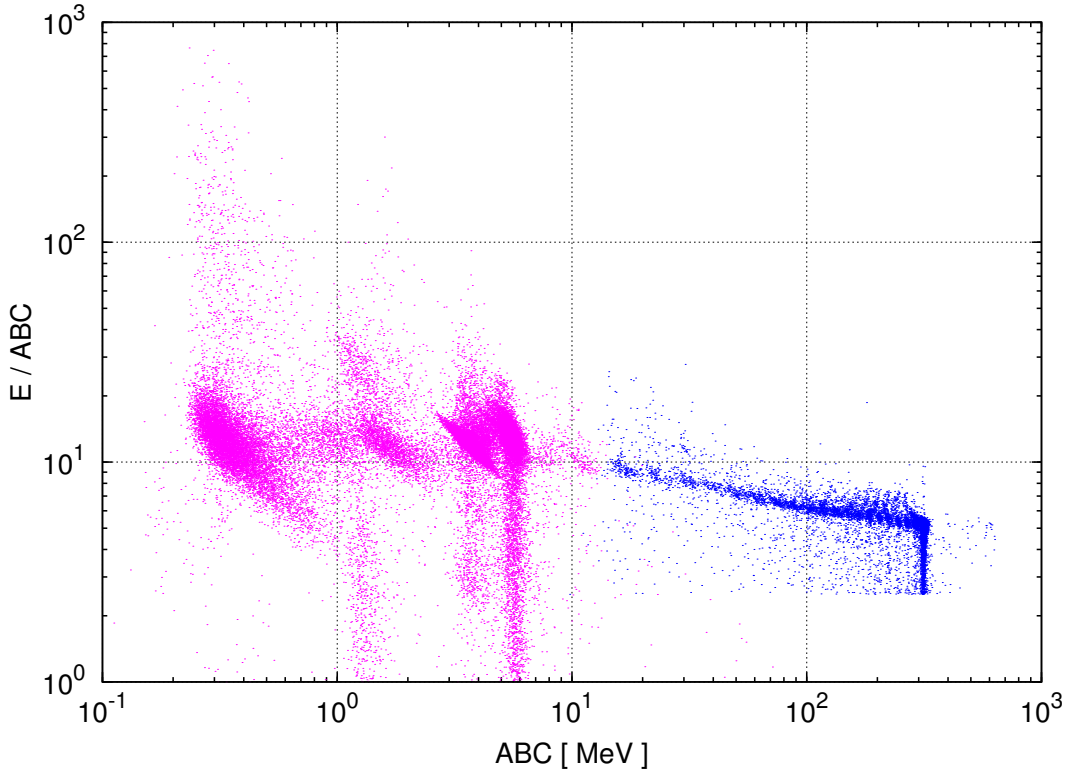

Figure 7.9.: The resulting penetrating particle histogram (E/ABC vs ABC) of the used calibration runs for particles passing the penetrating particle logics. HP events are plotted in blue, LP events in magenta.

ion species are recognisable. Interestingly, the theoretically predicted line parallel to the x-axis for high-energetic penetrating particles (see Sec. 7.1.2) shows a decrease for higher energy deposits in ABC, which is due to quenching, as the light output in E is lowered. However, this effect is braced against by a proper allocation of the available bins of the histogram.

Further, one can also see for the LP data, particles that penetrate the instrument but lose significant energy in D and E (the populations with E/ABC ratios greater than $\sim$ 10-15). The lines parallel to the y-axis at low E/ABC ratio values come from particles

that fragment in D or E. But again, their significance is overstated by the scatter plot, in a 2-d histogram these events have much lower counts than the normal penetrating particle populations.

Cut value determination for stopping histograms

HP events that are rejected by the penetrating particle logics are then tested with the stopping particle checks. First, the AC is checked. The starting point, here, is to check against C2 and the sum of deposits in F1 and F2, to only allow particles with paths inside the AC boundaries to be tested further. However, as already seen in the penetrating particle processing, F1 is quickly saturated when high-energetic particles interact with D and E. A check of the deposits of ABC and F1, therefore, leads to a situation similar to the one shown in the right plot of Fig. 7.6, resulting in a likewise exclusion of F1 from the cut logic, while the two remaining AC detectors are still checked.

These checks are presented in Fig. 7.10. Note, that in the following plots, whenever

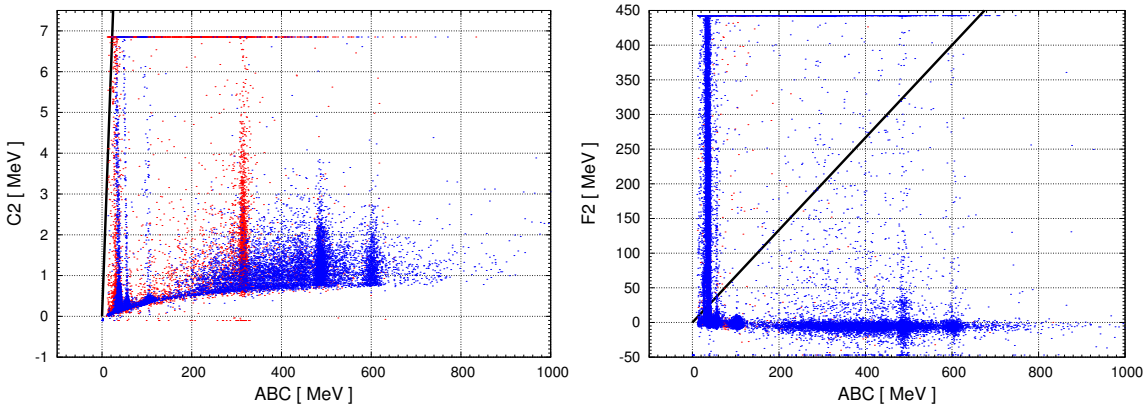

Figure 7.10.: Left: Calibrated energy deposits in A2+B+C vs C2. Right: Calibrated energy deposits in A2+B+C vs F2. Plotted for HP charged particles with all other stopping particle cuts applied. The red dots show events rejected by any of these cuts, the blue dots the events that pass all remaining cuts.

detector A or the sum of energy deposits in the telescope ABC is mentioned, this refers to detector segment A2. The cut processing for A1 works in the same way and, therefore, these plots are not shown here. For the C2 check one can see that the populations of particles passing the other cuts are not distinguished from the ones rejected, except for a small area at very low ABC deposits. Therefore, a rather steep cut adjusted to the most left blue line parallel to the y-axis is chosen.

Analysing the right plot of Fig. 7.10, yields the importance of the F2 check, as without this check nearly all events are passed by the other cuts. Here, it is important to reject all particles with significantly higher deposits in F2 than in ABC. One could further argue for an additional check against a F2 overflow, but the number of events in overflow not caught by the presented cut is negligibly low.

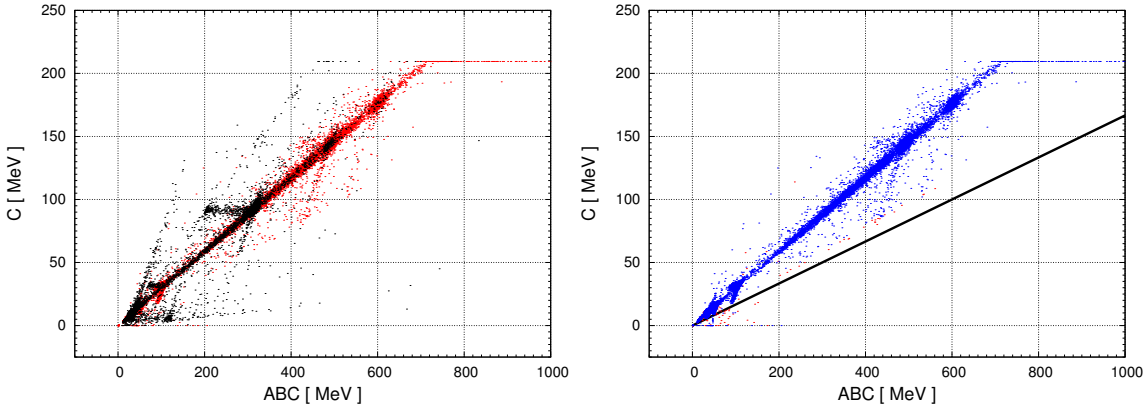

Figure 7.11.: Calibrated energy deposits in A2+B+C vs C. Left: Particles entering this cut are plotted in red, particles rejected by the prior AC checks and not entering this cut condition are shown in black. Right: Plotted for HP charged particles with all other stopping particle cuts (besides from cut IV in Fig. 7.4) applied. The red dots show events rejected by any of these cuts, the blue dots the events that pass all remaining cuts.

In the left plot of Fig. 7.11, the influence of the AC checks on the further processing is shown, highlighting all events (black) that are rejected by these cuts and not further processed. The right plot shows the ABC vs C cut in its iterative stage. Note, that besides from this cut, the conditional total energy check in D (position IV in Fig. 7.4) is also omitted from the cut logic for this plot.

In the top left plot of Fig. 7.12, this cut is further examined. Particles that are rejected by the ABC vs C cut are checked for their deposit in D, as these could represent particles stopping in B. The resulting total energy cut should be placed right (i.e. at a higher energy) of the noise peak. To be able to accommodate for a possible broader noise peak, the cut is set directly before the onset of the peak seen to the right and results in a cut value of 5 MeV.

The top right panel of Fig. 7.12 shows the consistency check of detectors A and B for particles passing the ABC vs C cut. This cut checks if the deposits in A and B are nearly the same, as at this point only particles penetrating these detectors should be processed. Due to electronic noise, non-perpendicular flight paths of the particles,

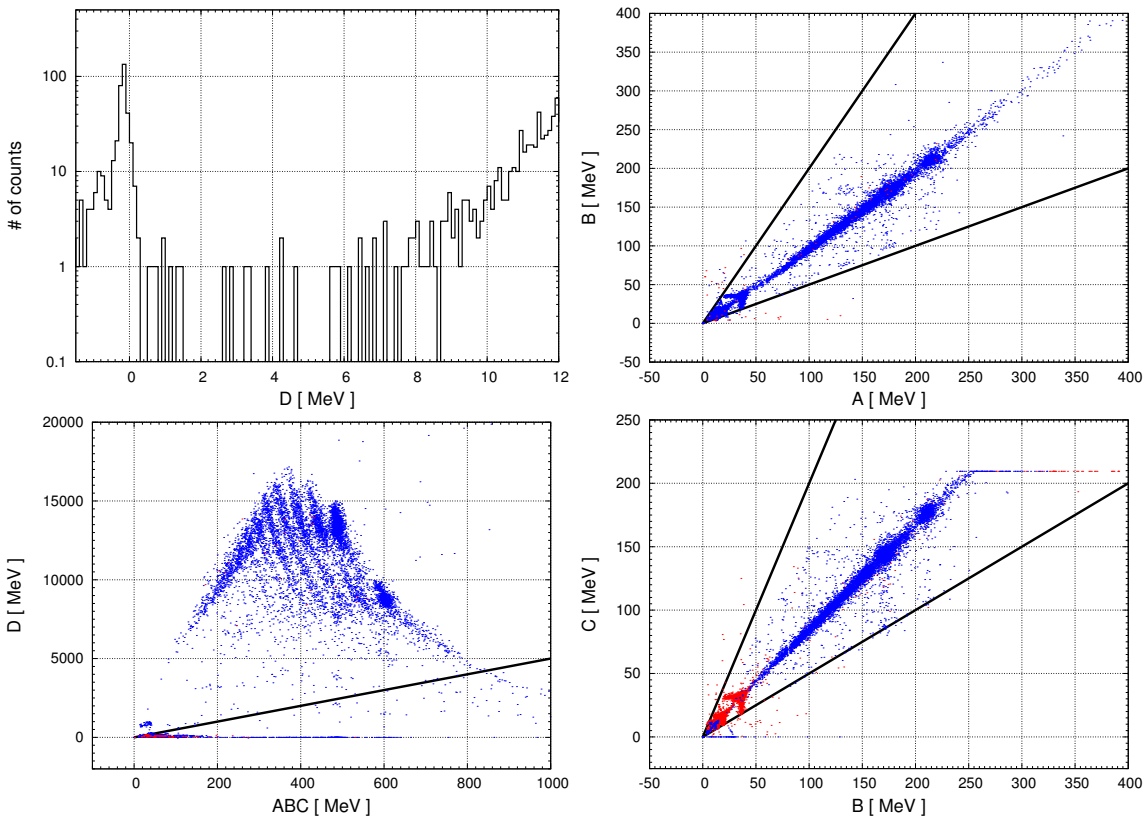

Figure 7.12.: Top left: Total energy check in D for particles rejected by the ABC vs C cut. Histogram of number of counts per detected energy deposit in D, only the relevant range of the x-axis is shown. Top right: A vs B consistency check, bottom left: ABC vs D, bottom right: B vs C consistency check. Cut conditions for HP charged particle events. Plotted in blue are events passing all cuts, with the one analysed in the plot excluded from the cut conditions. Red dots represent events rejected by the logic, the black line show the respective determined cut conditions. Only events not rejected in any prior processing step are shown.

measurement uncertainties, etc., these deposits are not exactly the same, so that the cut is placed in a bit wider range. Note, that the number of red dots in these plots (progressing from the plots shown in Fig. 7.10 to the ones in Fig. 7.12) decreases. This is of course due to the fact that only events that passed all the prior cuts are further processed at any stage.

The bottom left panel of Fig. 7.12 shows the ABC vs D cut. Here, it has to be mentioned that events rejected by this cut are, in the complete logic, also accounted for as stopping particles, as these events should only be particles stopping in C. Therefore, one can observe a blue particle population below the cut line. The cut is mainly there to assure that the particles with comparably high energy deposit in D are allowed to pass. The cut will reject a small amount of particles at really high ABC energy deposit values, but this is a compromise to be made when wanting to cut-off the whole population at D $\sim$ 0 MeV.

In the bottom right panel one can see the last consistency check of B vs C, which shows very similar characteristics to the plot shown in the top right panel. Here, the larger red population inside the cuts is shown as rejected, because the condition, that events rejected by the ABC vs D cut are also considered as stopping, is left out for redundancy reasons, i.e. otherwise there would be no possibility for rejected particles at this last stage.

The resulting stopping histogram for the calibration runs can be seen in Fig. 7.13, again HP, as well as LP data is shown. In the population at high y-values (marked as 1 in the plot), one can nicely see the separation of different ion species, created by fragmentation of Fe-ions before entering the detectorhead. Furthermore, in this region of the plot the quenching effect is also visible, as these different populations do not lie on lines parallel to the x-axis but show a decreasing slope to lower x-values. One can also notice the switch from HP to LP in the helium population (denoted position 3 in the plot). This is due to the fact that the boundary is set at $\sim$ 4 MeV (in A and B) to properly classify relativistic carbon. However, stopping helium can also deposit more than 4 MeV in A, B and C, so these particles are assigned HP. As one can see in the smooth continuation of HP and LP helium, He is still recognisable in the final histogram.

Unfortunately, the presented data is not as clean as expected, especially visible in the smeared out dots of the LP data (position 4) and the discontinuities of the HP data at position 2. This, however, is not founded in the particle processing logic or its implementation presented in this work. It has, most likely, either to do with problems in the measurement process during the actual calibration runs, or with a flawed energy calibration of the data from these runs. The latter is a well-known problem and work to fix this is ongoing, but at the moment not completely finished. But again, as mentioned

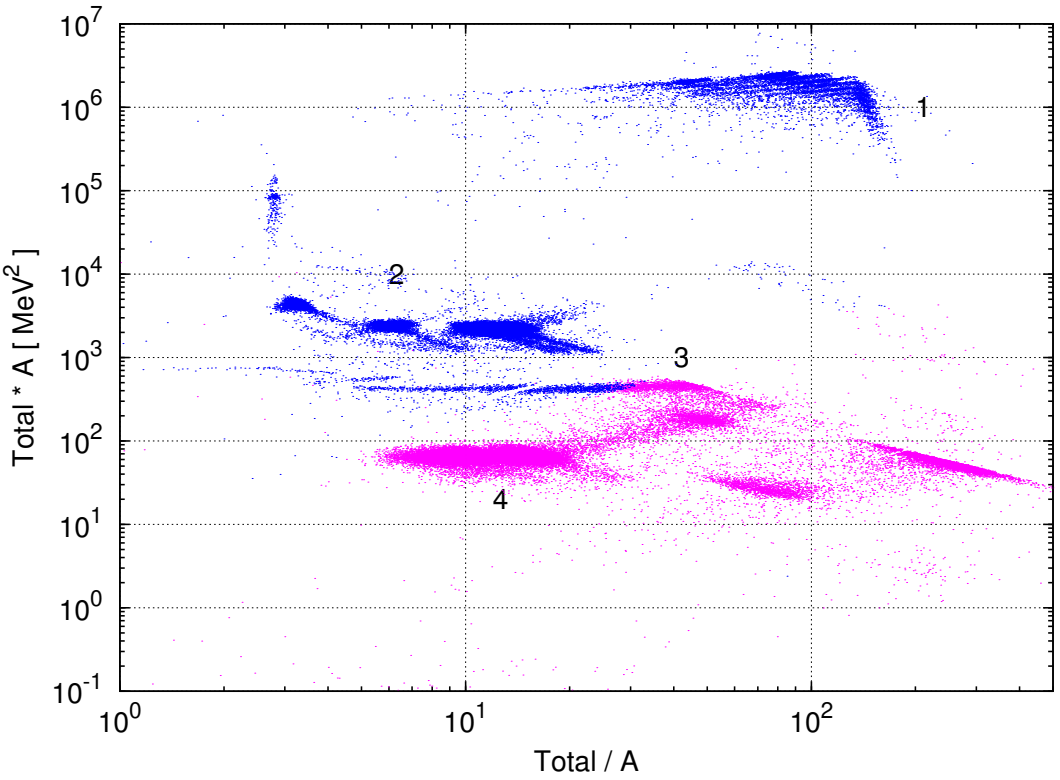

Figure 7.13.: The resulting stopping particle histogram for events with higher deposits in A2 than A1. HP events are plotted in blue, LP events in magenta. Plotted is the total energy deposit (A2+B+C+D+E) / A2 versus the total energy deposit times A2. The numbers 1-4 denote particle populations discussed further in the text.

before, the processing logic seems to work fine.

7.3. Simulations with GEANT4

7.3.1. The GEANT4-RAD model

To date there are no data available for radiation measurements on the Martian surface. So, one has to use particle transport simulation codes to get an idea of what a detector would measure on such a surface mission. Furthermore, a solid simulation model of the detector can help in other matters, such as calibration and debugging of the measuring process. Fortunately, there is already such a model of RAD available. A full `GEANT4` model of the sensorhead was developed by Dr. O. Kortmann during his time as a PhD-Student at the University of Kiel, implementing a CAD model of the instrument by

L. Seimetz (also at the University of Kiel), and extended by J. Köhler as part of his PhD-thesis at the University of Kiel. In the scope of this work, this GEANT4 model of RAD was used to assist the analysis of calibration data (see Sec. 7.2.2) and to help evaluating the necessary binning of the on-board data storage histograms by determining theoretical positions of different ion species in the histograms for stopping and charged particles. Note that effects of quenching were not considered in the simulations conducted for this thesis, but the resulting effects will be mentioned in the next section.

7.3.2. Simulating charged particle beams

It has to be stated that for the simulation the classification of stopping or penetrating particles was not conducted by simulating the total RAD processing logic. Rather, absolute energy cuts for the different detectors were applied, as for the GEANT4 simulations the deposited energies in the detectors are, of course, readily available. Thus, this allows for a more precise analysis in this way. Fig. 7.14 shows the simulation results for penetrating and stopping particle histograms and further plots to better compare the simulations with the onboard logic, (e.g. Figs. 7.8 and 7.12), are shown in Fig. C.9 in App. C.2. At a first glance one can say that the positions of the known ion species from calibration runs, e.g. protons or helium, in the charged particle histograms match comparably well with their GEANT4-simulated positions. So, the simulations can help to fill in binning borders for other interesting ion species for which no calibration data was available.

In the simulation results for penetrating particles (top panel of Fig. 7.14), one can see the separation of the different ion species over the x-axis. Of course, for higher-Z particles the separation spaces get smaller in the logarithmic scale of the axis. However, as the aim of the corresponding measurement histograms will not be to distinguish between each and every one of the ion species, but rather between certain groups, this separation should be sufficient. The class of penetrating particles that lose significant energy in the scintillators before leaving the sensorhead can be seen in the upward-directed tails of the populations. Furthermore, when comparing the y-values (ratio of deposit in E and ABC) of the individual ion species shown in this plot with the ones shown in Fig. 7.9, one can see the effect quenching has on real measurements. Whereas the simulated y-values of high-energetic, penetrating particles are almost constant for all considered species (at $E_{Dep,E/ABC} \approx 10$), in the measurement data the higher the charge of the ions the lower the $\frac{E}{ABC}$ ratio gets due to quenching. However, as the y-binning of the onboard histograms is rather rough, consisting of just 3 bins (see Table 7.1), these discrepancies have no significant influence on using the simulation data as an aid to evaluate the measured calibration data, as unquenched and quenched

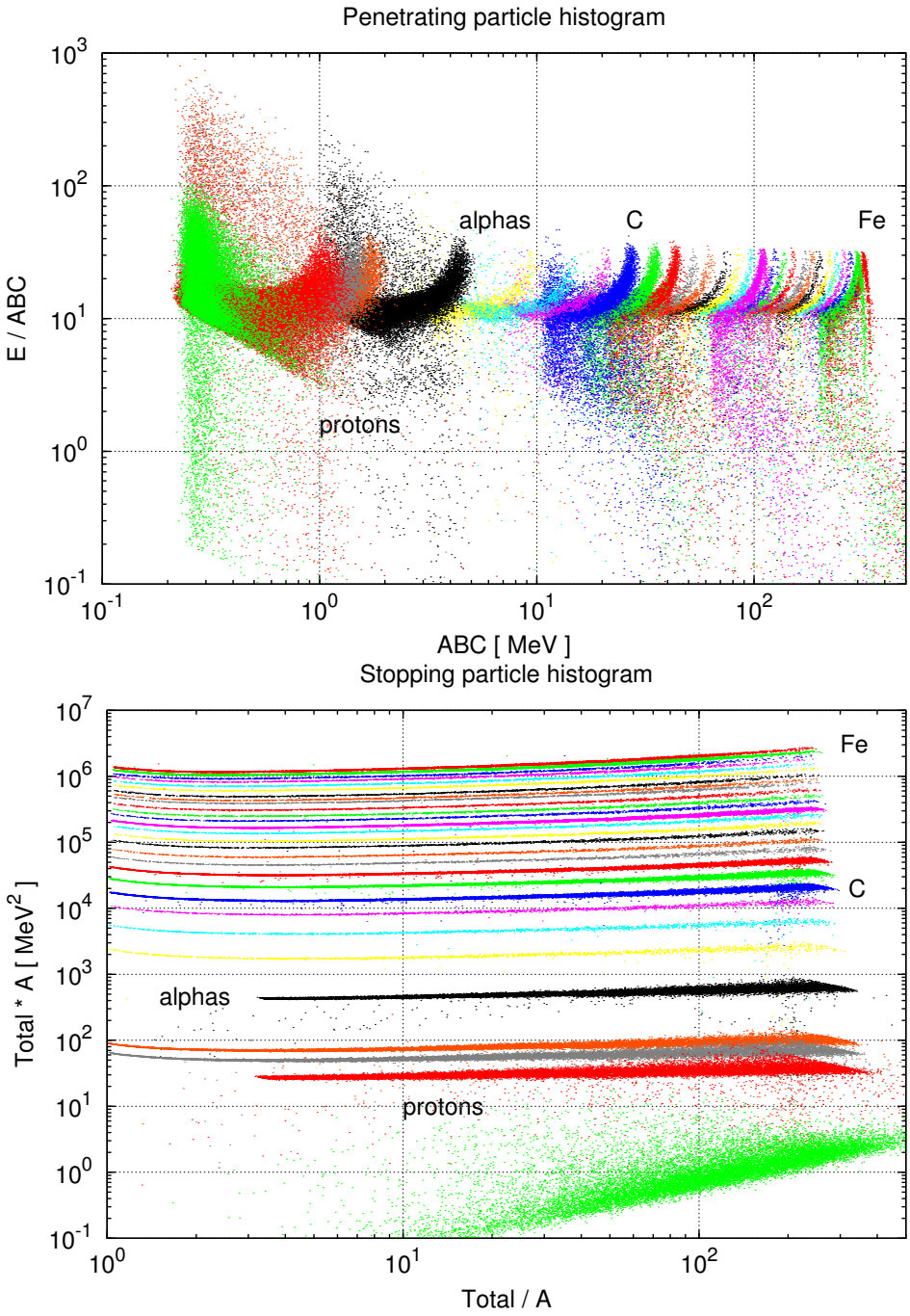

Figure 7.14.: GEANT4 simulation results. Plotted are results for several ion species from protons ranging up to Fe, as well as electrons (lowest, respectively leftmost green), deuterium, and tritium (between protons and alphas). The axes were chosen according to the corresponding particle histogram setup of the RAD onboard data storage. Top: Particles penetrating the detectors A, B, C, D, E, and F. Bottom: Particles stopping in one of the detectors B, C, D, or E. For reference some particle species positions were labelled: protons (red), alphas (black), carbon (blue), and iron (red).

$\frac{E}{ABC}$ ratios would be placed in the same bin. The x-values, meaning the energy deposit in the telescope, match up well, which is expected, as quenching plays no role in the thin Si-detectors.

Due to the limited amount of stopping ion species statistics, a comparison of the simulated stopping histogram (bottom panel of Fig. 7.14) with the measured data shown in Fig. 7.13 is quite hard. One can see, that the simulated helium y-axis positions (the labeled black population in the plot and denoted as position 3 in Fig. 7.13) match up well with the measurements. The limited amount of stopping proton statistics in the measurement data makes a conclusion a bit complicated, but it can be estimated that at least the y-positions match tolerably well with the `GEANT4` simulation (where protons are the lowest red population). For Fe (topmost red population in the simulation plot) a difference between the two plots is not really visible, and for carbon (the labelled blue population in the simulation plot), the simulated y-values are a bit higher, which could hint at quenching. However, as both axes-parameters are functions of total energy deposit (including the scintillators D and E, where quenching is likely to occur), as well as deposit in A2 (no significant quenching), the quenching can not be recognised as straight-forward as in the penetrating histogram.

Furthermore, it probably would be difficult to distinguish between different high-Z ion species, as these ions are bunched relatively close together. However, one can derive from the simulation that it should be possible to create a binning that separates the more important species from another, such as protons from helium, or helium from Li, Be, and B. This approach is deemed sufficient enough for a proper data analysis of the measured RAD data, as for HZE ions additional PHA data will most likely also be available.

As a conclusion of the results gathered from the `GEANT4` simulations Tables 7.1 (penetrating) and 7.2 (stopping) give an overview over the determined y-axis binning of the histograms. In each table, the y-axis bin number and the content of all corresponding

Table 7.1.: List of y-axis bins and their content for the penetrating particle histogram. The distinction in high- and lower-energetic penetrating particles is explained in more detail in Sec. 7.1.2.

y-bin	Content
1	Underflow bin – high-energetic penetrating particles
2	Lower-energetic penetrating particles
3	Lower-energetic penetrating particles – overflow bin

x-axis bins is given. Note, that no actual y-bin-values are presented, as the ultimate

Table 7.2.: List of y-axis bins and their content for the stopping particle histograms. The column "Content" shows which particle species can be found in the bins belonging to one specific y-axis bin.

y-bin	Content
1	Underflow bin
2	Electrons
3	protons, He
4	protons, He
5	protons, He
6	protons, He
7	protons, He
8	protons, He
9	He, Li, Be
10	B, C, N, O
11	F – Ca
12	Sc – overflow bin

definition of these values is still to be finalised.

The x-axis of the penetrating histogram is divided in 24 logarithmically-spaced bins ranging from an energy deposit in ABC of $\sim$ 0.1 MeV to $\sim$ 500 MeV. As these bin borders are being determined independently of this work, no more information on this topic can be given at the moment and the x-bins are not included in Table 7.1 (the same applies to the 16 logarithmically-spaced x-axis bins of the stopping histograms).

The y-binning shows two bins reserved for lower-energetic particles, as it was decided to be more reasonable to have a higher resolution for these particles. A second consideration, here, would be to reserve one bin for underflow, one for high-, and one for the lower-energetic penetrating particles (plus overflow).

As can be seen in Table 7.2, most y-axis bins of the stopping particle histograms list several particle species as their content. This is due to the facts that multiple x-axis bins belong to one y-bin, and that particle of one species do not necessarily lie on lines parallel to the x-axis. Therefore, a population of one particle type can cover a broader range of y-bins over the course of the x-axis.

As mentioned above, as higher-Z ions are bunched closer and closer together over the y-axis of the histogram, it would be difficult to allocate one y-axis bin to one or just a few ion species. Therefore, and because count rates for HZE ions are expected to be rather low, larger ranges of ion species are covered in single y-bins. The larger amount of

y-bins reserved for protons and helium comes from the consideration that these species should be most frequently measured, and so, the most meaningful physical analyses should be concerning these species. Therefore, a large number of bins was deemed reasonable.

8. Conclusions

In the first part of this thesis, the radiation environment on Mars was analysed for changes induced by atmospheric and surficial conditions differing from the present-day situation. The motivation of this analysis is that the Noachian-period Mars (4.1 - 3.7 billion years ago) looked decisively different from the cold, barren planet we know today. To analyse the early-Mars-like conditions, a model was developed to calculate the radiation exposure for a given Martian environment. Using MC methods, the model derives particle fluxes induced by GCR interactions with the planet, which subsequently allows to determine the absorbed dose rates caused by these particles. The model was tested by comparing calculations for present-day Martian conditions to findings from existing research, which yielded values in a satisfying level of agreement.

The developed model and the presented findings constitute a significant addition to the existing research on Martian radiation. Due to the setup of the model, calculated total dose rates can be split up into different subsets of contributing factors, so that, e.g., the contributions of different particle species to the total dose can be tracked in dependence of atmospheric or soil depth. This gives access to a highly-detailed level of information for any analysed environment and, thus, enables to provide analysis and data on a wide range and combination of influencing factors to the radiation environment.

One main difference between Mars, then and now, is that the Noachian atmosphere was considerably denser, although the exact magnitudes of atmospheric density and pressure level are not definitely assured, as of now. To account for this uncertainty, we analysed the changes in the radiation exposure for a stepwise increase of the overall atmospheric pressure level, to identify potential trends of this increase for the radiation dose. Our findings yielded that, as far as the dose induced by GCRs is concerned, absorbed surface dose rates for Noachian-like high atmospheric pressure levels were three to four orders of magnitude lower than today and would lie, depending on the assumed value of the Noachian surface pressure, up to one order of magnitude below the present-day average terrestrial surface dose rate at datum altitude. Furthermore, it was shown that the surface dose rates for a given pressure-level scenario show a strong dependence on the surface altitude, at which this dose occurs. The radiation environments were also analysed for their subsurface dose rate progressions, where an expected decline with

depth was found. For the modelling of the existence of liquid surface water or subsurface water ice, no significant influence on the surface dose could be detected. Beneath the surface the decrease of the dose rate was found to be less pronounced compared to a dry modelling of the ground, as due to the lesser density of the permafrost, compared to a water-less soil, incident radiation from the upper hemisphere can propagate deeper into the ground. The presented findings were, furthermore, brought into context with their astrobiological implications. We showed that the estimated radiation exposure for suggested Noachian conditions should not be considered constrictive for a possible emergence of life on early Mars. A simplified modelling of the temporal evolution of this exposure was used to estimate survival times for dormant bacteria at and beneath the surface. The results indicate a potential sustainment of life up into the millions of years, substantiating estimates from other research models.

Due to the large number of parameters necessary for a complete modelling of Noachian conditions, not all parameters could be analysed in the scope of this work. Therefore, it is expedient for further research on the presented topic to analyse the implications of the parametric changes not yet considered. Foremost, the implementation of the HZE portion of the incident GCR spectrum into the `PLANETOCOSMICS` code should be given priority. Although this might constitute a longer-lasting and elaborate task, the fact that the GCR input spectrum is a main driver for Martian radiation, a more accurate depiction of its composition should be worth the effort. Due to the high modifiability of `PLANETOCOSMICS`, an implementation of the remaining parameters can for the most part be easily achieved. The adaptability of the developed model further offers room for more research, e.g. analysing dose rates divided into contribution of backscattered and downwards-cascading particles.

In the second part of this thesis, a model to investigate RAD's onboard behaviour for classifying charged particles was developed. The model was coded to mirror this respective part of the RAD electronics' processing logic to evaluate RAD's accuracy of data processing. A high accuracy in correctly recognising measured particles as charged particles and to further distinguish them into penetrating and stopping particles is crucial for conducting Earth-based science with the measured data from Mars. Due to limited transmission bandwidth, the onboard charged-particle classification is necessary as RAD has to reduce the amount of gathered information from a measurement before transmitting the data back to Earth. The developed model was applied to calibration measurement data and the logic chain was investigated for each processing step. In the course of that research flaws in the existing logic were identified and corrected, and we used the findings from the model to change and improve the onboard processing logic. Additionally, the cut values for the processing logic were assessed and, if necessary, adjusted, and new cut values were determined for the newly implemented processing

steps. In the end, values for the y-axis bins of the onboard created histograms for charged particle measurements were determined. The values for this binning, important to achieve a reasonable resolution of different groups of ion species, were derived by complementing the information from the calibration data with simulations using a GEANT4 model of the RAD detectorhead, developed by O. Kortmann at the Universtiy of Kiel.

As there is only a limited amount of calibration data available, analysing in-flight data can contribute to further review and improve RAD's particle processing logic. As of this writing, the MSL mission is already well on its way to Mars. Fortunately, at the moment RAD is the only instrument already collecting data. Therefore, the amount of bandwidth is not so strictly limited during cruise, compared to the nominal surface operation of the rover. Thus, RAD can transmit larger amounts of unreduced data back to Earth, which makes a more detailed analysis of the particle processing possible. The conjunction of the processing-logic model, the RAD GEANT4 model, and PLANETOCOSMICS's ability to model modified Martian environments offers the unique possibility to simulate the expected radiation environment and estimate the RAD measurements in Gale crater beforehand.

Once arrived at Mars, RAD will conduct the first-ever measurements of radiation on the Martian surface. This will allow us to evaluate the dose-calculation model, developed for the first part of thesis, with dose measurements from RAD. Furthermore, the particle flux measurements can be compared to simulated Martian surface spectra derived from particle propagation models, such as PLANETOCOSMICS.

A. Further Results from the Dose Rate Model

A.1. Further absorbed dose rates

In this section further plots for the results presented in Ch. 5.1 can be found. Fig. A.1 shows the absorbed dose rates of gammas, electrons, and positrons, as well as the total absorbed dose rates (including all analysed particle species) in dependence of the surface altitude for different atmospheric pressure scenarios. These plots are separately shown here, as including these particle species in the respective "Absorbed dose rate contribution"-plots in Ch. 5.1 would have unnecessarily cramped the plots shown there. As mentioned before, all three particle-species curves show very similar characteristics to the neutron dose rates shown in Ch. 5.1, i.e. for present-day atmospheric conditions their dose rates increase with decreasing elevation, for higher pressure conditions they, then, decrease with the surface altitude. This is, in accordance with the effects described for neutrons in the respective sections, mostly due to the changes in the primary particle fluxes with higher pressure levels. The secondary particle creation of all three species shown here is strongly coupled to the primary particle fluxes, as the electromagnetic component of the particle cascade is for the most part started by the decay of π^0 into two gamma rays, as described in Ch. 2.1.1, and the π^0 itself is created in the hadronic cascade.

Table A.1.: Surface absorbed dose rates for gammas, electrons, and positrons for different atmospheric pressure levels. Given are the calculated minimum and maximum dose rates in mGy/a.

	Surface absorbed dose (mGy / a)		
	Gammas	Electrons	Positrons
Present-day	6.4 - 15	9.7 - 19.3	9.1 - 14.8
Pressure x 25	0.06 - 13.9	0.08 - 14.4	0.04 - 9.5
Pressure x 50	0.02 - 5	0.03 - 4.5	0.01 - 2.7
Pressure x 100	0.008 - 0.48	0.014 - 0.45	0.005 - 0.24

As a reference, the minimum and maximum values found for the three particle species

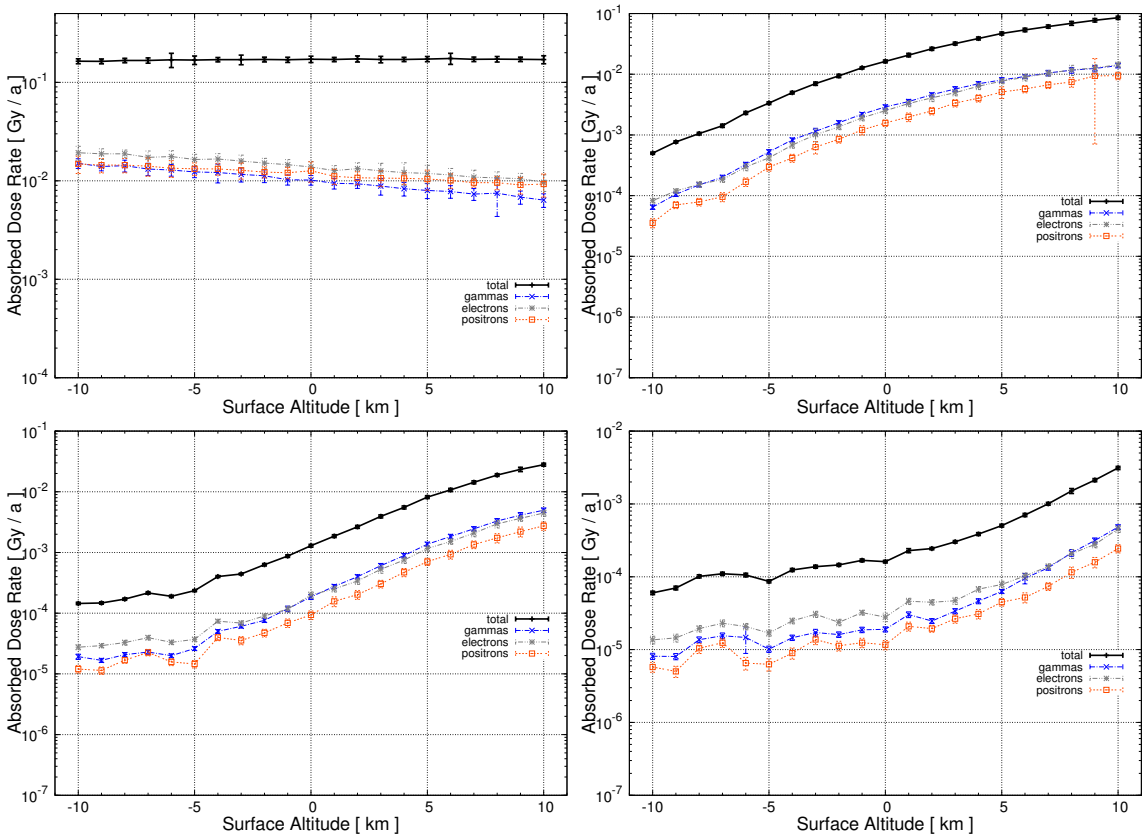

Figure A.1.: Absorbed dose rate contribution of selected particle types for different atmospheric conditions in dependence of the surface altitude. Top left: Present-day atmospheric pressure conditions. Top right: Increased atmospheric pressure with a factor of 25. Bottom left: Pressure increase factor of 50. Bottom right: Pressure increase factor of 100. Shown are the total absorbed dose rate (black), the gamma contribution (magenta), electrons (orange), and positrons (grey). The y-axes scales were chosen congruent with the respective plots in Fgs. 5.2, 5.4, 5.6, and 5.7.

under the different atmospheric conditions are given in table A.1. One can clearly see that, in general, all three particles deposit very similar doses under all depicted conditions, as their particle fluxes are coupled to each other via pair production and bremsstrahlung (see Ch. 2.1.1).

A.2. Contributions to the subsurface dose

Table A.2 gives the contributions of the particle species to the total subsurface absorbed dose rates for different soil depths. Note that for high pressure increases and

Table A.2.: Contribution of different particle species to the total subsurface dose rate for increased pressure conditions. Given are total dose rate and percentages to that dose for each particle species at a surface altitude of 0 km. The shown soil depths are 0 m (surface dose), 1 m, and 5 m. Note that for high pressure increases and deep soil depth, the influence of protons and neutrons is overestimated.

Pressure	x 25			x 50			x 100		
	0 m	1 m	5 m	0 m	1 m	5 m	0 m	1 m	5 m
Total Dose (mGy/a)	16	4.7	0.35	1.3	0.62	0.28	0.16	0.1	0.1
Protons	23.5 %	26.5 %	2 %	18 %	14 %	23.5 %	5.5 %	1 %	12 %
Alphas	0.5 %	0.5 %	0 %	0 %	0 %	4 %	0 %	0 %	0 %
Neutrons	26 %	32 %	6 %	21 %	24.5 %	7.8 %	6.5 %	3 %	12.5 %
Gammas	17.5 %	10 %	1.5 %	14 %	5.8 %	2 %	12 %	0.8 %	5.5 %
Electrons	15 %	8.5 %	0.5 %	15 %	6 %	3 %	17.5 %	0.5 %	2.2 %
Positrons	9.5 %	3.5 %	0.1 %	7.5 %	2.5 %	4.2 %	7 %	0.3 %	4 %
Muons	3.7 %	7.5 %	35 %	11 %	26.2 %	30.8 %	22.2 %	50 %	31.8 %
Antimuons	4 %	10.5 %	55 %	12 %	20.7 %	24.5 %	30 %	44.1 %	31.2 %

deep-situated soil layers, `PLANETOCOSMICS` overestimates the proton fluxes, apparently because of the low statistics involved. Furthermore, the percentages given here are averages, so variations in the trending values can occur, e.g. the alpha particle contribution at 50-times increased pressure.

A.3. Dose equivalent rates

Calculating the dose equivalent rate from the absorbed dose rate is done by applying the quality factor Q (as explained in Ch. 2.2). As the model is set up in a way that for every incident particle the necessary particle information, such as energy deposit or track length of the particle in the water volume, can be read out, the model allows to convert the absorbed dose from each registered event to a dose equivalent value. Fig. A.2 shows the resulting total equivalent dose rates in dependence of the surface altitude for the four different pressure-level scenarios and the corresponding calculated minimum and maximum values are given in Table A.3. Interestingly, for present-day conditions the

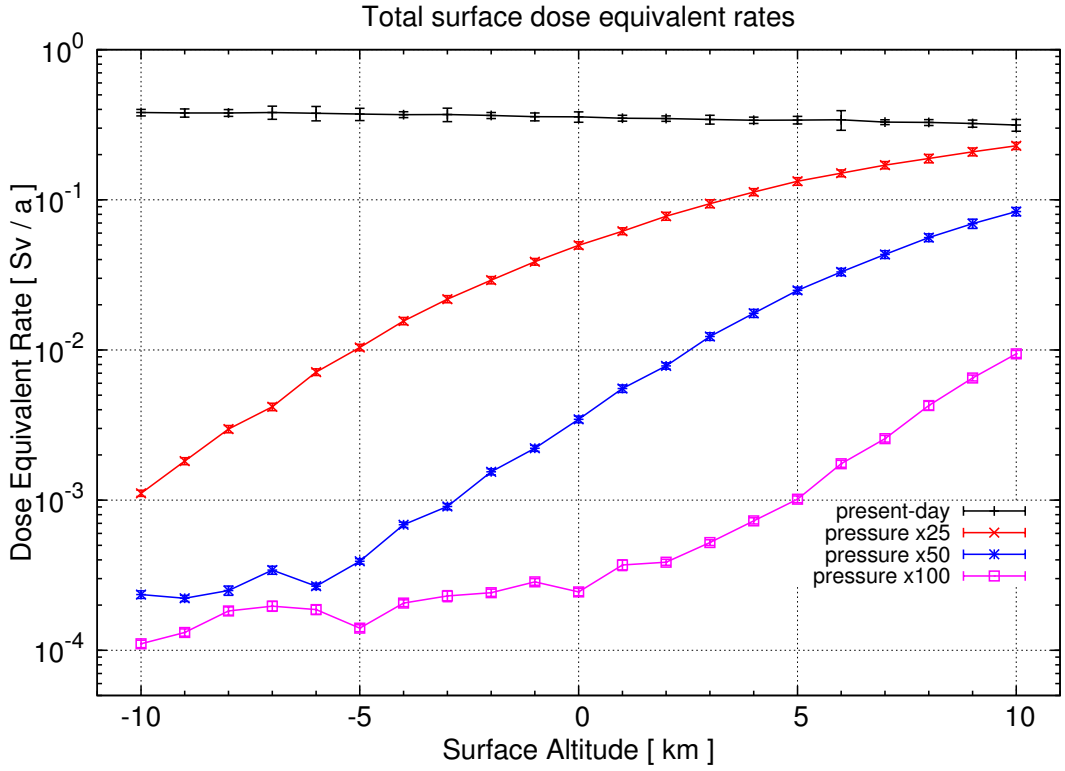

Figure A.2.: Total dose equivalent rate for different atmospheric conditions in dependence of the surface altitude. Present-day condition (black), increased pressure with a factor of 25 (red), pressure increase factor of 50 (blue), and factor of 100 (magenta).

total dose increases with decreasing elevation. In this case the Q-weighted contributions of neutrons show an increased influence on the total dose, outweighing the proton contribution and, therefore, leading to the observable anticorrelation with the surface altitude. The curves for the increased pressure scenarios show the same characteristics

Table A.3.: Total dose equivalent rates at the surface for different atmospheric pressure increases. Given are minimum and maximum values found for one atmospheric pressure level, considering all analysed surface altitudes of the respective scenario.

	Dose equivalent rates (mSv / a)
Present-day	314 - 318
Pressure x 25	1.1 - 229
Pressure x 50	0.24 - 83.5
Pressure x 100	0.11 - 9.4

as their respective absorbed dose curves (correlation with the elevation), as here the neutron contribution is also correlated with the surface altitude.

A.4. Estimating the HZE contribution

Even though protons and alpha particles dominate the atomic-nuclei-GCR composition (making up nearly 98 %), heavier ions (abbreviated as HZEs in the following) can have a significant effect on the absorbed dose of a GCR-induced radiation environment. For one, heavier ions have a higher energy loss, as according to Eq. 7.2: $\frac{dE}{dx} \sim Z^2$, which is important when regarding direct interactions of HZEs with organic matter. Furthermore, heavier ions also can produce comparably more secondaries when interacting with molecules of the atmosphere.

Therefore, when analysing any radiation environment or subsequent dose values due to exposure to it, the contribution of HZE ions can not be neglected. Unfortunately, as previously mentioned, on default `PLANETOCOSMICS` only considers protons and alpha particles as GCR-input spectra. So, when wanting to use the model, introduced in this work, for an estimation of the absorbed dose induced by the HZE component of the GCRs, other means have to be found.

A possible approach is to consider a HZE nucleus as the sum of its protons and neutrons, so e.g. considering a Fe ion as 26 protons and 30 neutrons. This is an approach also used by other research simulating HZE propagation, e.g., [*Molina-Cuberos et al.*, 2001], [*Sihver et al.*, 2008]. However, considering that a particle's energy loss scales with the square of the particle's charge, the induced dose by a direct HZE hit would be underestimated using this approach. E.g., for the present-day low atmospheric pressure on Mars alpha particles can propagate all the way to the surface and create proportionally more secondaries on its way. Comparing the dose rates created by primary

and secondary particles from the alpha particle component of the GCR spectrum and the ones from the proton component, we find that for present-day conditions the first component induces roughly 23 % of the dose, although the primary alpha particle flux is about one order of magnitude lower than the primary proton flux. Furthermore, aside from creating more secondary particles, alpha particles can also directly induce dose (see Fig. 5.2) at these low atmospheric depths, an effect that is also not properly represented by the proposed approach. Therefore, testing the approach for present-day conditions yields that dose rates created by the alpha-particle GCR component differ distinctively for the two variations. Simulating alphas as 2 protons and 2 neutrons yields a dose rate of $\sim$ 70 % compared to simulating alpha particles as one nucleus.

However, for higher-pressure conditions, i.e. for high atmospheric depths a primary ion would have to propagate through, a point is reached where a large fraction of the primary HZE nuclei have undergone enough fragmentation processes, so that they can be approximated as free protons and neutrons. For example, *Sihver et al.* [2008] showed that this approach can reproduce the secondary neutron fluence created by alpha particles in the atmosphere, if the atmospheric depth is high enough, i.e. for higher altitudes this approach fails. The approach was tested for the analysed, higher pressure conditions and could reproduce the absorbed surface dose rates of the alpha-particle simulations on average in an order of 10 - 15 % with some uncertainties at low elevations and high pressure levels.

To, now, estimate the contribution of particles, induced by GCR ions with charges $Z > 2$, the following steps were undertaken:

I. In an estimation, the input GCR spectrum for the model, described in Ch. 4.3, was assumed as protons, respectively neutrons, with a spectral distribution equal to the GCR-proton spectrum used in `PLANETOCOSMICS`.

II. From this, the resulting surface particle spectra were simulated with `PLANETOCOSMICS`, and subsequently the resulting species-dependent dose rates were calculated, with the method described in Ch. 4.3, for both proton- and neutron-induced environments.

III. These dose rates were then scaled with the appropriate proton/neutron-composition of a given ion species, e.g. 6 protons and 6 neutrons for carbon, as well as with the relative GCR abundance of the ion species compared to that of GCR protons, according to [*Shinn et al.*, 1994] (see Fig. A.3).

The resulting absorbed dose rate contributions induced by HZE ions for different environmental conditions are given in Table A.4. At first glance, there seems to be a visible trend that the HZE-induced dose rate decreases with higher atmospheric pres-

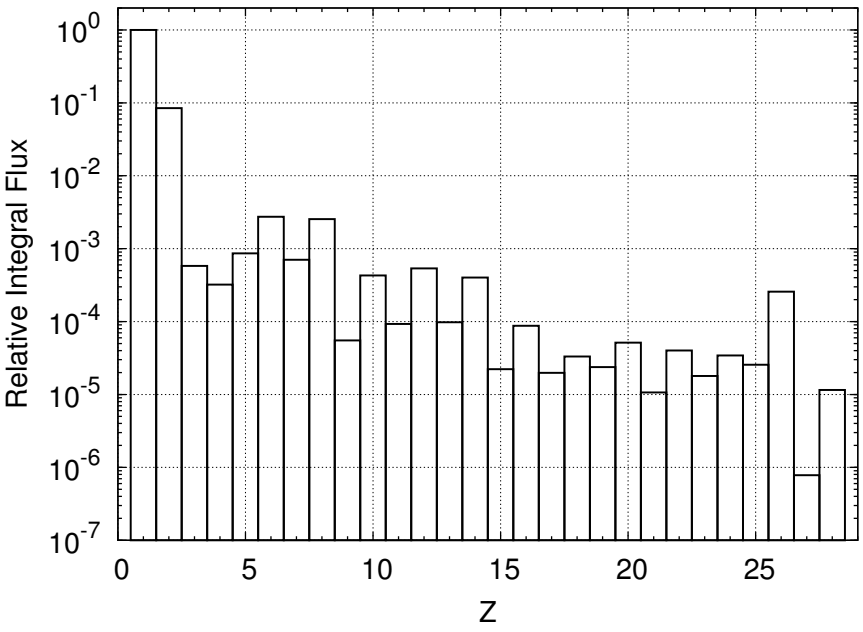

Figure A.3.: Relative GCR abundances of ion species with charges Z $\leq$ 28 for Solar minimum conditions. Shown are the relative integral fluxes (normalised to the integral proton flux) over the charge Z of the ion species. Adapted from [*Shinn et al.*, 1994].

sure levels, due to the added percentage to the dose decreasing. However, no such trend is discernible for increasing soil depth for a fixed pressure condition, which seems counterintuitive. One has to remember that the values given in the table are values relative to the proton- and alpha-particle-induced dose rate and not absolute values. Furthermore, the percentages are averaged over all considered altitudes for a given pressure level and show a range around the mean of $\pm$2 - 3 %. Therefore, we advise against taking these presented values as hard facts and rather to see them more as a rough estimate, due to the uncertainties introduced with this approach, e.g. due to its dependence on the column depth above the analysed layer.

As a conclusion, one can see that considering GCR heavy ions would yield an additional dose rate of roughly 5 - 10 % to the presented GCR-induced dose rates in Ch. 5. However, to improve the accuracy of these values, it is expedient to incorporate this of yet missing component of the input spectrum into `PLANETOCOSMICS`.

Table A.4.: HZE contribution to the total absorbed dose rates for different atmospheric environments. Given are averaged additional dose rates induced by HZEs with charges $3 \leq Z \leq 28$ for the surface and 1 m and 5 m deep in the soil.

Dry Mars model	Surface	1 m soil depth	5 m soil depth
Present-day	7.9 %	10 %	10 %
Pressure x 25	8.4 %	8.5 %	8.3 %
Pressure x 50	6.9 %	7.9 %	6.1 %
Pressure x 100	5 %	7 %	4.2 %
Water-ice model			
Present-day	7.9 %	8.9 %	9.1 %
Pressure x 25	7.9 %	8 %	6.8 %
Pressure x 50	6.8 %	6.2 %	6.5 %
Pressure x 100	5.6 %	4.7 %	6.4 %

B. Additional information for MSL/RAD

B.1. RAD detector naming scheme

For a better understanding of the results given in section 7.2, an overview of the nomenclature used for the silicon detector definitions will be given here and is summarised in table B.1. Each SSD is hexagonally shaped and segmented into inner (area C in

Table B.1.: List of the used nomenclature of the RAD detectors. Given are the name used for the respective detector, the physical detector it is based on, and – for the Si-detectors – which segments belong to the detector name.

Detector name	Physical detector	Segments used (for SSDs)
A1	A	S,T,U
A2	A	C
B	B	C
C	C	C
C2	B	H,R
	C	H,R
D	D	n/a
E	E	n/a
F1	F1	n/a
F2	F2	n/a

the right of fig. B.1) and outer parts (S,T and U), divided by an intermediate area (H and R). For detector A the outer (named A1 in the following) and inner segment (A2) are read out separately, which allows for a constraint of the acceptance angle of the charged particle telescope to certain angles. For detector B only the inner segment is read out for measurement purposes (B). The intermediate sections of B and C build an additional AC, identified as C2. Again, for detector C only the inner segment is used in the telescope (C). The outer segment functions as a read-out of the AC scintillator F1 (F1). A more detailed view of the ACs can be seen on the left in Fig. B.1.

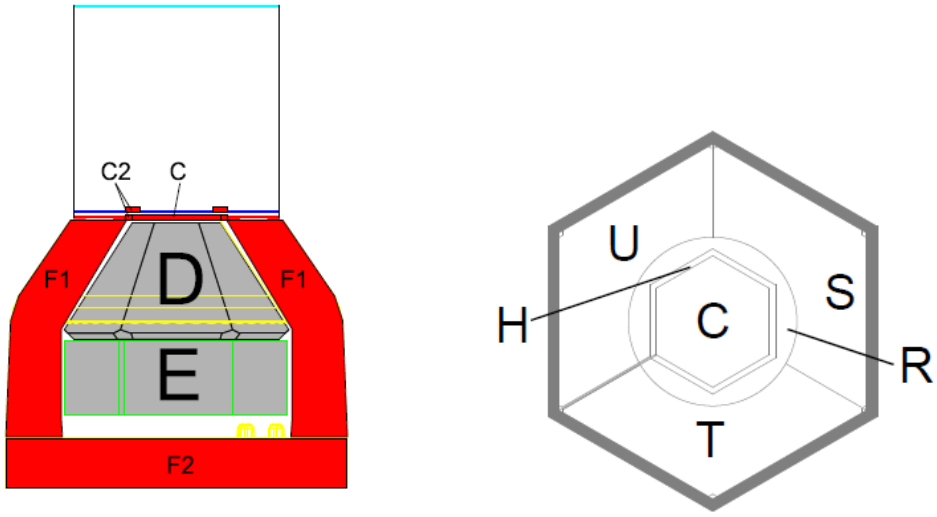

Figure B.1.: Left: Schematic of the AC. All detector segments functioning as AC are marked in red. Right: Schematic of the segmentation of the SSD detectors. The inner segment consists of the C part, S,T and U make up the outer segment, H is a guard ring, and R separates the inner and outer segments. Taken from *Kortmann* [2010].

B.2. Energy ranges of RAD detectors

Depending on the amplification stages, the different detectors of RAD are capable of resolving different energies, as all detectors have several gain channels available for which the amplification can differ from detector to detector. For example, the C SSD-detector has a significant lower energy range than the other SSDs (A1, A2, B). This was chosen deliberately, as the demands on this detector allow for a lower energy range. Table B.2 shows the maximum resolvable energy for all detectors. Note that the gain channels given there are the ones considered for digitisation, as of the time of this writing. The selection of channels digitised for read-out might be subject to change at a later date to improve the functionality of RAD, resultingly influencing the energy ranges of the afflicted detectors.

Table B.2.: List of maximum resolvable energies for the RAD detectors. The left column states the detector, the middle column lists all available gain channels, as they are considered for onboard digitisation at the moment. In the right column the maximum detectable energy is given. Calculated from [*Kuhnke*, 2011].

Detector	Read-out gain channels	Maximum energy
A1	A1U,A1H,A1M,A1L	749 MeV
A2	A2U,A2H,A2M,A2L	674 MeV
B	BU,BH,BM,BL	625 MeV
C	CU,CH,CM,CL	210 MeV
C2	C2,C2R	7 MeV
D	DU,DH,DI,DM,DN,DL	22 GeV
E	EU,EH,EI,EM,EN,EL	9 GeV
F1	F1	422 MeV
F2	F2	443 MeV

B.3. List of calibration runs

For completion's sake, an overview over the data used to calibrate the charged particle detection of the RAD instrument is given in Table B.3. In there, one can find references for the particle accelerator facility, the date of the measurement campaign, information about the used ion species and their energies, as well as additional calibration run details. For this research, data from calibration runs at the Brookhaven National Laboratory (BNL) in May 2008 and at the Heavy Ion Medical Accelerator in Chiba (HIMAC) in January 2009 and 2010 were available. The accelerator facilities are able to provide mono-energetic (in a reasonable accuracy) particle beams of different ion species. To expand the range of the collectable data from these provided beams, additional targets are placed between beam outlet and detector. The aim of these targets is twofold. For one, they can be used to influence the range of mono-energetic particles in the detectors, as a charged particle loses energy when traversing through these targets. A second advantage is, that besides from losing energy, ions are fragmented in the target and a broad range of different ions with lesser Z values are created. Thereby, one can measure several ion species by using just one initial species. Typical target materials used are Polyethylene (PE), Al or Cu.

Table B.3.: List of calibration run data used in this work to calibrate the RAD instrument with charged particle measurements. Information given here (from left to right): The particle accelerator facility, the date of the calibration campaign, the used ion species, its energy, additional information for the measurements.

Location	Date of beam time	Ion species	Energy	Additional Information
BNL	May 2008	Protons	80 MeV	
			95 MeV	
			105 MeV	
			110 MeV	1st run
			110 MeV	2nd run
			1 GeV	
		Fe	1 GeV	with 3 cm PE target in front of the detector
				with 20 cm PE target
				with 22 cm PE target
HIMAC	January 2010	Protons	160 MeV	with 11.36 $\frac{g}{cm^2}$ Cu and 0.81 $\frac{g}{cm^2}$ Al
				with 11.36 $\frac{g}{cm^2}$ Cu and 2.16 $\frac{g}{cm^2}$ Al
				with 11.36 $\frac{g}{cm^2}$ Cu and 3.51 $\frac{g}{cm^2}$ Al
				with 15.81 $\frac{g}{cm^2}$ Cu and 3.51 $\frac{g}{cm^2}$ Al
		Helium	180 MeV/nuc	no target
				with 15.81 $\frac{g}{cm^2}$ Cu and 2.16 $\frac{g}{cm^2}$ Al
				with 17.6 $\frac{g}{cm^2}$ Cu and 2.16 $\frac{g}{cm^2}$ Al
				with 22.05 $\frac{g}{cm^2}$ Cu and 2.16 $\frac{g}{cm^2}$ Al
		Carbon	230 MeV/nuc	no target
				with 1.79 $\frac{g}{cm^2}$ Cu
				with 4.6 $\frac{g}{cm^2}$ Cu
				with 5.95 $\frac{g}{cm^2}$ Cu
				with 6.845 $\frac{g}{cm^2}$ Cu
				with 11.345 $\frac{g}{cm^2}$ Cu
				with 12.185 $\frac{g}{cm^2}$ Cu
				with 17.885 $\frac{g}{cm^2}$ Cu

C. Further RAD Calibration and Simulation Data

In this section, further plots of calibration measurements and GEANT4 simulations are presented to provide a more complete picture of the work on on investigating onboard processing logic.

C.1. Calibration data

C.1.1. Charged particle triggers

As shown in Fig. 7.2, when detecting an event the first step for the electronics is to see if the measured particle qualifies as a charged particle. For this, the processing logic uses two different cut checks. First, it looks if a registered event can be classified as a HP charged particle, i.e. a particle with a high deposit in A and B. These high-LET particles should be found rarely on the Martian surface, as the flux of the higher-charged particles making up these events is rather low. However, high-energetic particles are, e.g., of great interest for dosimetry purposes, when evaluating the radiation risks for future manned missions to Mars. Therefore, the aim is to transmit as much information as possible back to Earth for these particles. The corresponding checks are shown in Fig. C.1. The lower boundary of the HP classification was beforehand defined as relativistic carbon, for which, unfortunately, there was no calibration data available. Therefore, the amount of energy deposit of such carbon in one of the SSD detectors was estimated via simulations and determined as ∼4.3 MeV. Now, with the use of the energy calibration developed by *Kuhnke* [2011], this corresponds to channel numbers of around 770 (for A2) and 810 (for B). To leave enough room for possible errors in this channel number determination, e.g. due to uncertainties in the energy calibration, this cut was placed at a slightly lower channel number of 700. In the plots presented in Fig. C.1, one can see that the smaller peaks between noise peak and cut value (form proton and helium calibration runs) are rejected, i.e. not classified as HP. The peak occurring at channel numbers of $\sim$ 1500 in the upper plots stems from carbon (with lower energies than relativistic ions).

If no HP classification is triggered, the event is checked for the possibility of being a

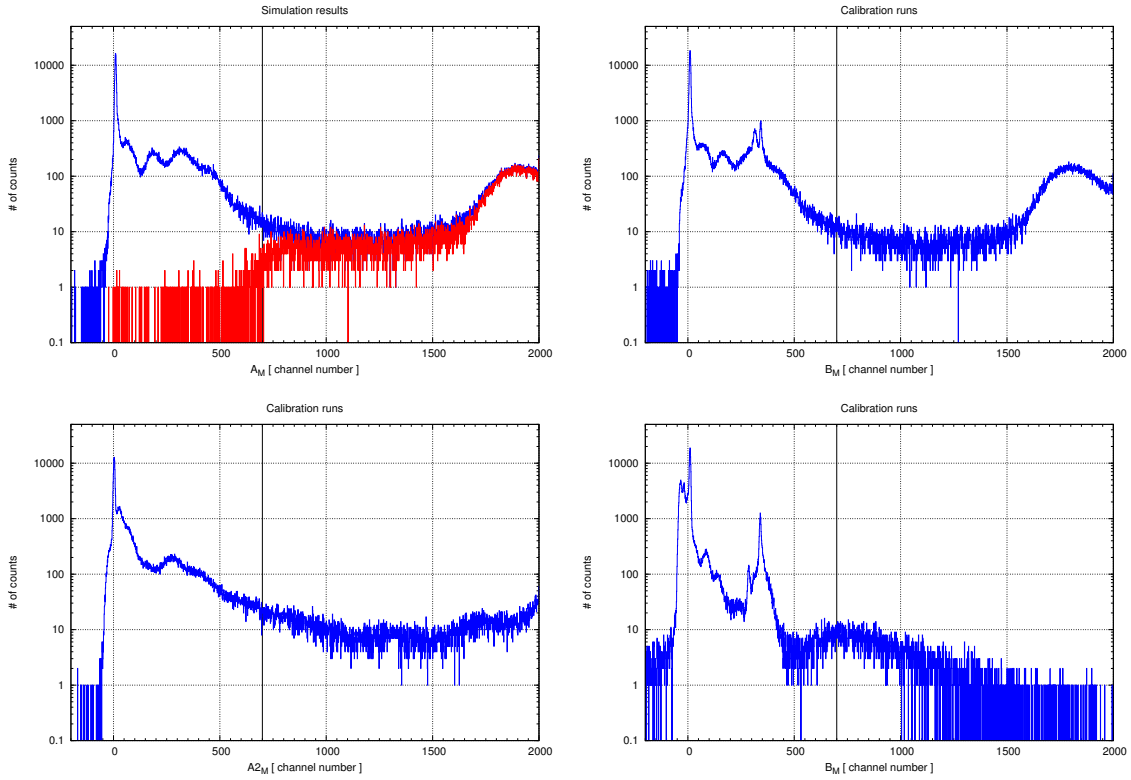

Figure C.1.: HP charged particle cuts. Top: Data for particles with a higher signal in A2 than in A1. Bottom: Particles with a higher signal in A1. For both cases, histograms for the interesting energy range of the medium gain channel of A1/A2 and B are shown. The black lines represents the cuts.

LP charged particle. These events should be much more common and, thus, there is the need for to reduce the data from these events. For the LP check, the remaining events are investigated for signals above the noise peak in A2 and B, under the additional condition that no signal above a certain threshold is detected in C2. The checks are shown in Fig. C.2. Both peaks of the double peak structure in the histograms of A2U and BU (below channel number 200) belong to the noise and are, therefore, rejected by the respective cuts and only events above this threshold are classified as LP. The same can be said for the C2 cut in the bottom left (below channel number 500). In the plots in the mid right and bottom right, this double peak structure is also marginally visible.

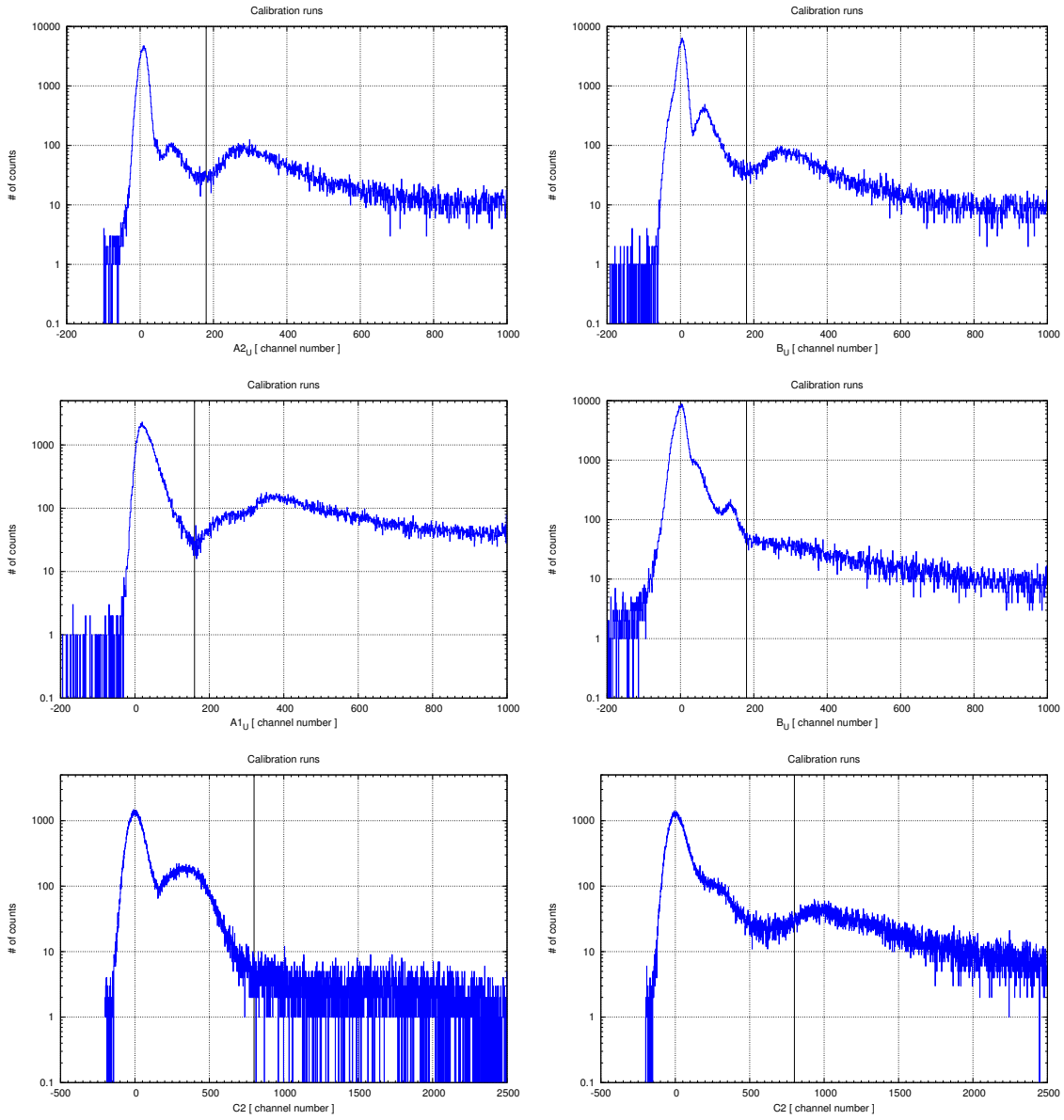

Figure C.2.: LP charged particle cuts for particles rejected by the HP cuts shown in Fig. C.1. Top: Data for particles with a higher signal in A2 than in A1. Mid: Particles with A1 > A2. For both cases, histograms for the interesting energy range of the ultra gain channel of A1/A2 and B are shown. Bottom left: Histogram of C2 for particles with higher signal in A2, bottom right: Histogram of C2 for particles with higher signal in A1. The black lines represent the cuts.

C.1.2. Dosimetry triggers

Dosimetry measurements of RAD are conducted with the B and E detector and measured data is stored in the respective dosimetry histograms for B and E. To classify if a dosimetry recording is warranted, both detectors are checked for significant energy deposits. Here, both HP and LP events are checked against the same cut condition, i.e. both priorities undergo the same checks. For B, the high gain channel is tested. The derived dosimetry cut value for detector B can be seen in the top panel of Fig. C.3, both for particles beforehand going through A2 (blue) and A1 (red), and was placed narrow to the steep flank of the occurring peak. The dosimetry check in E requires investigates the high (EH) and intermediate (EI) gain channel in coincidence condition and is shown in the mid and bottom panel of Fig. C.3.

LET triggers

As the cuts for HP and LP LET processing are the same as the cuts for charged particle classification, there are no further plots shown here.

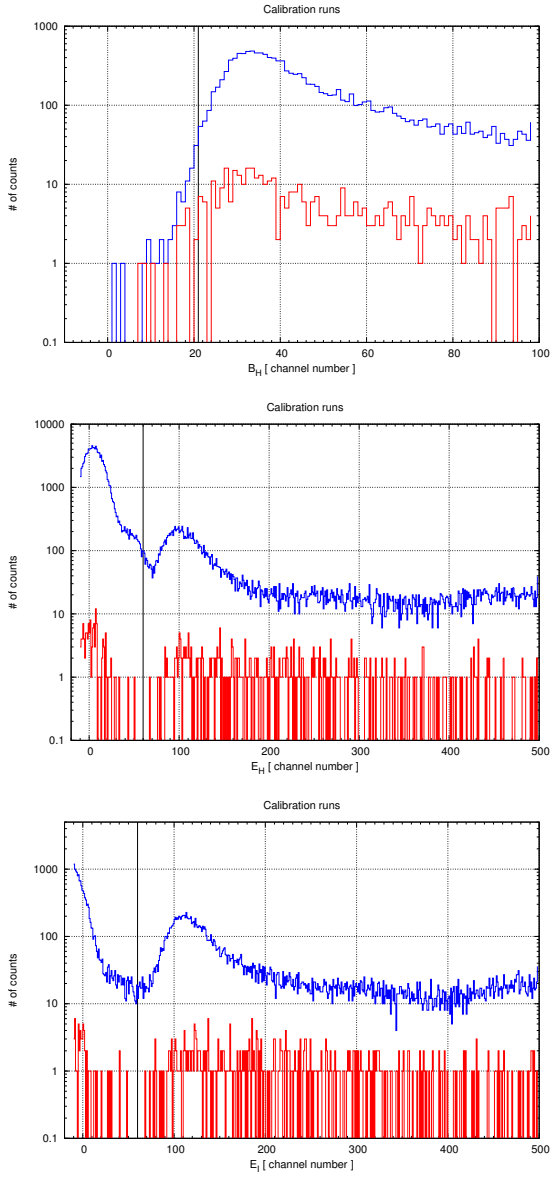

Figure C.3.: Top: Histogram of the gain channel BH. Mid: Histogram of EH. Bottom: Histogram of EI. Events that went through A2 are plotted in blue, events that went through A1 in red. The black lines represent the cut values.

C.1.3. Low Priority cuts for penetrating and stopping particle histograms

For the further LP classification of penetrating and stopping particles, one has to keep in mind that detectors A1/A2, B, and the AC channel C2 were all checked in the charged particle definition checks. Therefore, they do not have to be checked again in the following steps.

Penetrating particle logic

For LP penetrating particles, the interesting detectors left then are C, D, E, and F2. Therefore, this classification consists of four checks for significant energy in these detectors. To classify an event as an LP penetrating particle, all four detectors have to show a signal, in coincidence condition, above the cut value, In contrast to the previously presented charged particle triggers, etc., for these checks the total calibrated energy of all gain channels is considered, rather than just signals in one of the gain channels. The histograms of the detectors and the corresponding cut values are shown in Fig. C.4.

For C (top left panel) and D (top right) the cut can be placed directly at the flank of the first signal peak. Looking at the histograms for the E detector (bottom left), one can see that without this cut on E, a larger amount of events in the noise peak would be accepted by the logic (plotted in blue). This happens because of an unclean energy calibration in F2, as can be seen in the bottom right panel. Rejected and accepted events overlap over a wider range, because the noise peaks of different calibration runs could not be matched up with the currently used energy calibration. So, for E the cut can still be placed in the gap between falsely accepted noise peak and first event peak, but for F2 it gets more complicated. The resulting cut was chosen by further looking at ABCvF2 plots for LP events and, there, determining which events should likely be accepted. These additional considerations yielded a value very near to the junction of rejected (red) and accepted (blue) events in F2, so that the energy value at the junction was chosen as the cut value.

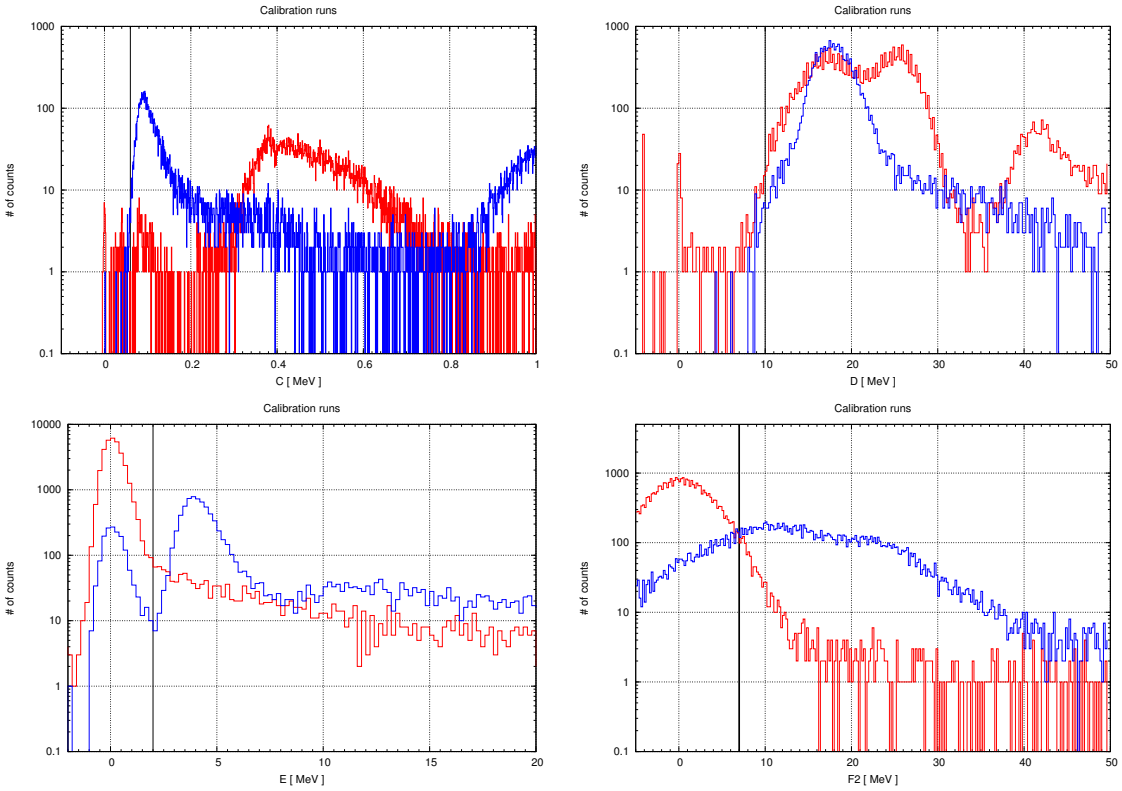

Figure C.4.: LP penetrating particle cuts. Plotted are histograms (in a cut-out of the whole detector energy range) of events accepted (blue) or rejected (red) by the other cuts than the one shown in the plot. The black lines represent the resulting cut values. The detectors are C (top left), D (top right), E (bottom left), and F2 (bottom right)..

Stopping particle logic

For LP stopping particles only two detectors remain to be checked. The idea is that if the AC scintillators F1 and F2 show no significant energy deposit, this along with the charged particle cuts means the particle would have had stopped somewhere in the detectors B, C, D, or E. In fig. C.5, the histograms for F1 (left) and F2 (right) can be seen. In both cases, it is relatively easy to place the necessary cut directly at the right flank of the noise peak, so that higher signals are rejected by the logic.

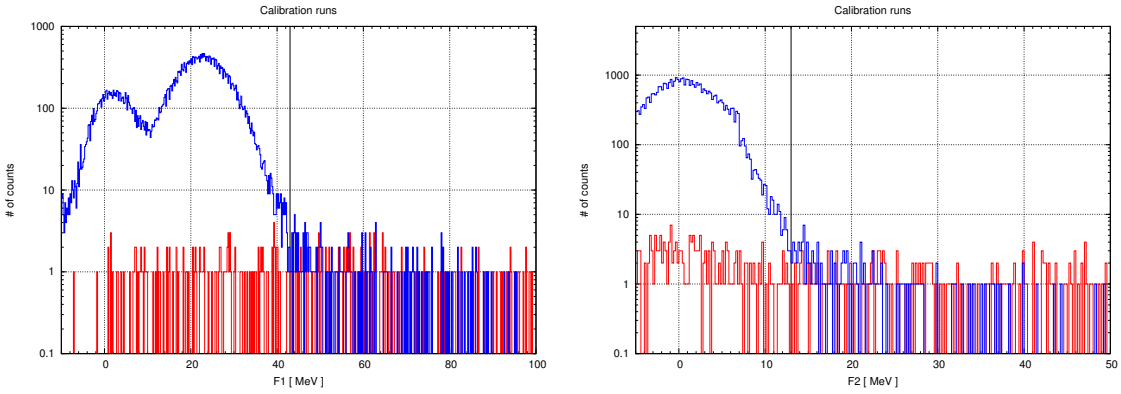

Figure C.5.: LP stopping particle cuts. Plotted are histograms (in a cut-out of the whole detector energy range) of events accepted (blue) or rejected (red) by the other respective cut. The black lines represent the resulting cut values. Left: Histogram of F1. Right: Histogram of F2.

C.1.4. A1 stopping particles

For the A1 part of the A detector (the outer segment) no penetrating particle classification is conducted, mainly for geometrical reasons. Therefore, only the stopping particle cuts have to be investigated.

Analysing the calibration run data for stopping particles that went through A1 is more difficult than for A2, due to the calibration-measurement setup used. During these runs, the detectorhead was aligned perpendicular to the pencil-like particle beam. Furthermore, the instrument was placed so that its top was centred on the beam. This, however, means that most of the time particles hit the A detector also in its centre (in the A2 segment), as the beam diameter is smaller than the diameter of the A detector. As the beam is no perfect pencil beam, there are particles that can go through A1, but then the flight path of the particles is not perpendicular to the detector anymore. This, in turn, leads to most of these particles not propagating through the inner parts of B and C, and rather going through C2. But, due to the setup of the particle processing logic, these events are then rejected from the logic. Therefore, applying the particle classification checks to the calibration data for hits in A1 can yield no significant results for the wanted cut values. This is illustrated for HP events in Fig. C.6. Although some of the structures from the corresponding plots for hits in A2 (compare Fig. 7.12) are recognisable in these plots, one can see that most of the events are rejected by the logic (plotted in red). The cause for this can be seen in the plots in the top left panel of Fig. C.6 (ABC v C2).

Due to the non-perpendicular flight path of particles hitting A1, they further prop-

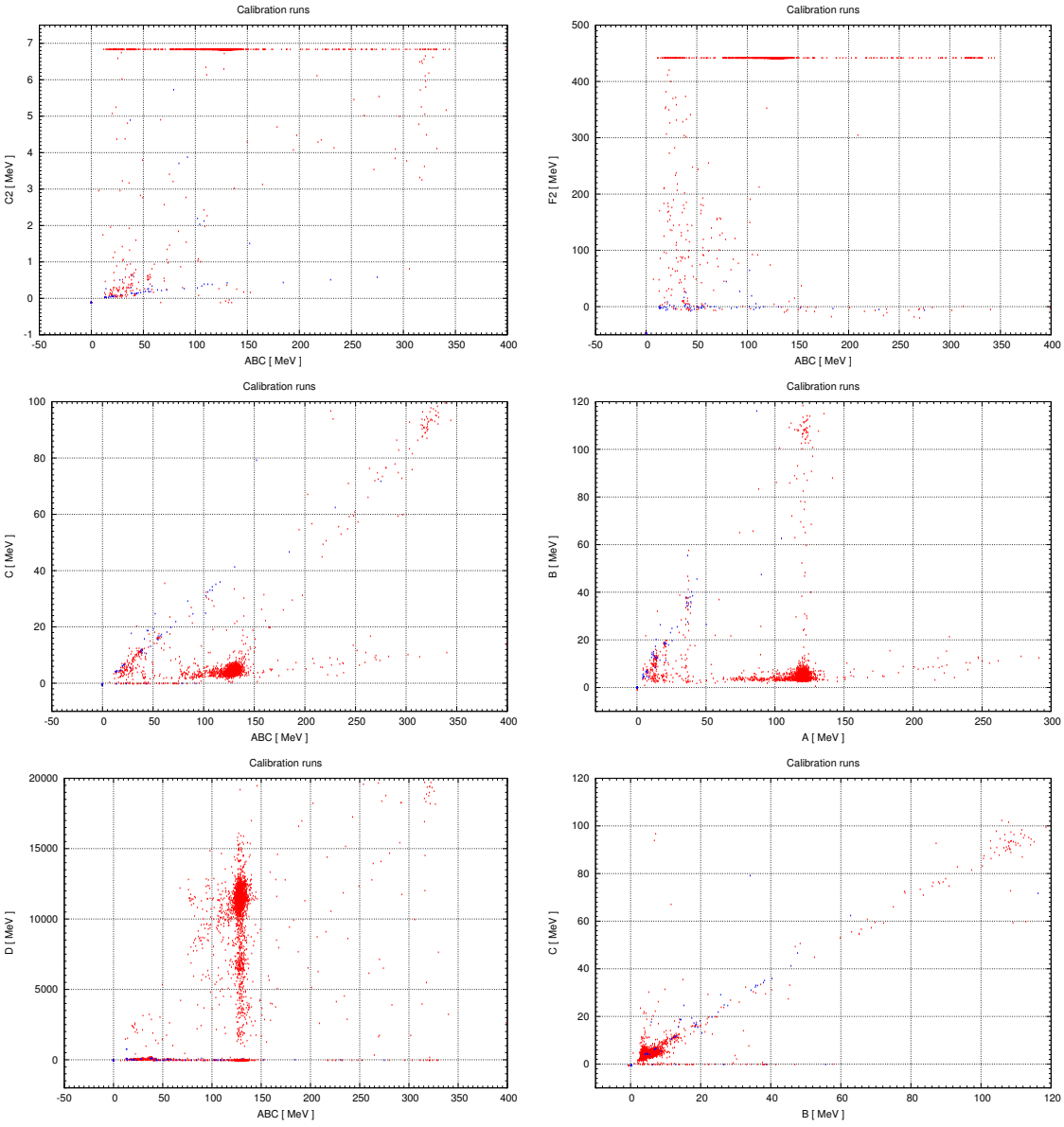

Figure C.6.: A1 HP stopping particle cut checks.

agate through the AC rather than through the "wanted" detectors. This leads to the events being in overflow in C2 and correspondingly to many events making next to zero deposit in B or C, which can be seen in the middle panel of the figure.

For LP stopping particles, the cut conditions for particles traversing A1 are shown in Fig. C.7. The cuts used here are the same ones as derived from the A2 LP event

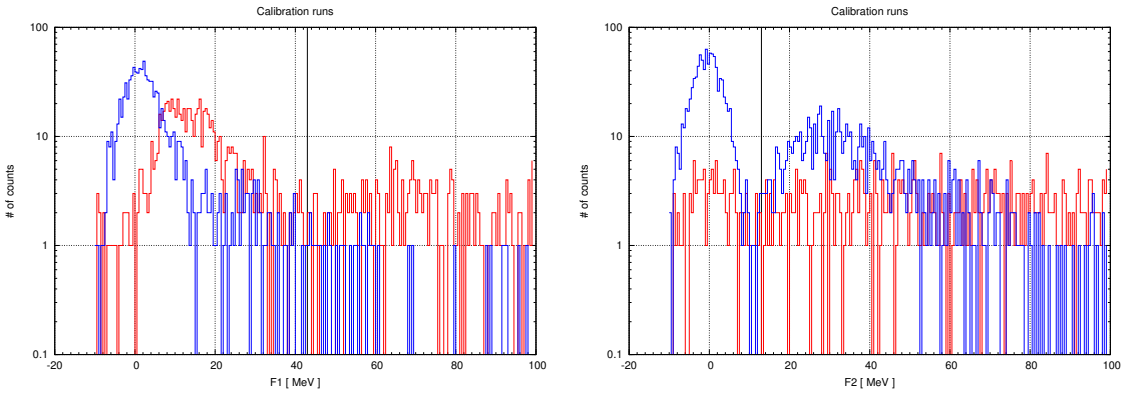

Figure C.7.: A1 LP stopping particle cuts. Left: F1, right: F2. Particles passing the other respective cut are plotted in blue, events that are rejected in red. The black line shows the cut condition derived from the A2 LP data. Not the whole energy range of the detectors is shown.

classification, as the onboard electronics uses the same cut for both events hitting A1 or A2. In the left panel, one can see the resulting event classification for F1, when the F2 cut is applied.

Fig. C.8 shows the resulting stopping particle histogram for particles hitting A1 (both HP and LP events). As mentioned before, the statistics for events classified as stopping is unfortunately very low, so that no proper conclusions about the quality of the cuts can be drawn from this plot. Therefore, it is mostly shown for the sake of completeness. However, the plots in Fig. C.6 show that the few HP events passing the cuts show similar behaviour to the ones going through A2. This leads to the conclusion that cut values derived for the A2 stopping histogram should in a first estimation be also applicable for the A1 stopping histogram. For the LP data, the cuts derived from the A2 data also work reasonably well, as far as the low statistics allow an assessment.

Again, the problem of low statistics is mostly due to the calibration run setup. Better statistics to fine-tune these cuts can most probably be derived on the flight to Mars.

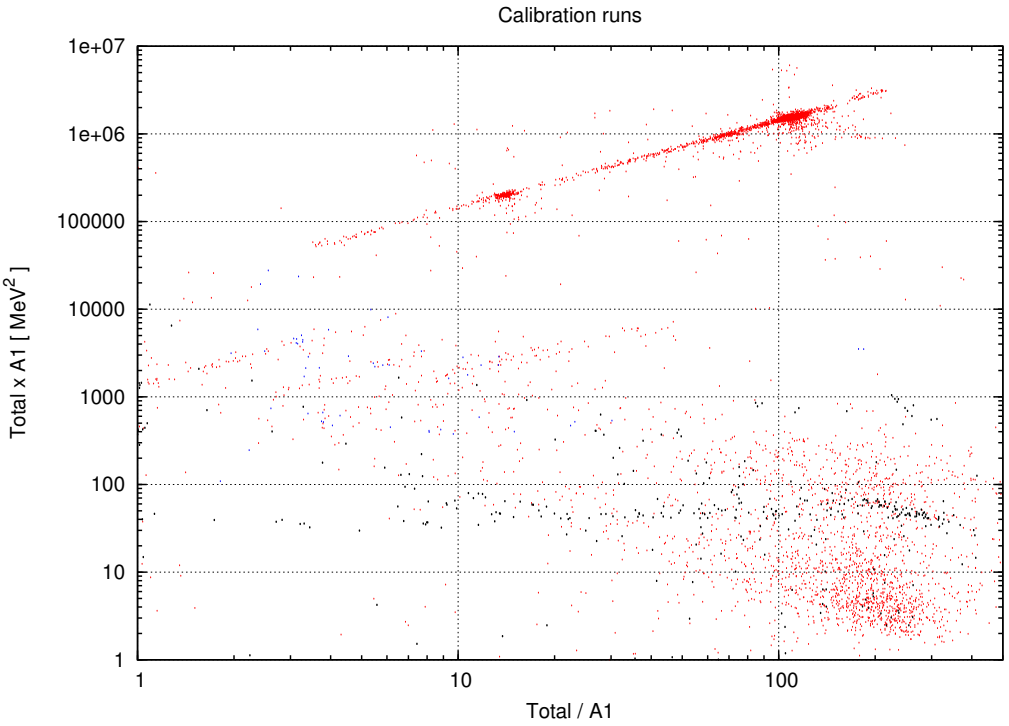

Figure C.8.: The resulting A1 stopping particle histogram. HP events, classified as stopping, are plotted in blue, LP events, classified as stopping, in black. HP and LP events rejected by the logic are plotted in red.

C.2. GEANT4 simulations

In this section further results from simulations with the `GEANT4` model of RAD are presented. Fig. C.9 shows simulation data plotted in arrangements corresponding to the calibration data plots for the HP particle processing presented in Ch. 7.2.2. One main difference between simulated and real detector is that the latter has hard energy range limits, i.e. only a certain amount of energy deposit can still be resolved in the detectors. Furthermore, as mentioned before, the `GEANT4` simulation does not include quenching, which is why the simulated energy deposits in the scintillators are higher than in the real measurements. The penetrating particles in the ABCvA2, ABCvB, and ABCvC plots show very similar characteristics to the calibration run plots. The ABCvD plot also shows a comparable distribution, penetrating particles lie on one line with a steep slope, while the different stopping particle population are situated on branches diverting from the penetrating line. Due to the not considered quenching, the ABCvE plot is not so nicely comparable with the measurements. However, one can see that particles penetrating E deposit roughly 300 MeV in ABC at maximum, which

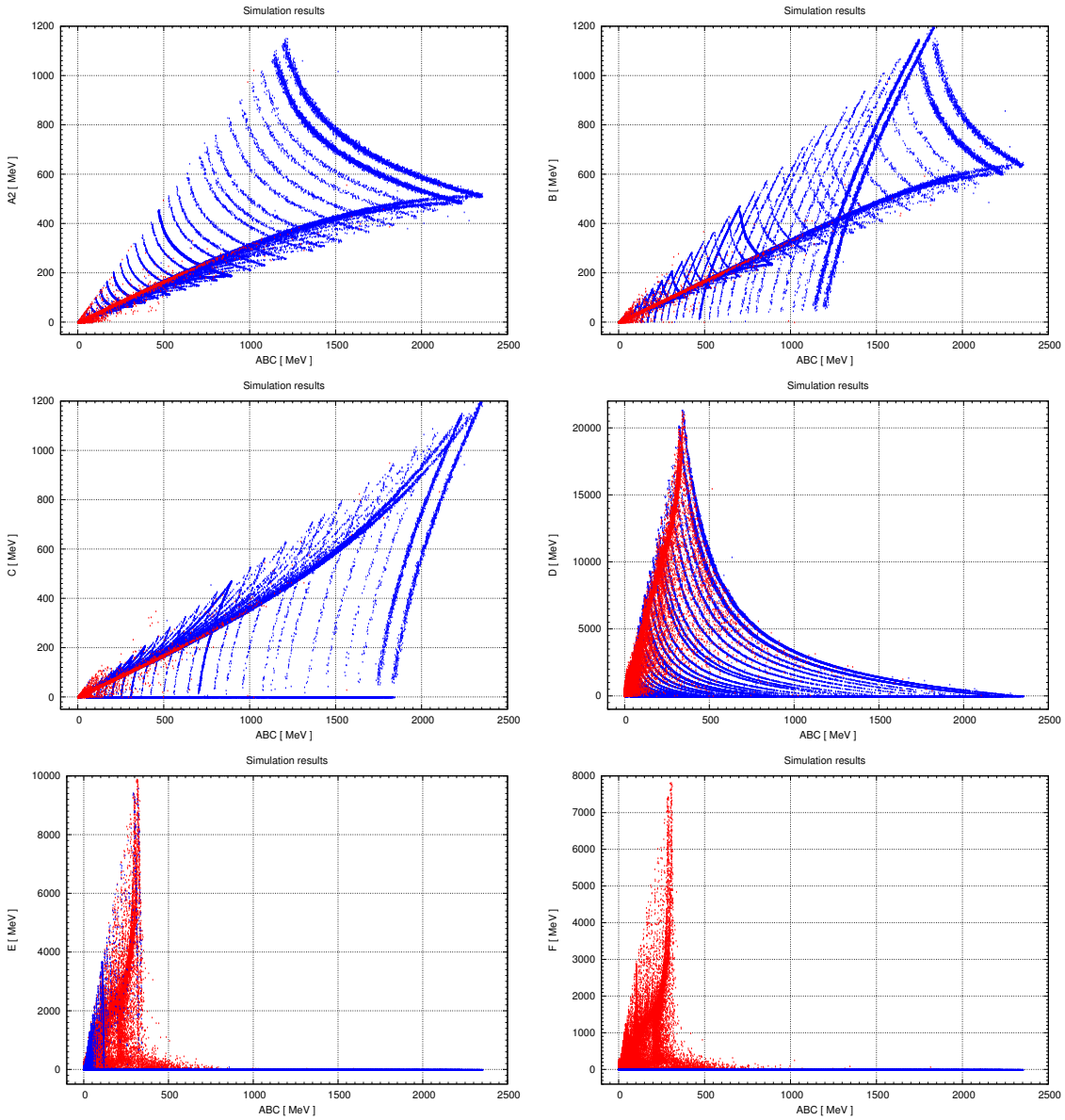

Figure C.9.: GEANT4 simulation results comparing the energy deposit in different detectors to the deposit in the telescope. Top left: ABCvA2, top right: ABCvB. Mid left: ABCvC, mid right: ABCvD. Bottom left: ABCvE, bottom right: ABCvF. Particles stopping in one of the detectors are shown in blue, particles penetrating the detectors are plotted in red.

corresponds to the measured energy deposit in the telescope of such particles. The ABCvF plot includes deposits in both F1 and F2, because of the setup of the GEANT4 RAD model, and is, here, mostly included for the sake of completeness, as, due to the limited energy range of the "real" F detectors, no significant conclusions can be drawn from a comparison with the measurements.

C.3. Derived cut values for charged particle processing

Table C.1.: List of cut values determined for the processing logic for HP charged penetrating and stopping particle determination. The left column shows the check condition and in the right column the determined values is given.

Logic check	Determined value
	Penetrating particles
$E_{Dep,C2} < x$	6.5 MeV
$E_{Dep,ABC} < x \cdot E_{Dep,A}$	6
$E_{Dep,ABC} < x \cdot E_{Dep,B}$	6
$E_{Dep,ABC} < x \cdot E_{Dep,C}$	6
$E_{Dep,ABC} \cdot x < E_{Dep,D}$	5
$E_{Dep,ABC} \cdot x < E_{Dep,E}$	2.5
$E_{Dep,ABC} \cdot x < E_{Dep,F2}$	1.33
$E_{Dep,F2} > x$	440 MeV
	Stopping particles
$E_{Dep,ABC} > x \cdot E_{Dep,C2}$	3.3
$E_{Dep,C2} < x$	6.5 MeV
$E_{Dep,ABC} > x \cdot E_{Dep,F2}$	1.5
$E_{Dep,ABC} < x \cdot E_{Dep,C}$	6
$E_{Dep,D} < x$	5 MeV
$\max(E_{Dep,A},E_{Dep,B}) < x \cdot \min(E_{Dep,A},E_{Dep,B})$	2
$E_{Dep,ABC} \cdot x < E_{Dep,D}$	5
$\max(E_{Dep,B},E_{Dep,C}) < x \cdot \min(E_{Dep,B},E_{Dep,C})$	2

Bibliography

Acuña, M. H., et al., Global Distribution of Crustal Magnetization Discovered by the Mars Global Surveyor MAG/ER Experiment, *Science*, *284*, 790, 1999.

Acuña, M. H., et al., Magnetic field of Mars: Summary of results from the aerobraking and mapping orbits, *J. Geophys. Res.*, *106*, 23,403–23,418, 2001.

Agostinelli, S., et al., Geant4-a simulation toolkit, *Nuclear Instruments and Methods in Physics Research A*, *506*, 250–303, 2003.

Allkofer, O. C., *Introduction to Cosmic Radiation*, Verlag Karl Thiemig München, 1974.

Amsler, C., et al., Review of particle physics, *Physics Letters B*, *667*, 1 – 6, 2008.

Arkani-Hamed, J., Timing of the Martian core dynamo, *J. Geophys. Res. (Planets)*, *109*, 3006, 2004.

Barendsen, G. W., Radiation-induced DNA damage in relation to linear and quadratic terms of dose-effect relationships for cell reproductive death., *BJR Suppl.*, *24*, 53 – 56, 1992.

Barlow, N. G., *"Mars - An Introduction to its Interior, Surface and Atmosphere"*, Cambridge University Press, 2008.

Barnard, L., and M. Lockwood, A survey of gradual solar energetic particle events, *Journal of Geophysical Research (Space Physics)*, *116*, 5103, 2011.

Battista, J. R., Against all odds: The survival strategies of *Deinococcus radiodurans*, *Annu. Rev. Microbiol.*, *51*, 203 – 224, 1997.

Baumstark-Khan, C., and R. Facius, *Life under conditions of ionizing radiation. In: Astrobiology. The Quest for the Conditions of Life.*, pp. 260–283, Springer Verlag, 2001.

Bethge, K., *Kernphysik – Eine Einführung*, Springer Verlag, 1996.

Boyce, J. M., *The Smithsonian Book of Mars*, Smithonian Press, 2002.

Brain, D. A., and B. M. Jakosky, Atmospheric loss since the onset of the Martian geologic record: Combined role of impact erosion and sputtering, *J. Geophys. Res.*, *103*, 22,689–22,694, 1998.

Böttcher, S., Signal processing in the Radiation Assessment Detector for MSL, rev. 1.5, *Tech. rep.*, Christian-Albrechts-Universität zu Kiel, 2011.

Carr, M. H., and J. W. Head, Geologic history of Mars, *Earth and Planetary Science Letters*, *294*, 185–203, 2010.

Chassefière, E., and F. Leblanc, Mars atmospheric escape and evolution; interaction with the solar wind, *Planetary and Space Science*, *52*, 1039–1058, 2004.

Chyba, C. F., and K. P. Hand, ASTROBIOLOGY: The Study of the Living Universe, *Annu. Rev. Astron. Astrophys.*, *43*, 31–74, 2005.

Clowdsley, M. S., J. S. Wilson, M. H. Kim, R. C. Singleterry, R. K. Tripathi, J. H. Heinbockel, F. F. Badavi, and J. L. Shinn, Neutron environments on the martian surface, *Physica Medica*, *17*, 94–96, 2001.

Cockell, C. S., and J. A. Raven, Zones of photosynthetic potential on Mars and the early Earth, *Icarus*, *169*, 300 – 310, 2004.

Connerney, J. E. P., et al., Magnetic Lineations in the Ancient Crust of Mars, *Science*, *284*, 794–798, 1999.

Cox, M. M., and J. R. Battista, *Deinococcus radiodurans* – The consummate survivor, *Nature Rev. Microbiol.*, *3*, 882–892, 2005.

Cucinotta, F. A., P. B. Saganti, J. W. Wilson, and L. C. Simonsen, Model predictions and visualization of the particle flux on the surface of Mars, *J. Radiat. Res.*, *43 suppl.*, 35–39, 2002.

Dartnell, L. R., L. Desorgher, J. M. Ward, and A. J. Coates, Modelling the surface and subsurface Martian radiation environment: Implications for astrobiology, *Geophysical Research Letters*, *34*, 2007A.

Dartnell, L. R., L. Desorgher, J. M. Ward, and A. J. Coates, Martian sub-surface ionising radiation: biosignatures and geology, *Biogeosciences Discussions*, *4*, 455–492, 2007B.

Desorgher, L., E. O. Flückiger, and M. Gurtner, The PLANETOCOSMICS Geant4 application, in *36th COSPAR Scientific Assembly*, vol. 36, pp. 2361–+, 2006.

Fassett, C. I., and J. W. Head, Valley network-fed, open-basin lakes on Mars: Distribution and implications for Noachian surface and subsurface hydrology, *Icarus*, *198*, 37–56, 2008.

Feldman, W. C., et al., Global distribution of near-surface hydrogen on Mars, *Journal of Geophysical Research (Planets)*, *109*, 9006, 2004.

Garcia-Munoz, M., G. M. Mason, and J. A. Simpson, The anomalous He-4 component in the cosmic-ray spectrum at below approximately 50 MeV per nucleon during 1972-1974, *apj*, *202*, 265–275, 1975.

Gleeson, L. J., and W. I. Axford, Solar modulation of galactic cosmic rays, *apj*, *154*, 1011–+, 1968.

Goulding, F. S., and B. G. Harvey, Identification of nuclear particles, *Annual Review of Nuclear Science*, *25*, 167–240, 1975.

Grießmeier, J.-M., A. Stadelmann, U. Motschmann, N. K. Belisheva, H. Lammer, and H. K. Biernat, Cosmic Ray Impact on Extrasolar Earth-Like Planets in Close-in Habitable Zones, *Astrobiology*, *5*, 587–603, 2005.

Gurtner, M., L. Desorgher, E. O. Flückiger, and M. R. Moser, Simulation of the interaction of space radiation with the Martian atmosphere and surface, *Advances in Space Research*, *36*, 2176–2181, 2005.

Heber, B., H. Fichtner, and K. Scherer, Solar and Heliospheric Modulation of Galactic Cosmic Rays, *Space Sci. Rev.*, *125*, 81–93, 2006.

Hillas, A. M., Can diffusive shock acceleration in supernova remnants account for high-energy galactic cosmic rays?, *Journal of Physics G: Nuclear and Particle Physics*, *31*, R95, 2005.

ICRP60, *ICRP Publication 60: The 1990 Recommendations of the International Commission on Radiological Protection*, vol. Ann. ICRP 21 (1–3), 1991.

Jakosky, B., and R. Phillips, Mars' volatile and climate history., *Nature*, *412*, 237–44, 2001.

James, F., Monte Carlo theory and practice, *Reports on Progress in Physics*, *43*, 1145–1189, 1980.

Janitzek, N., Analyse der Zenithalwinkelverteilung des GCR-induzierten Strahlungsfeldes auf dem Marsboden, *Bachelor's thesis*, Christian-Albrechts-Universität Kiel, 2010.

Kahn, R., The evolution of CO2 on Mars, *Icarus*, *62*, 175 – 190, 1985.

Kieffer, H. H., B. M. Jakosky, C. W. Snyder, and M. S. Matthews (Eds.), *Mars*, The University of Arizona Press, 1992.

Kortmann, O., Scintillator performance investigation for MSL/RAD, Ph.D. thesis, Christian-Albrechts-Universität Kiel, 2010.

Kuhnke, M., Procedure for the Calibration of the Radiation Assessment Detector for the Mars Science Laboratory, *Tech. rep.*, Christian-Albrechts-Universität zu Kiel, 2011.

Köhler, J., Gamma/neutron separation in the Martian radiation environment, Ph.D. thesis, Christian-Albrechts-Universität Kiel, 2012.

Köhler, J., B. Ehresmann, C. Martin, E. Böhm, A. Kharytonov, O. Kortmann, C. Zeitlin, D. M. Hassler, and R. F. Wimmer-Schweingruber, Inversion of neutron/gamma spectra from scintillator measurements, *Nuclear Instruments and Methods in Physics Research B*, *269*, 2641–2648, 2011.

Lammer, H., W. Stumptner, and G. J. Molina-Cuberos, *Martian atmospheric evolution: implications of an ancient intrinsic magnetic field*, pp. 203–217, 2002.

Langevin, Y., F. Poulet, J.-P. Bibring, B. Schmitt, S. Douté, and B. Gondet, Summer Evolution of the North Polar Cap of Mars as Observed by OMEGA/Mars Express, *Science*, *307*, 1581–1584, 2005.

Leblanc, F., J. G. Luhmann, R. E. Johnson, and E. Chassefiere, Some expected impacts of a solar energetic particle event at Mars, *Journal of Geophysical Research (Space Physics)*, *107*, 1058, 2002.

Leo, W. R., *Techniques for Nuclear and Particle Physics Experiments*, Springer, 1994.

Marinova, M., O. Aharonson, and E. Asphaug, Mega-impact formation of the Mars hemispheric dichotomy, *Nature*, *453*, 1216, 2008.

Melosh, H. J., and A. M. Vickery, Impact erosion of the primordial atmosphere of Mars, *Nature*, *338*, 487–489, 1989.

Mileikowsky, C., et al., Natural Transfer of Viable Microbes in Space: 1. From Mars to Earth and Earth to Mars, *Icarus*, *145*, 391 – 427, 2000.

Mitrofanov, I. G., et al., Soil Water Content on Mars as Estimated from Neutron Measurements by the HEND Instrument Onboard the 2001 Mars Odyssey Spacecraft, *Solar System Research*, *38*, 253–257, 2004, 10.1023/B:SOLS.0000037461.70809.45.

Molina-Cuberos, G. J., W. Stumptner, H. Lammer, N. I. Kömle, and K. O'Brien, Cosmic Ray and UV Radiation Models on the Ancient Martian Surface, *Icarus*, *154*, 216–222, 2001.

Nelson, G. A., Fundamental space radiobiology, *Gravit. Space Biol. Bull.*, *16*, 29 – 36, 2003.

Owen, T., K. Biemann, J. E. Biller, A. L. Lafleur, D. R. Rushneck, and D. W. Howarth, The composition of the atmosphere at the surface of Mars, *JGR*, *82*, 4635 – 4639, 1977.

Pavlov, A. K., A. V. Blinov, and A. N. Konstantinov, Sterilization of Martian surface by cosmic radiation, *Planetary and Space Science*, *50*, 669 – 673, 2002.

Pérez-de-Tejada, H., R. Lundin, H. Durand-Manterola, and M. Reyes-Ruiz, Solar wind erosion of the polar regions of the Mars ionosphere, *Journal of Geophysical Research (Space Physics)*, *114*, 2106, 2009.

Prantzos, N., On the origin and composition of Galactic cosmic rays, *ArXiv e-prints*, 2011.

RAD Proposal, *RAD Radiation Assessment Detector Proposal by Southwest Research Institue and Christian-Albrechts-Universität zu Kiel*, 2006.

Roberts, J. H., R. J. Lillis, and M. Manga, Giant impacts on early Mars and the cessation of the Martian dynamo, *Journal of Geophysical Research (Planets)*, *114*, 4009, 2009.

Saganti, P. B., F. A. Cucinotta, J. W. Wilson, T. F. Cleghorn, and C. J. Zeitlin, Model calculations of the particle spectrum of the galactic cosmic ray (GCR) environment: Assessment with ACE/CRIS and MARIE measurements, *Radiation Measurements*, *41*, 1152 – 1157, 2006.

Scherer, K., et al., Interstellar-terrestrial relations: Variable cosmic environments, the dynamic heliosphere, and their imprints on terrestrial archives and climate, *Space Science Reviews*, *127*, 327 – 465, 2006.

Shaviv, N. J., and J. Veizer, Celestial driver of phanerozoic climate?, *GSA Today*, *13*, 4, 2003.

Shinn, J., J. Nealy, L. Townsend, J. Wilson, and J. Wood, Galactic cosmic ray radiation levels in spacecraft on interplanetary missions, *Advances in Space Research*, *14*, 863 – 871, 1994.

Sihver, L., D. Matthiä, T. Koi, and D. Mancusi, Dose calculations at high altitudes and in deep space with GEANT4 using BIC and JQMD models for nucleus nucleus reactions, *New Journal of Physics*, *10*, 105,019, 2008.

Simonsen, L. C., and J. E. Nealy, *Mars surface radiation exposure for solar maximum conditions and 1989 solar proton events.*, 1993.

Simpson, J. A., Elemental and Isotopic Composition of the Galactic Cosmic Rays, *Annual Review of Nuclear and Particle Science*, *33*, 323–382, 1983.

UNSCEAR, Sources and effects of ionizing radiation. UNSCEAR 1993 report to the General Assembly, 1993.

Webber, W. R., The interstellar cosmic ray spectrum and energy density. interplanetary cosmic ray gradients and a new estimate of the boundary of the heliosphere, *aap*, *179*, 277–284, 1987.

Zeitlin, C., et al., Overview of the Martian radiation environment experiment, *Advances in Space Research*, *33*, 2204–2210, 2004.

List of Acronyms

AC	Anti-Coincidence
BNL	Brookhaven National Laboratory
CAU	Christian-Albrechts-Universität
CFA	Colony Forming Ability
CME	Coronal Mass Ejection
DLR	Deutsches Zentrum für Luft- und Raumfahrt
DNA	Deoxyribonucleic acid
GCR	Galactic Cosmic Ray
GEANT	Geometry and Tracking
HIMAC	Heavy Ion Medical Accelerator in Chiba
HP	High Priority
HZE	High Charge and Energy
ICRP	International Commission on Radiological Protection
LET	Linear Energy Transfer
LHB	Late Heavy Bombardment
LP	Low Priority
MARIE	Martian Radiation Environment Experiment
MC	Monte-Carlo
MGS	Mars Global Surveyor
MOLA	Mars Orbiter Laser Altimeter
MSL	Mars Science Laboratory
NASA	National Aeronautics and Space Administration
PE	Polyethylene
PHA	Pulse Height Analysis
RAD	Radiation Assessment Detector
SEP	Solar Energetic Particle
SN	Supernova
SNR	Supernova Remnant
SPE	Solar Particle Event
SSD	Solid-State Detector
SwRI	Southwest Research Institute
UV	Ultra-Violet

Danksagung

Herrn Prof. Dr. R. F. Wimmer-Schweingruber danke ich für die Vergabe des Themas und die stets vermittelte Begeisterung am Forschungsfeld der Extraterrestrischen Physik. Des Weiteren danke ich ihm, dass die Tür zu seinem Büro immer offen stand und er, auch wenn er viel zu tun hatte, immer bereit war, Fragestellungen und Probleme zu erörtern.

Den feinen Herren Doktoren, Dr. Lars Berger, Dr. Jens Buck, Dr. Muharrem Köten und Dr. Roland Rodde, danke ich vor allem für den Ansporn auch selbst noch einen weiteren akademischen Grad vor den Dipl. Phys. zu setzen. Ausserdem möchte ich mich bei ihnen für ein sehr angenehmes Begleiten meiner Studien-, Diplomanden- und Doktorandenzeit bedanken.

Aus der Abteilung "Extraterrestrik" danke ich des Weiteren insbesondere Herrn Dr. Sönke Burmeister, Herrn Dipl. Phys. Thomas Möller, Herrn Dipl. Phys. Johannes Labrenz, Herrn Dipl. Phys. Christian Drews, Herrn Dipl. Phys. Christoph Terasa, Herrn Dipl. Phys. Jan Grunau und meinem Lieblings-Büropartner Herrn Dipl. Phys. Lauri Panitzsch für die zahllosen (zumeist nicht-)wissenschaftlichen Unterhaltungen während und vor allem auch mal nach der Arbeitszeit. Nicht zu vergessen sei hier natürlich auch Herr Dipl. Phys. Jan Köhler, bei dem ich mich speziell auch nochmal für die großartige Teamarbeit beim MSL-Projekt und für das Beheben etlicher Computer-Probleme bedanke. Im Grunde könnte ich an dieser Stelle alle Mitarbeiter der Arbeitsgruppe aufzählen, da alle dafür gesorgt haben, dass so ein hervorragendes Arbeitsklima herrschte.

Des Weiteren bedanke ich mit hiermit beim Deutschen Zentrum für Luft- und Raumfahrt, welches diese Arbeit im Rahmen der Projekte 50QX0702 und 50QM0501 gefördert hat.

Ebenso bedanke ich mich bei meinen Eltern für die jahrelange Unterstützung im Laufe der Studienzeit.

Eidesstattliche Versicherung

Hiermit versichere ich an Eides Statt, dass ich die vorliegende Arbeit abgesehen vom Rat meiner akademischen Lehrer ohne fremde Hilfe und lediglich unter der Verwendung der angegebenen Literatur sowie den bekannten Nachschlagewerken der Naturwissenschaften angefertigt habe, und sie nach Inhalt und Form meine eigene ist. Diese Arbeit ist unter Einhaltung der Regeln guter wissenschaftlicher Praxis entstanden.
Ich versichere, dass diese Arbeit weder ganz noch teilweise an anderer Stelle zur Prüfung vorlag. Frühere Promotionsversuche wurden von mir nicht vorgenommen.
Desweiteren erkläre ich hiermit, dass ein Teil der in Kapitel 5.1 präsentierten Ergebnisse bereits in einer Veröffentlichung unter der Referenz *"Ehresmann, B., S. Burmeister, R. F. Wimmer-Schweingruber, and G. Reitz (2011), Influence of higher atmospheric pressure on the Martian radiation environment: Implications for possible habitability in the Noachian epoch, J. Geophys. Res., 116, A10106, doi:10.1029/2011JA016616"* vorliegt. Die in der Veröffentlichung präsentierten Ergebnisse wurde mit einem Grundgerüst des in Kapitel 4 beschriebenen Modells berechnet. Für diese vorliegende Dissertation wurde das Modell erweitert und die Ergebnisse neu berechnet, so dass neue Erkenntnisse gewonnen werden konnten.

Kiel, den

_____

Bent Ehresmann